EXPERIMENTAL ANALYSIS AND EVALUATION OF A DYNAMIC POSITIONING THRUSTER IN HEAVY LOADING CONDITIONS

SAID EL-LABABIDY

EXPERIMENTAL ANALYSIS AND EVALUATION OF A DYNAMIC POSITIONING THRUSTER IN HEAVY LOADING CONDITIONS

by

©Said El-Lababidy, B. Eng., M. Eng.

A Thesis Submitted to the School of Graduate Studies

in Partial Fulfillment of the Requirements for the Degree of

Doctor of Philosophy in Engineering

Faculty of Engineering & Applied Science

Memorial University of Newfoundland

March 2005

St. John's, Newfoundland, Canada

ABSTRACT

Over the past few years, Dynamic Positioning (DP) systems have seen increasing use in the offshore oil and gas industry. As operations move into more hostile and deeper waters, the need for DP systems has become almost mandatory. Thrusters working at low advance ratios are employed in a wide range of offshore and marine applications on Floating, Production, Storage and Offloading (FPSO) systems, shuttle tankers, tug boats, and mobile offshore units. Therefore, an understanding of the flow around a DP thruster is of great practical interest.

Despite this interest, there is lack of knowledge on the description of the hydrodynamic characteristics of a DP thruster's wake under varied operating conditions and regarding a description of the effects of the current wash produced from DP thrusters when they are in operation. The large number of parameters involved in these particular problems does not allow an experimental and systematic coverage of the various phenomena of the DP thruster's wake. Therefore instead, recourse must be taken to a combination of experiments and calculations, which together eventually will yield a prediction tool that can be used to further improve the analysis of a DP thrusters wake. With the increasing importance and applications of DP thrusters in the offshore oil and gas industry, the designer as well as the operator must have more information about the operational propulsive characteristics. Future development and the success in such approaches depend greatly upon our understanding of the flow around a DP thruster.

Different phenomena associated with the propeller wake can be measured by the introduction of laser techniques: Laser Doppler Velocimetry (LDV) and Particle Imagine

Velocimetry (PIV), as propeller flow velocity-measuring tools. Moreover, with Computational Fluid Dynamics (CFD) codes finding their way into practical applications, a combined analysis is gradually becoming feasible. Experiments are then used to validate and complement computations.

The aim of this study is to provide a comprehensive and systematic analysis of the flow produced from the operation of a DP thruster with and without a nozzle, under varied operating conditions. Furthermore, this study aims to quantify the interaction effects between the DP thruster wake and any structures placed in the working region of the DP thruster up to 15 diameters. This study is the first such approach to the particular problems associated with DP thruster operation.

In this research, a DP thruster's performance characteristics and wake velocities were analyzed experimentally, and the DP thruster near and far wake profile was simulated computationally. The DP thruster performance characteristics were investigated at different propeller speeds, with and without a nozzle, and over a range of advance ratios including the bollard pull condition. The DP thruster wake velocities were measured using two different laser techniques in two different facilities: a LDV system at the National Research Council of Canada (NRC) Institute for Ocean Technology (IOT) cavitation tunnel; and a Stereoscopic PIV system at the Italian Ship Model Basin (INSEAN), Rome, Italy, large circulating tunnel. The numerical simulation of the DP thruster wake profile was performed using CFD software FLUENT 6.0. The experimental results of the DP thruster near wake velocity were used as input to the CFD numerical simulation.

The results of the experimental work of this study show the advantages of using ducted thrusters rather than open thrusters in low speed and DP applications. Also, these results provide valuable data about the safest distance, which should be between the DP thrusters and any submerged structure in the slipstream. The evaluation of the DP thruster near and far wake characteristics under a variety of working conditions provide designers of structures in the slipstream of the DP thruster with reliable and accurate data of the DP thruster wake momentum, thrust and energy propagation. These data are fundamental in calculating the load increases on these structures due to the operation of the DP thruster. Therefore, reliable and sound design of these structures can be achieved.

A number of DP thruster near and far wake simulations under a variety of working conditions were performed using FLUENT 6.0. The simulation of the DP thruster wake was simplified and was considered to be similar to a turbulent jet flow, in which the flow of the propeller was simulated without using the detailed propeller geometry. The results from the CFD simulations showed the capability of this method in simulating the DP thruster wake propagation and dissipation under a variety of working conditions.

The results of this research provide detailed data about DP thrusters' performance characteristics, near and far wake hydrodynamic features, wake momentum propagation and far wake momentum effects under a variety of working conditions. Moreover, the results of this study provide reliable and accurate data about the DP thruster wake to be used for numerical and CFD simulation and validation work. These can be used as an important tool for evaluating the performance of DP thrusters and for predicting DP thrusters wake effect on structures in the slipstream.

ACKNOWLEDGEMENTS

Thanks to God for providing me with the opportunity and ability to accomplish this task. This work would not have come to fruition had it not been for the support and friendship of those with whom I have worked and lived during the past several years.

I am forever grateful to my family their love, support and encouragement throughout the years. Thanks to my wife, Samah, and my daughter, Sara, for their support and patience over such a long period of time.

I would like to express my deepest gratitude and appreciation to my supervisor, Prof. Neil Bose, my co-supervisor, Dr. Pengfei Liu, and member of the supervisory committee, Dr. Dan Walker. They provided much-needed advice and guidance during the course of this research. Their interest and encouragement, as well as many stimulating discussions and helpful suggestions, played a major role in the progress of this work. Without their efforts, this research would not have been possible. I appreciate the way they encouraged me and kept me on the right track.

I wish to extend my gratitude to Prof. Bose for his experience and suggestions, and his guidance in conducting this research and preparing this thesis. Also, to Dr. Pengfei Liu, who availed me of the opportunity to have an office, computer, and access to the computer facilities and conduct the model test program during my Ph.D work.

Thanks are due to the Arab Academy for Science, Technology and Maritime Transport (AASTMT) Alexandria-Egypt; Memorial University of Newfoundland (MUN) Newfoundland, Canada; the Institute for Ocean Technology (IOT) of the National Research Council Canada (NRC), the Italian Ship Model Basin (INSEAN), Rome – Italy;

Petroleum Research Atlantic Canada (PRAC) and the Natural Sciences and Engineering Research Council of Canada (NSERC) for the financial support of this thesis. Thanks also are due to Norsk Hydro Canada for their participation in the travel support to visit INSEAN through a grant to Dr. Thormod Johansen.

Many people have contributed to the experimental program. The experiments described in this thesis were conducted with the help of the technical staff of the Institute for Ocean Technology (IOT), Memorial University of Newfoundland (MUN), and the Italian Ship Model Basin (INSEAN). They gave valuable suggestions for improvement of the test program. Their contributions are acknowledged with appreciation.

The generous contribution and continuous support of the National Research Council's Institute for Ocean Technology and the Italian Ship Model Basin Large cavitation tunnel department in this research are gratefully acknowledged.

INSEAN has provided vital support to this research. I would like to address a special word of thanks and appreciation to Dr. Fabio Di Felice who helped me in arranging all my matters in Rome, and learning more about Stereoscopic Particle Image Velocimetry technique and propeller wake evaluation. Special thanks are due to Guido Calcagno, Mario Felli, Francisco Pereira, Francesco Salvatore and Alessandro Testerini for their devotion to our work, support, help and hospitality.

Special thanks are due to Eric Thronhill for his valuable advices during the numerical work of this study.

Last, but not least, I am eternally grateful to my friends in Egypt and Kuwait, and my friends and Muslim community in St. John's, Canada.

TABLE OF CONTENTS

LIST OF FIGURES

LIST OF TABLES

NOMENCLATURE AND ABBREVIATIONS

Nomenclature

D	.....	propeller diameter, m
H	.....	flow shape factor
J	.....	advance coefficient, $J = V_A/(n.D)$
K	.....	number of propeller blades
K_Q	.....	torque coefficient, $K_Q = Q / (\rho. N^2.D^5)$
K_T	.....	thrust coefficient, $K_T = T / (\rho. N^2.D^4)$
K_{TN}	.....	duct thrust coefficient
K_{TP}	.....	propeller thrust coefficient
K_{TT}	.....	ducted propeller total thrust coefficient, $K_{TT} = K_{TP} + K_{TN}$
K_{TN} / K_{TT}	.....	duct thrust contribution ratio
$m^{0'}$	.....	mass flow deficit, Kg/s
M'_{XX}	.....	momentum flux deficit in the X direction, kN
M'_{OX}	.....	swirl (tangential) flux deficit in the X direction, kN
m^0	.....	normalized mass flow deficit
M_{XX}	.....	normalized momentum flux deficit in the X direction
M_{OX}	.....	normalized swirl (tangential) flux deficit in the X direction
N'	.....	number of SPIV images per plan
N	.....	angular speed of propeller shaft, rev/s
P	.....	propeller pitch, m
P/D	.....	propeller pitch ratio
Q	.....	torque, N.m
R	.....	propeller radius. m
r/R	.....	propeller radius fraction
T	.....	thrust, N
u	.....	flow velocity component in X direction, m/s
v	.....	flow velocity component in Y direction, m/s
V_A	.....	velocity of advance, m/s
V_{ax}	.....	propeller induced axial flow velocity, m/s

V_r	.....	flow radial velocity, m/s
V_d	.....	axial flow velocity at X/D =0.5
V_t	.....	flow tangential velocity
V_X	.....	measured axial flow velocity downstream of the propeller, m/s
V_{ax}/V_a	.....	axial flow velocity ratio
V_{ax}/V_d	.....	axial flow velocity ratio
V_r/V_a	.....	flow radial velocity ratio
V_t/V_a	.....	flow tangential velocity ratio
w	.....	flow velocity component in Z direction, m/s
X	.....	propeller downstream distance, m
X/D	.....	axial downstream position

Greek Symbols

Θ	.....	angular coordinate angle
ρ	.....	fluid density, Kg/m^3
ξ	.....	flow vorticity (s^{-1}), $\xi = \frac{\partial v}{\partial x} - \frac{\partial u}{\partial y}$
Γ	.....	flow circulation, m^2/s
η	.....	propeller open water efficiency, $\eta = (J.K_T) / (2\pi.K_Q)$
δ	.....	radial distance where the axial velocity equal to the free stream velocity
σ	.....	velocity standard deviation

Abbreviations

CFD	.....	Computational Fluid Dynamics
CNC	.....	Computer Numerical Control
DP	.....	Dynamic Positioning
FPSO	.....	Floating Production Storage And Offloading
INSEAN	.....	Italian Ship Model Basin
IOT	.....	Institute for Ocean Technology
LDV	.....	Laser Doppler Velocimetry
MIT	.....	Massachusetts Institute of Technology
NRC	.....	National Research Council of Canada

PIV	.....	Particle Imagine Velocimetry
RMS	.....	Root Mean Square
SPIV	.....	Stereoscopic Particle Imagine Velocimetry

CHAPTER 1

INTRODUCTION

When a freely floating body is placed in the marine environment, different forces and moments act on the body, tending to cause it to translate and rotate. Wind, waves and currents create forces and moments. If a vessel is to remain within a given distance of a reference point on the bottom, or follow a predetermined path, the capability to generate counter forces and moments must be included on the vessel. There are many ways used to provide counter forces, but Dynamic Positioning (DP) systems and mooring lines systems are the only practically effective tools for keeping a vessel on point (Brothers, 1999).

The dynamic positioning system can be defined as a process involving the action of commanded thrusters that are capable to generate counter forces in any direction, because the environmental forces are able to come from any direction. The position is known at all times from the data transmitted by a position reference system. Thrusters represent the actuating element in the DP control system. There are different types of thrusters used in DP systems. The majority are steerable over 360^0 and mounted below the hull, or placed in tunnels crossing the hull from one side to the other.

The concept of DP has been available since the early 1960's (Fay, 1990), but it is constantly being improved and developed to meet the changing needs of the offshore industry. In the offshore industry activities have shifted toward increased water depths, which in some cases prohibit the use of conventional passive mooring systems. The flexibility and mobility of DP systems led to their application for the exploration of marginal oil fields, with the added advantage that assistance of anchor handling vessels is no longer necessary. This advantage is also beneficial for cable or pipe laying activities. Indeed it seems to be a trend for oil companies to require the use of actively controlled ships in the vicinity of sub sea pipe lines to avoid the risk that these may be damaged by the use of anchors.

A combination between a DP system and mooring system is used in some cases to improve the economy and safety of the offshore project (Morgan, 1978). This can be the case for mooring systems where the DP system is used only for reducing the maximum loads by increasing the damping of the system in severe weathers. In such cases the size of the single point mooring system may be reduced.

DP thrusters are also used to improve maneuverability and operation in many applications in shipping industries. They are used in dredging vessels, naval ships, tankers, container ships, tugs boats and ferries. Future development and the success in such approaches depend greatly upon our understanding of the flow phenomena around a DP thruster.

DP, tracking and low speed maneuvering have for a long time defied attempts to properly analyze and predict their performance (Nienhuis, 1992). This is undoubtedly due to the complexity of this dynamic problem where not only the hydrodynamic aspects are

important but also control aspects form an integral part of the system. The traditional way of solving this problem was by splitting the problem into smaller parts. Each part was considered separately and no full coverage of the problem was undertaken. With the development of time domain simulation programs more integral analyses has been undertaken (Nienhuis, 1992).

Despite this interest, there is lack of knowledge in the description of the hydrodynamic characteristics of a DP thruster's wake. This is due to the complexity of the DP thruster wake, which does not allow a complete experimental and systematic coverage of the various phenomena. The flow in the wake of a DP thruster involves several complex features: transition zones, turbulence, presence of vortical structures, deformation, effects of waves and currents, vortex rollup and break down, shear layers, etc. These do not easily allow a complete evaluation of the flow features. Furthermore, the operation of DP thrusters in the bollard pull condition adds additional complexity to the DP thrusters' wake, where the propeller is heavily loaded with very high propeller induced velocities. The blade sections are at a high angle of attack, with large radial flow, large section drag coefficient and very strong tip and hub vortices (Jessup *et al.* 2004). Moreover, the vessel hull boundary and the vessel motion as well as waves and currents will affect the wake from the DP thrusters. The location of the DP thrusters, below the hull or placed in tunnels crossing the hull from one side to the other, affects any structures behind and downstream their region of operation. When DP thrusters are in operation, they create a water jet current behind and downstream of the thruster. Any production pipelines, moorings and other structures downstream are subjected to this current wash or momentum impacts. These impacts create fluid loading on these

structures. Any damage that may occur in these structures will affect the environment, the productivity, and the reliability of the offshore projects. There is a lack of knowledge in describing and evaluating DP thrusters wake induced load. The knowledge of the wake force loading and characteristics of DP thrusters are fundamental in designing of structures placed in the slipstream and is of primary importance for the reliable operation of these members. Therefore, it is important to obtain experimental information on the flow field around these thrusters.

1-1: Objectives

The objectives of this thesis are to provide detailed descriptive data of the DP thruster's wake hydrodynamic characteristics and to quantify the effects of the DP thruster wake force loading on structures placed in the working region up to 15 diameters downstream from the thruster under varied operating conditions. The approach was to perform performance and wake measurements tests on a DP thruster model with and without a nozzle at different low advance coefficient values, including the bollard pull condition. This was to simulate as closely as possible the actual operating conditions of DP thrusters in order to obtain accurate presentation and evaluation of their performance, wake characteristics, and wake induced-load effects. Emphasis was placed on obtaining accurate prediction of the DP thruster duct and strut geometry effects and of the far wake momentum and energy propagation. It is expected that such information will improve the prediction of the DP thrusters far wake momentum impacts on any structures behind and downstream of their operation.

The present work is thought to constitute the first known published attempt to perform an in-depth analysis of DP thruster wake characteristics and induced load effects.

1-2: Previous Research

A historical review of the application and different types of DP systems is provided by Morgan (1978). A DP thruster is a type of unconventional propulsor system, known as ducted propulsor. The idea of a shroud around a propeller is almost as old as the invention of the propeller itself (Geissler, 1918). The ducted propeller came into practical use when Luigi Stipa and later L. Kort experimentally proved the special advantages connected with this type of propulsion device (Sacks *et al.*, 1962). The experiments clearly showed that the presence of the duct led to a considerable increase in thrust performance in static operation and at low forward speed. The gain in performance was particularly large when the propeller was heavily loaded, which makes the ducted propeller suitable for propulsion of tugs and trawlers (Dyne, 1970). The ducted propulsion system was applied in the early 1970's to large ships with heavily loaded propellers such as tankers and bulk carriers (Narita *et al.*, 1981). DP systems have been available since the early 1960's, but they did not attract attention until the exploration and development of offshore oil and gas fields moved into deep waters. Hydrodynamic characteristics of these thrusters are still in the research stage. More studies are required in order to improve the reliability of such systems.

In the 22nd ITTC (1999), the report of the Specialist Committee on Unconventional Propulsors reviewed the problem of the extrapolation of powering performance of vessels fitted with ducted propellers. The three methods presented by

Stierman (1984) were discussed. In the first one the nozzle is considered as an appendage of the hull, in the second one as a part of the propulsion system, and in the third one the interaction between ship, nozzle and propeller is considered. Abdel-Maksoud *et al.* (2002) shows the drawback of each method presented by Stierman (1984). The investigation of the hull fitted with a nozzle alone as considered in Stierman's first and third methods, leads to limited results due to the weak consideration of the interaction between the nozzle and the propeller. The flow around the nozzle is strongly dependent on the thrust coefficient of the propeller and that explains the drawback of the second method of Stierman, where, the thrust of the nozzle and of the propeller are scaled separately.

The study of the wake characteristics of a ducted propeller is by no means new. A summary of such studies is represented by Nienhuis (1992). The majority of the studies were done to evaluate the performance of thrusters under varied operating conditions of inflow angles, advance coefficient and ship speed (Shields 1965, Harvald 1967, Oosterveld *et al.* 1970, Ridely 1971, Dyne 1973, van Leest *et al.* 1976, and Moberg *et al.* 1983).

Oosterveld (1973) undertook a number of experiments using different nozzle' shapes and geometry in order to determine the optimum nozzle shape to be used with ducted propellers from efficiency viewpoint. Moreover, he performed a number of experiments to obtain data for analyzing the maneuvers of vessels fitted with ducted propellers.

One of the most interesting points of research for DP thrusters is the evaluation of the interaction effect between DP thrusters and a ship hull. The arrangements of thrusters

in groups below the keel lead to thruster–thruster and thruster–hull interactions. The thrusters may operate in each other's slipstream with a consequent loss of thrust (Wise *et al.* 1975, English 1975, English *et al.* 1975, Van der Made *et al.* 1976, Lehn 1980, Van den Boom *et al.* 1983, Moberg 1983, Nienhuis 1986, Lehn 1990, Nienhuis 1992, and Webster *et al.* 1999).

Lehn (1980) performed a number of experimental tests to study the interaction of two-azimuthing thrusters in each other's vicinity at different thruster positions and angles in open water at the bollard pull condition. From these tests Lehn established that the forward propeller is not affected by the rear one if the mutual distance exceeds approximately two propeller diameters. Nienhuis (1992) established a method for calculating the interaction effect between two thrusters as a function of distance between the two thrusters and of azimuth angle of the thrusters. This is by calculating the flow induced by one of the two thrusters and assuming that the second one is not present. Once the flow field is determined, the thrust and torque of the second thruster is calculated by taking the average axial inflow speed to the second thruster and using the open water diagram. This method was validated assuming that the operation of the first thruster is not affected by that of the second thruster.

The influence of the hull on the effective inflow speed and direction of the DP thrusters when mounted on the hull were studied by Yumuro (1975), Inoue (1981), Kose (1982), and Nienhuis (1992).

The first detailed thruster slipstream measurements were made with 2D LDV equipment in the MARIN towing tank (1986 – 1987) by Nienhuis. These measurements were done on a thruster mounted under a simple shaped barge in conditions similar to

open water conditions. The results of the flow measurements show that the flow behind the ducted propeller behaves similarly to a turbulent jet issuing from an orifice, where the velocity profile behind the propeller may be divided into two zones: the initial developed zone and the fully developed zone. In the initial developed zone the flow is contracted due to the accelerating effect of the propeller and duct. A core flow with lower axial velocity is surrounded by a progressively thickening turbulent shear layer. In this zone, the velocity profile is influenced by propeller geometry, propeller loading and blade loading distributions. In the fully developed zone the flow starts to expand, roll up and vortex break down occurs.

A Health and Safety Executive (HSE) report (2000) studied the effects of DP thruster slipstream on the hull of an FPSO and its influences on the performance of another adjacent thruster. The research, which was done to study and evaluate the far wake of a DP thruster, was mainly based on panel methods in which the flow was considered to be a potential flow and to have a regular vortex sheet in which the effect of viscosity was ignored. Also, the effects of a DP thruster's far wake on structures in the slipstream were mentioned by Liu *et al.* (2001) in their numerical work to investigate the near and far wake, up to five diameters downstream. The analysis was done using the propeller panel code PROPELLA (PROPELLA user manual 1999-2003). Practically, the application of panel methods does not give a complete description of the slipstream flow due to the important roles played by fluid viscosity in determining the rollup, vortex breakdown and dissipation. CFD methods, which include some of the effects of viscosity through Reynolds's number averaging can play a partial role in describing and evaluating this flow type. Experimental work is required to validate such methods.

1-3: Approaches and Methodologies

DP thrusters are used in highly loaded propeller conditions (bollard pull and near bollard pull). Therefore, experimental tests should be performed at such conditions using adequate experimental facilities and techniques. Normally, the limitations of cavitation tunnels do not enable measurements to be performed at a true bollard pull condition.

This research consists of experimental and theoretical studies described here in two phases. The approach was aimed at improving our understanding and knowledge about a DP thruster's wake characteristics and effects. This will provide offshore designers with accurate data to be taken into consideration in the early design stage of the structures in the slipstream of DP thrusters. The intent is to improve the safety, reliability, productivity and environmental safety of the application of the DP systems.

The first phase aimed at providing information about the performance behavior of the DP thruster under varied operating conditions. This was done by evaluating the performance characteristics of the DP thruster under varied propeller speeds, with and without the nozzle, and at propeller geometric pitch ratio of 1.2. This phase was performed at the IOT towing tank.

The second phase was aimed to evaluate the hydrodynamic features of the DP thruster wake under varied operating conditions. This phase was executed in two parts. The first part was carried out in the IOT cavitation tunnel using a Laser Doppler Velocimetry system. In this part, near wake measurements (up to 1.5 diameters downstream) were performed at near bollard pull operating conditions (J=0.4 and J=0.45), and at three different propeller geometric pitch ratios (1.096, 1.2 and 1.835). The second part was performed at the INSEAN (the Italian Ship Model Basin, Rome,

Italy) large cavitation tunnel using a Stereo Particle Image Velocimetry system. In this part, the far wake measurements (up to 15 diameters downstream) were performed with and without a nozzle, at bollard pull and near bollard pull operating conditions (J=0, J=0.4 and J=0.45), and at propeller geometric pitch ratio of 1.2. The size and characteristics of the INSEAN large cavitation tunnel allowed the investigation to include the bollard pull condition.

1-4: Organization of the Thesis

This thesis consists of a total of six chapters. The first chapter forms the introductory study to the thesis. Chapter 1 discusses the issues addressed in this work. The relevant background, literature review, which focuses on previous studies, approaches and methodologies are briefly described. The specifications and descriptions of experimental facilities and measuring techniques are illustrated in chapter 2. The evaluation and analysis of the DP thruster performance tests results under varied operating conditions are given in chapter 3. Chapter 4 forms the body of this thesis. The experimental and theoretical analysis and evaluation of the DP thruster near and far wakes hydrodynamic characteristics; momentum and energy propagation; and energy decay is given in chapter 4. An introduction to the CFD concept and examples of a DP thruster far wake simulation at different advance coefficient values including bollard pull condition using FLUENT 6.0 is giving in chapter 5. Finally, the conclusions arising out of this study are given in chapter 6. Three Appendices (A, B, and C) are also given. The specifications and figures of the DP thruster model and the experiment work test facilities are given in Appendix A. The results of the LDV measurements of the DP thruster near

wake at thruster geometric pitch ratio of 1.096 and 1.835 are given in Appendix B. Finally, the results of the DP thruster whole wake measurements using SPIV are given in Appendix C.

CHAPTER 2

EXPERIMENTAL FACILITIES AND MEASURING TECHNIQUES

Experimental work was performed on a DP thruster model in two research institutes using different experimental facilities and techniques.

The DP thruster performance tests were carried out in the IOT towing tank. In these tests, both the propeller and the duct thrust were measured at propeller geometric pitch ratio of 1.2 and at different propeller speeds (10 rps, 15 rps, 20 rps and 30 rps).

The DP thruster wake velocities were analyzed experimentally using a 2D Laser Doppler Velocimetry (LDV) system in the IOT cavitation tunnel and a Stereoscopic Particle Image Velocimetry (SPIV) in the INSEAN cavitation tunnel. The IOT wake velocity measurements were performed at three propeller geometric pitch ratios (1.096, 1.2 and 1.835), and at different test advance coefficient values (0.4 and 0.45).

In this chapter, the specifications of the experimental facilities and measuring techniques as well as the set up of the experiments are given.

2-1: DP Thruster Model

The propeller used was a 200 mm diameter model of a ducted controllable pitch propeller. Fig. (2-1) shows the elevation and side view of the propeller model. The principal dimensions and particulars of the propeller, the model and the nozzle are given in Table (2-1) (Doucet, 1996). Moreover, detailed information about the propeller model is given in Appendix (A-1).

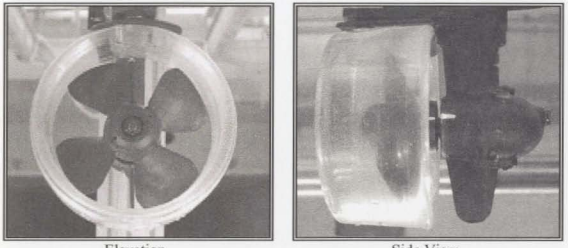

Elevation Side View

Figure 2-1: Elevation and side view of the DP thruster model

Main Particulars	Propeller	Model
Diameter	3.0 m	0.2 m
Number of blades	4	
Hub to propeller diameter ratio	0.367	
Expanded area ratio (EAR)	0.604	
Nozzle Model Particulars		
Length	0.100 m	
Inside diameter	0.202 m	
Nozzle contraction ratio[1]	1.2223	

Table 2-1: Ducted propeller model and model nozzle particulars (Doucet, 1996)

[1] Nozzle contraction ratio is the ratio between the nozzle entrance diameters to the exit diameter. It is (>1) in the case of accelerating nozzle and (< 1) in the case of decelerating nozzle.

2-2: Experimental Facilities

2-2-1: IOT Cavitation Tunnel

The IOT cavitation tunnel is a vertical plane closed re-circulation tunnel. Principal details and description of the tunnel's test section are presented in Table (2-2). The schematic diagram of the IOT cavitation tunnel is shown in Fig. (2-2). More detailed data about the IOT cavitation tunnel are presented in Appendix (B-1).

Test section dimensions	0.5 m × 0.5 m × 2.2 m
Water speed	0 – 12.0 m/s
Test section pressures	0.1 – 1.0 atm.
Drive system	Four-blade axial flow impeller with digital control
Impeller motor power	56 kW, 1500 rpm

Table 2-2: IOT Cavitation tunnel test section particulars

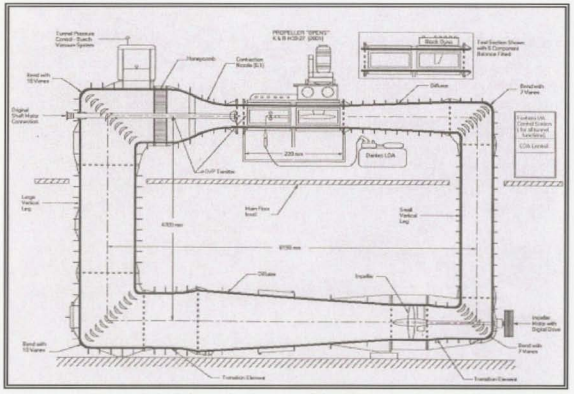

Figure 2-2: Schematic diagram of the IOT cavitation tunnel

2-2-2: IOT Towing Tank

The IOT towing tank is a rectangular tank of 200m in length, 12m in width and 7m in depth. The towing tank carriage driver consists of 8-wheel synchronous motor drive of 746 kW power and of speed range 001 m/s - 10.0 m/s.

The cross sectional view of the IOT towing tank is shown in Fig. (2-3). Models are towed through still water or waves by a carriage spanning the width of the tank. Model rigging is facilitated by two trim docks and a moveable overhead crane (4000 kg).

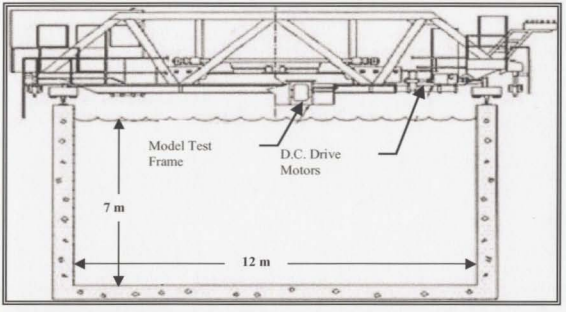

a: IOT towing tank cross-sectional view

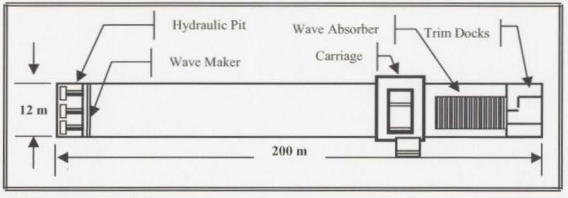

b: IOT towing tank plan view

Figure 2-3: IOT towing tank cross-sectional views

2-2-3: INSEAN Cavitation Tunnel

INSEAN has a free-surface large circulating water channel that can be depressurized. The test section is 10 m long, 3.6 m wide with a depth of 2.25 m. The cross-sectional view of the INSEAN large cavitation tunnel is shown in Fig. (2-4). The maximum water speed is 5.2 m/s. The pressure in the test section can be reduced up to a minimum of 30 mbar (0.03 atm). The schematic diagram of the INSEAN cavitation tunnel is shown in Appendix (B-II).

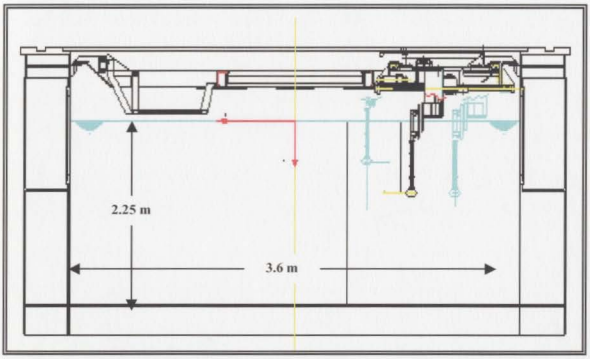

Figure 2-4: INSEAN cavitation tunnel cross-sectional view

2-3: Experimental Measuring Techniques

Wake velocity measurement techniques require adequate performance due to the features of DP thrusters wake, such as marked velocity gradients, strong turbulent fluctuations, three-dimensional boundary layers and hub effects. These do not easily allow a complete evaluation of the flow features.

The techniques for determining flow velocity vectors have traditionally been based on intrusive experimental methodologies. The flow is quantified using sensors, which are placed in, and thus have some effect on, the flow being examined. This approach will inherently introduce some errors into the final results. Even if such errors can be explicitly accounted for, and the results corrected accordingly, there remain practical limitations due to finite size of the sensors. This consideration becomes more critical in situations where the physical size of the model itself is very small. Intrusive techniques can also be difficult to implement in situations where access to the test region is limited by the experimental facility.

Early methods, such as vane wheels and resistance rings, provided only global measurements (van Lammeren *et al.*, 1948). These techniques were simple to implement, but the price for experimental simplicity was limited information on the flow field. Both techniques provided only a single mean axial flow velocity over the diameter of the transducer. Modern electronic transducers and recording technology could be used to improve the experimental efficiency of these procedures. However, regardless of the extent of any such improvements, the simplicity of data collected severely limits their usefulness.

The fact that flow velocities can be measured directly by using light beams and without the introduction of a transducer into the flow has opened up new areas of measurement previously considered impossible. This represents an obvious advantage over intrusive techniques. Nearly all such techniques are optically based, and although termed "non-intrusive" some modification to the fluid is usually required in order for the techniques to function properly. This is usually the addition of light reflective particulate

matter into the flow. The presence of these seed particles is assumed to have a negligible effect on flow properties, while the particles themselves are assumed to faithfully follow the fluid motion. Laser Doppler Velocimetry (LDV) and Particle Image Velocimetry (PIV) are two methods of the non-intrusive measuring techniques. The introduction of the laser has been a key element in the development of both, but the function of the laser is considerably different. Rapid advances in computer and optical techniques have permitted the development of many possible variations of these basic methods.

In this section, the principle of operation of the LDV and PIV techniques, the study LDV and SPIV systems and test specifications and set up are given.

2-3-1: Laser Doppler Velocimetry (LDV)

Laser Doppler Velocimetry (LDV), also called Laser Doppler Anemometry (LDA), is the most commonly encountered non-intrusive technique. It is fast becoming one of the most common tools in flow measurement. The LDV technique allows an efficient data acquisition at a point in time, and hence provides an easy reconstruction of the flow field in a cross section.

The following advantages of LDV indicate the potential capabilities.

- Noninvasive technique, no probes are introduced into the flow, and thus it retains all the flow field characteristics.
- No calibration is required.
- Flow velocity is measured directly and is not strongly dependent on the temperature, density, or composition of the flow medium.

- Ability to measure any desired velocity components directly in any complex flow, without having to measure the other components.
- Measuring any type of velocity (flows, moving or vibrating surfaces, etc.)

The LDV system, as shown in Fig. (2-5), consists of laser light source, transmitting optics to focus the light beams into the measurement region, receiving optics to collect light scattered by the particles in the flow, a photo detector to convert the light into an electrical signal, and a signal processor, which gives the velocity of the flow.

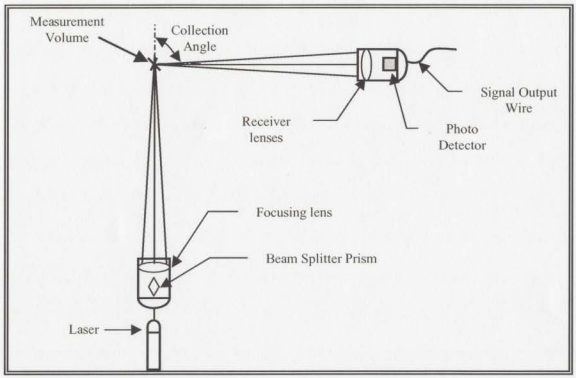

Figure 2-5: LDV system main components

An LDV measures velocity by measuring the Doppler shift in the frequency of laser light from incident and reflected light from microscopic particles within the flow.

A dual beam LDV system consists of two equal intensity beams, which are focused on the same point in the flow field by the focusing lens. The region where the

two beams cross becomes the measurement region, which is called the fringe volume. When a particle goes through the measurement region, light is scattered from each beam. The heterodyning of the scattered light from the two beams provides the shift frequency. The component of velocity measured is always normal to the bisector of the beams and hence is independent of the positioning of the scattered light collection setup. In general, this allows large collection apertures and results in good signal quality (Menon, 1982). To measure two velocity components, two extra beams can be added to the transmitting optics in a plane perpendicular to the first beams. In order to measure the three velocity components two separate probes are required. Also, the 3D flow field in a transversal plane can be easily reconstructed by sweeping the measurement volume of a three component LDV system over a long radius (Chesnakas *et al.*, 1998), or along two orthogonal radial directions using a two components LDV system (Cenedese *et al.* 1985, Jessup 1989, Stella *et al.* 1998A, Stella *et al.* 1998B).

Since the introduction of the LDV technique in 1964 the basic technique has been modified to take advantage of developments both in optical and in electronic processing technology (Durrani *et al.*, 1977). The development of laser Doppler velocimetry allows suitable investigation of complex fluid dynamic fields, like propeller wakes where strong vortex structures, turbulent fluctuations, three-dimensional boundary layers and marked velocity gradients occur (Min 1978, Kobayashi 1982, Hoshino *et al.* 1987).

The first introduction of the LDV to the water tunnel to study the flow characteristics around marine propeller blades was in 1976 in the Marine Hydrodynamics Laboratory of MIT (Kobayashi, 1982). Kobayashi (1982) presented the application of LDV in a propeller wake survey. Hoshino (1993) used a 3D LDV technique to measure

flow around a propeller in a cavitation tunnel to improve his surface panel methods for hydrodynamic analysis of propeller by using a new wake model of the trailing vortices.

Cenedese *et al.* (1985) used the LDV phase sampling technique in evaluating a propeller wake. They concluded that the flow field in the near wake of a marine propeller can be quantitatively analyzed only by means of the LDV which ensures a high spatial resolution and a suitable time resolution without perturbing the field. Felli *et al.* (2001) used a 3D LDV phase sampling technique for the analysis of the flow upstream and behind a four bladed, highly skewed propeller in a large circulation water channel. Stella *et al.* (1998B) used the same LDV technique to analyze the geometrical and hydrodynamic features of a propeller downstream wake in the cavitation tunnel.

The density of particle concentration or seeding is a critical factor for LDV operation and effectively determines the data-sampling rate. In some instances the natural presence of dirt particles will be sufficient, while in other cases artificial seed particles are introduced to the flow. Another factor affecting the operation of the LDV is the size of the particles. Particles that are too small will contribute to background noise levels. However, too large particles will be detected but may not be properly following the flow.

2-3-2: Particle Image Velocimetry (PIV)

PIV is a whole flow field technique providing instantaneous velocity vector measurements over a plane in a flow. It is aa robust optically based measurement technique, which since its introduction has received extensive attention and utilization. It is a quantitative technique that relies on the basic principle of distance over time to yield velocity, typically along a two-dimensional slice within a particular flow.

In this technique, the flow is seeded with small particles and illuminated by a thin sheet of pulsed laser light. Particles moving within the light sheet are recorded photographically by a camera placed at right angles to the light sheet as shown in Fig. (2-6).

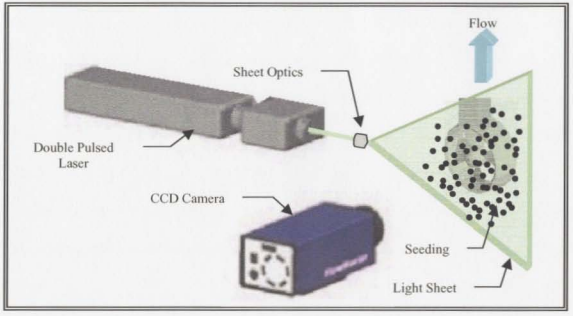

Figure 2-6: PIV system main components

The light sheet is pulsed twice (switched on and off very quickly) at a known interval time. The first pulse of the laser freezes images of the initial positions of seeding particles onto the first frame of the camera. The camera frame is advanced and the second frame of the camera is exposed to the light scattered by the particles from the second pulse of laser light. There are thus two camera images, the first showing the initial positions of the seeding particles and the second their final positions due to movement of the flow field. The two camera frames are then processed to find the velocity vector map of the flow field. This involves dividing the camera frames into small areas called interrogation regions. In each interrogation region, the displacement of groups of

particles between the two camera frames is measured using correlation techniques, and hence the velocity vectors in the flow can be calculated.

The classical PIV technique is just a two-dimensional measuring technique, which is only capable of obtaining two components of flow velocity vectors in the plane of illuminating laser sheet. The out-of-plane component of velocity vector is lost. Recent advances in PIV technique have been directed towards obtaining all three-components of fluid velocity vectors in a plane or in a volume simultaneously to allow the application of PIV technique to more complex flow phenomena. Several three-dimensional PIV methods or techniques have been developed successfully. The Stereoscopic PIV technique is a most straightforward and easily accomplished method for three-component velocity measurement in the illuminating laser sheet plane. It always uses two cameras at different view axes or offset distance to do stereoscopic image recording. By doing the view reconciliation, the corresponding image segments in the two views are matched to get three components of the flow velocity vectors. Development of a Dual-plane Stereoscopic PIV System for simultaneous measurements of all three components of velocity and vorticity vectors in fluid flows could help to improve our understanding of complex flow phenomena. Obviously, it is desirable to obtain all three components of the vorticity field simultaneously in order to gain a complete understanding of the instantaneous vorticity fields. Fig. (2-7) shows the Stereo technique in investigating the real 3D displacement of seeding particle.

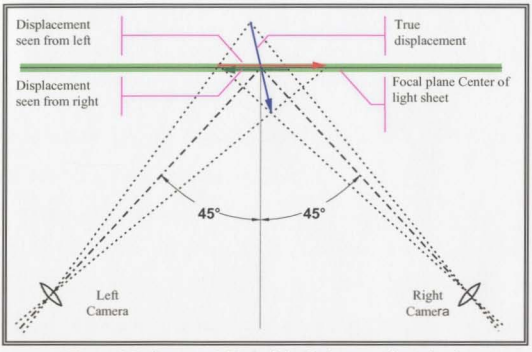

Figure 2-7: Stereo real 3D particle displacement investigation

PIV differs from the LDV technique, in that with PIV the simultaneous velocity at many points in the flow is determined. In contrast, when using LDV velocity measurement at only one point in the flow is determined. Hence the PIV technique has the ability to obtain full velocity field information instantaneously. That is why it is considered to be the obvious choice to capture the flow structures far downstream in a propeller wake. For propulsors operating in highly complex flows this may be the only way to fully capture the structural details of the vortices (Stella *et al.*, 1998B). Felice *et al.* (2000) used PIV to investigate the spatial and temporal evolution of a four bladed marine propeller placed in a uniform flow in a circulating water tunnel. Judge *et al.* (2001) used both a 3D LDV and a 3D PIV system in the David Taylor water tunnel to study the tip leakage vortex occurring on a ducted rotor in order to examine the variability in the vortical flow. Lee *et al.* (2004) used a Stereoscopic PIV technique to

identify the structure of a five bladed propeller wake up to one diameter downstream at three different advance coefficient values of 0.59, 0.72 and 0.88.

2-4: Study Measuring Techniques and Test Descriptions

2-4-1: IOT Laser Doppler Velocimetry Tests

2-4-1-1: System Specifications

The schematic diagram of the LDV experimental test is shown in Fig. (2-8). A 2D DANTEC fiber optics single probe LDV system was used at the IOT cavitation tunnel for the DP thruster near wake velocity measurements. The 2D LDV system consisted of: 60X FiberFlow optics; a particle Dynamic Analyzer processor; PC based data acquisition and analysis software; and a three axis traverse system. A six-watt argon-ion laser is normally operated at approximately 1.5 watts, which results in laser power of 50 to 100 mW out the final lens. The green laser line 514.5 nm in wavelength is usually used for stream wise velocity and the blue line 488 nm wavelengths for vertical or transverse velocity. The optics are configured in backscatter mode and consist of a two color fiber optic probe.

Data was collected and analyzed using the cavitation tunnel computer. DANTEC software was used for data acquisition, initial analysis and the positioning of the probe measurement volume with the three-axis traversing system. DANTEC hardware and software systems are briefly described in the DANTEC operational manual.

The IOT cavitation tunnel has a good accessibility for the LDV because of its square test section with relatively wide viewing windows.

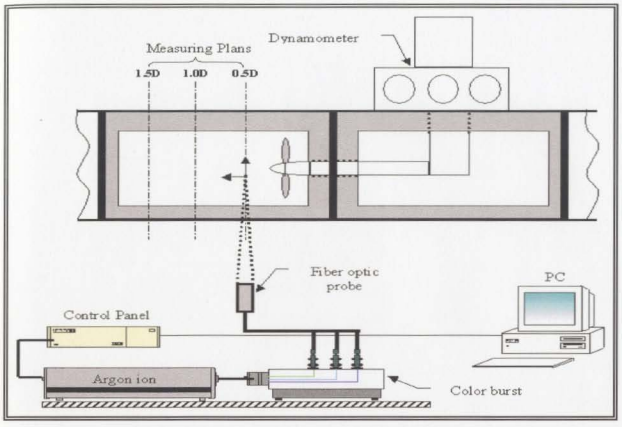

Figure 2-8: Schematic diagram of the LDV experiment

2-4-1-2: System Setup and Measuring Technique

The LDV system was arranged to measure simultaneously the axial and vertical components of the velocity in the test section fixed frame. A special arm was used to enable the *2D* LDV system to measure the third flow velocity component. This arm was used to change the location of the measuring volume by radial movements of the probe. When the probe was located on the vertical radius, along the *z*-axis as shown in Fig. (2-9), position (A), the axial component of the velocity (u) and the lateral velocity (v) were measured. When the probe was located on the horizontal radius, along the y-axis as shown in Fig. (2-9), position (B), the axial and vertical components of the velocity (u, w) were measured.

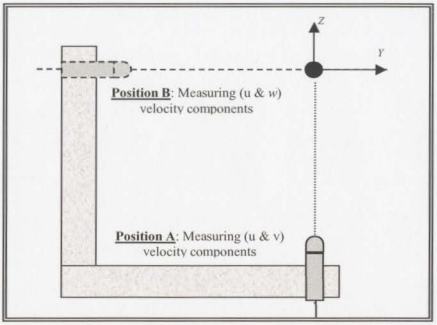

Figure 2-9: The arrangement of the LDV probe positions

The LDV measurement map was limited within the near wake propeller region due to the limitation of the IOT cavitation tunnel window length, which restricted the measurements to 1.5*D* downstream of the thruster. Measurements were done at three downstream transverse planes; the first one was set at 0.5*D* from the propeller blades' centerline, the others at 1.0*D* and 1.5*D*.

Each transverse plane was divided into seven radial locations (circles) with diameter equal to 0.2*D*, 0.4*D*, 0.6*D*, 0.8*D*, 1.0*D*, 1.1*D* and 1.15*D* respectively as shown in Fig. (2-10). The location of the last radial plane was limited by the width of the IOT cavitation tunnel test window (240 mm).

In each plane, there were 220 circumferential points, varying in number from 18 points at the first circle to 45 points at the largest diameter. At each point, the three components of the velocity were recorded as average values over time.

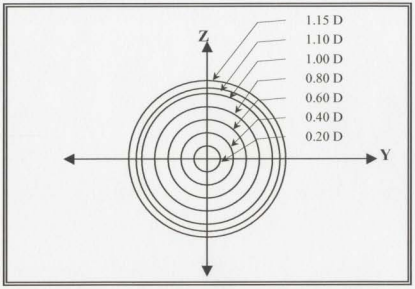

Figure 2-10: Radial measurements planes

The LDV measurements were performed at a constant propeller angular speed of 30 rps and at near bollard conditions. A true bollard condition could not be obtained due to water tunnel circulation.

2-4-2: INSEAN Stereoscopic Particle Image Velocimetry Tests

2-4-2-1: System Specifications

The schematic diagram of the SPIV experimental test is shown in Fig. (2-11). Measurements at the INSEAN cavitation tunnel were performed using an underwater SPIV probe. Fig. (2-12) shows the probe and the thruster installed in the test section. When completely assembled, the probe forms a streamlined torpedo-like tube with an external diameter of 150 mm. The tube was rigidly linked to a bench through two hydrodynamically optimized struts. The whole system could be traversed by a mechanism controlled by a PC to sweep the measurement plane up to $X/D = 15$. The

stereoscopic system consisted of two 2048 X 2048 pixels CCD cameras, with 12-bit resolution. The aperture, the focus and the Scheimpflug angle of the camera lenses were remotely controlled (TSI/SPIV manual, 2000). The laser light was delivered to the underwater sheet optics through the struts and inside an articulated arm. Mirrors within the arm allowed the beam to be correctly aligned with the output optics. The laser optics consisted of a set of cylindrical and spherical lenses, which respectively expanded the beam into a sheet and focused it onto the measurement plane. The laser subsystem consisted of a doubled pulse 15 Hz 200 mJ Nd-YAG laser rigidly attached to the probe support bench. The camera mirror sections were open to the water to avoid multimedia refractions and to minimize the optical aberrations through one single orthogonal water-air interface.

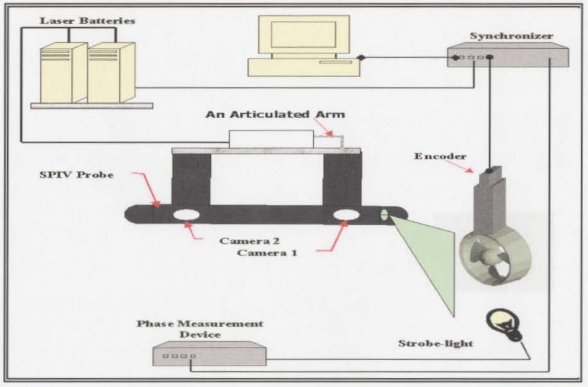

Figure 2-11: Schematic diagram of the SPIV experiment

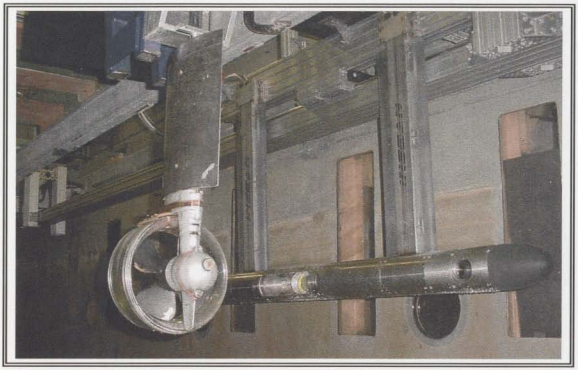

Figure 2-12: DP thruster model and the SPIV probe in the INSEAN large cavitation tunnel

The calibration process of the Stereo PIV system was done in two stages in order to achieve the best overlap imaged area of the two cameras. The first calibration stage was performed outside the test section and the second stage inside the test section using a 2D calibration plate as shown in Fig. (2-13). The overlapped imaged areas of the two cameras created a 3D velocity field area of about 328 mm X 265 mm. The measurement errors for the adopted optical configuration have been previously assessed on a test bench and are about 3% for the light sheet in plane components and about 2% for the out of plane components (Felli, 2003).

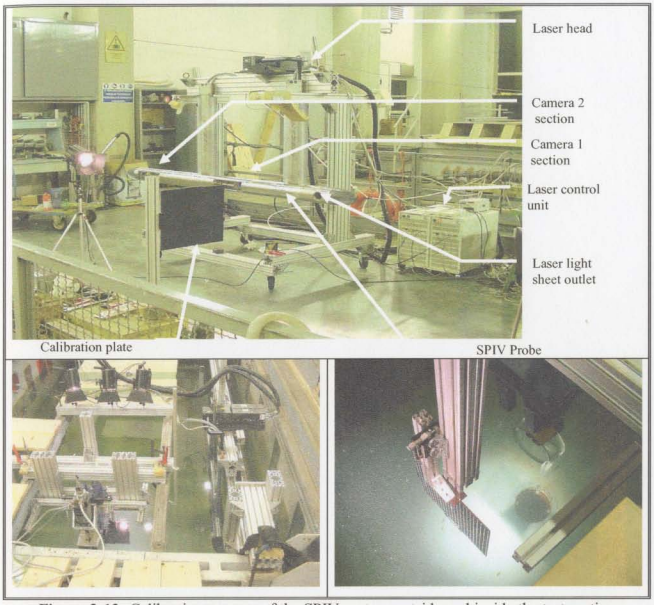

Figure 2-13: Calibration process of the SPIV system outside and inside the test section

2-4-2-2: System Setup and Measuring Technique

A cross-sectional view of the SPIV experiment setup is shown in Fig. (2-14). The PIV measurement map covered the measurements of the near wake and the far wake of the DP thruster at different test conditions. Measurements were done at a propeller pitch ratio of 1.2, with and without the nozzle at three different advance coefficient values (J=

0, J=0.4 and J=0.45). The measurements at the advance coefficient of 0.45 were limited to the near wake region (up to 1.5 diameters downstream of the propeller), while the measurements at J=0 and J=0.4 were performed up to 15 diameters downstream of the propeller. Table (2-3) shows the angular speed of the propeller and the tunnel water speed at each advance coefficient value.

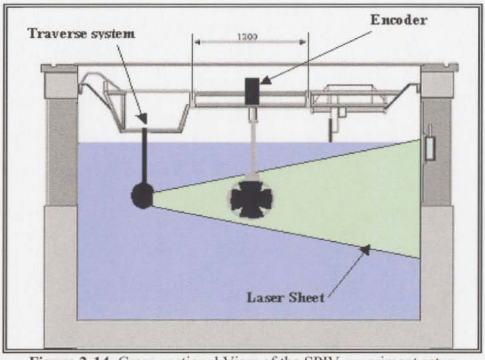

Figure 2-14: Cross-sectional View of the SPIV experiment setup

Advance coefficient (J)	Propeller speed (rps)	Tunnel water speed (V_A: m/s)
0	20	0
0.4	15	1.2
0.45	15	1.35

Table 2-3: Operating parameters of the SPIV experimental work.

Measurements were divided into two regions: near wake region and far wake region. The near wake measurements were obtained up to 1.5 diameters downstream of

the propeller at eight different downstream axial planes. The first measuring axial plane was set at $X/D = 0.1$ from the propeller blades' centerline, the others at $X/D = 0.2$, 0.3, 0.4, 0.5, 0.75, 1.0 and 1.5. The near wake measurements of the ducted propeller at $X/D = 0.1$ and 0.2 could not be obtained due to the presence of the nozzle. Far wake measurements were obtained at six downstream axial planes. The first one was set at $X/D = 3.0$ from the propeller blades' centerline and the others at $X/D = 5.0$, 7.5, 10.0, 12.5 and 15.0.

2-4-3: Coordinate System

A Cartesian (x, y, z) and a cylindrical coordinate system (O-x, r, θ) were used. As shown in Fig. (2-15), the x-axis is along the propeller shaft centerline and points downstream, the y-axis is horizontal, the z-axis is vertical pointing upwards; r is in the radial direction from the x-axis and the angular coordinate θ is measured from the vertical z-axis in the propeller rotation direction that is clockwise when viewed from aft.

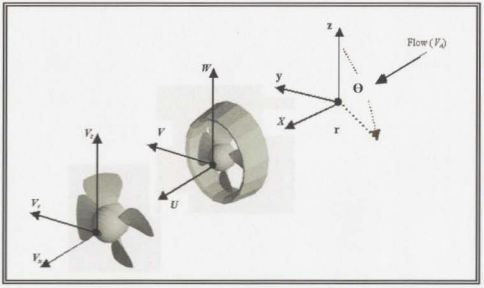

Figure 2-15: Experiment coordinate system

The mesh of the propeller and the nozzle were generated using PROPELLA (Liu 2002)

The analysis of wake velocity was done first by converting the Cartesian velocity components (V_X, V_Y and V_Z) into cylindrical velocity components [axial (V_{ax}), radial (V_r) and tangential (V_t) velocity] where:

$$V_{ax} = V_x - V_A \quad \text{.....Eq. (2-1)}$$

$$V_r = V_Y . \sin(\Theta) + V_Z . \cos(\Theta) \quad \text{.....Eq. (2-2)}$$

$$V_t = V_Y . \cos(\Theta) - V_Z . \sin(\Theta) \quad \text{.....Eq. (2-3)}$$

where:

- V_A is the tunnel flow velocity (velocity of advance).
- V_X is the measured axial velocity downstream of the propeller. It can be defined as the total axial velocity, which includes the propeller-induced velocity in addition to the tunnel flow.
- V_{ax} is the propeller induced axial velocity.

The SPIV wake velocity was initially analyzed by constructing the instantaneous 3D velocity vector field for each image (129 images/plane) from the combination of the 2D encoded velocity vector fields of the left and right camera. Then the mean 3D velocity field was constructed for each plane by averaging the summation of the instantaneous 3D vector files for each plane over 129. The SPIV sampling time was varied from 0.1- 0.6 sec per image. On the other hand, the time averaged LDV velocity components were recorded by averaging the individual LDV measurements over a period of 5 seconds.

2-4-4: Measurement Accuracy and Uncertainty

2-4-4-1: Accuracy of the LDV Measurements

The acquisition time of the LDV records must be long enough to provide a sufficient number of samples to make possible statistical data post-processing (Espositio *et al.* 1998). In this work, the acquisition time was set to be constant (around 5 sec) at all the measurement points. The results indicate fluctuation in the number of validated velocity samples from point to point ranging between 9000 samples and 600 samples. This fluctuation in sampling rate was shown to be a function of the distribution of the particles in the water. This uncertainty was due to low particle concentration and variation of fluid velocity across the measured volume. These two main factors caused poor signal/noise ratio, reduced the accuracy of velocity flow measurements in the blade and blade tip wakes regions, and caused a high fluctuation in the measured velocity flow components. Also, the results indicated uncertainties in LDV measurements when the laser passed near to the edge of the cavitation test window ($r/R = 1.15$).

2-4-4-2: Accuracy of the SPIV Measurements

The technique used for the stereo reconstruction was the method described by Solof (1997) and a detailed analysis of the errors was presented by Prasad (2000).

The uncertainty of velocity measurements from each single camera is mainly due to the error in the particle displacement evaluation, which can be normally considered to be around 1/10 to 1/20 of a pixel for the image analysis and subpixel interpolation algorithms (Raffel *et al.* 1998). This was equivalent to approximately 3 cm/s in terms of velocity for the flow speeds considered here. This error is present in the measurement of

the instantaneous flow field seen by each camera, but with the stereo reconstruction the error increases and is up to 10 cm/s for the longitudinal velocity component.

This relatively large error is a typical value for a SPIV measurement and depends on many factors such as the optical configuration (angle between the cameras), optical aberrations, number of dots in the calibration target, number of planes used in the calibration, etc. The errors due to light reflections from the hub and from the blade edges and the nozzle were also important in flow field regions mapped in proximity to reflection spots.

The moving propeller in the background of the measurement plane is another source of error. To reduce these errors the images where preprocessed in order to remove the background. However the effect of the moving background and of reflections could not be completely eliminated. In fact the correlation peak is still locked at the propeller or nozzle velocity in the regions where there is a lack of particle traces or where the reflections are dominating the PIV images. This effect appears in the PIV images as vectors of very high velocity values, which are called spurious vectors. These vectors affect the quality of the SPIV images. This is clearly represented in Fig. (2-16).

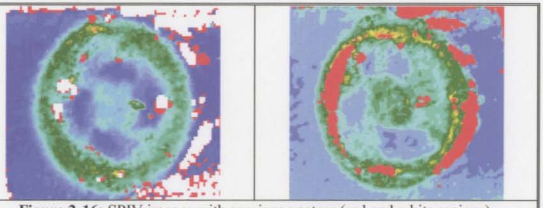

Figure 2-16: SPIV images with spurious vectors (red and white regions)

In the post-processing phase, the validation procedure is very effective to detect such spurious vectors due to the large difference between the flow and the blade velocity. Detected erroneous vectors are eliminated and replaced by interpolation. Nevertheless, spurious vectors might also be validated biasing the statistics especially in the proximity of the hub where the flow and propeller velocity become closer. This effect is relevant especially for the evaluation of second order statistics.

The accuracy of the mean velocity field depends upon the number of acquired samples and upon the shape of the velocity probability distribution function. By using the Student t-distribution (for which the confidence interval for 97.5%, is $\pm 1.96 * RMS / \sqrt{(N'-1)}$, with $N' = 129$), it is possible to estimate the uncertainty in a velocity component to be about 1/6 of the measured RMS velocity.

The comparison between LDV and SPIV accuracies and measurement uncertainties shows that LDV measurements are more accurate than the SPIV results. This is due to the following:

- The nature of the SPIV technique, which is an instantaneous measuring technique, leads to gathering all spatial information of the flow at a certain time. Therefore, there is a finite statistical probability that there are some regions where there is no meaningful input.
- The light intensity of the LDV measurements is higher than for the SPIV measurements. This is due to the difference between the ways of capturing the scattered light from the seeding materials. LDV measurements are usually backward (toward the light source) or possibly forward (away from the light source) scattered light from the seeding particles. Whereas, PIV measurements are sideways scattered

light from the seeding particles. Fig. (2-17) shows the different types of capturing the scattered light from seeding particles. The scattered light has higher intensity in the forward direction, somewhat less in the backward direction and very little in sideways directions (DANTEC/LDV manual 2000). The IOT LDV system is of the backward scattered type, while, the INSEAN SPIV system is a sideways type. Therefore, the accuracy of the LDV measurements is higher for the same laser light power.

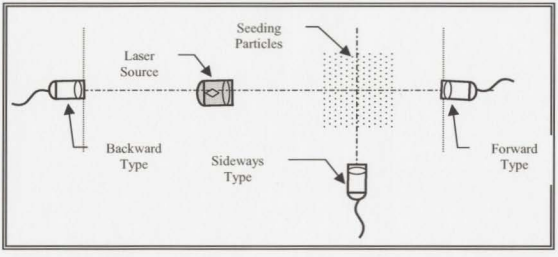

Figure 2-17: Methods of capturing the scattered light from seeding particles

In order to improve the accuracy of the SPIV measurements, the number of samples (N': images per plane) has to be increased. For example, to obtain a measurement error in the velocity of about 1/7 of the measured RMS velocity for the same confidence interval (97.5%), the number of samples would be 189 images per plane. This small improvement in the accuracy requires an increase in data storage and time processing of the measurements to around double the case for a measurement uncertainty of 1/6 of the measured RMS velocity.

CHAPTER 3

DYNAMIC POSITIONING THRUSTER PERFORMANCE CHARACTERISTICS

In an effort to provide experimental data on the performance of Dynamic Positioning (DP) thrusters under variable operating conditions, a series of experiments were done on the DP thruster model, at the Institute for Ocean Technology (IOT) towing tank. These experiments were carried out over a range of advance coefficients.

Through the IOT towing tank tests the performance characteristics of the DP thruster model were investigated with and without the nozzle, at a propeller pitch ratio of 1.2, and at different propeller speeds (10, 15, 20 and 30 rps). The evaluation of the DP thruster performance characteristics tests at the IOT towing tank were performed in order to investigate the performance behavior of the DP thruster at bollard pull and higher loading conditions. Therefore, tests were carried out at bollard pull and higher advance coefficient values. Also, these tests were performed to investigate the contribution of the

duct thrust to the whole performance of the ducted DP thruster under a variety of loading conditions. Therefore, performance tests were performed with and without a nozzle. The thrust of the nozzle was measured using the IOT nozzle thrust measuring arm shown in Fig. (3-1).

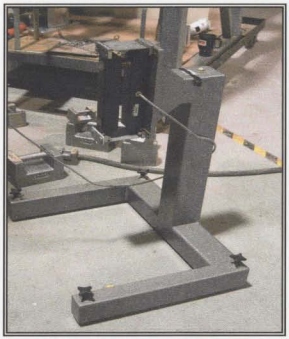

Duct load measuring arm

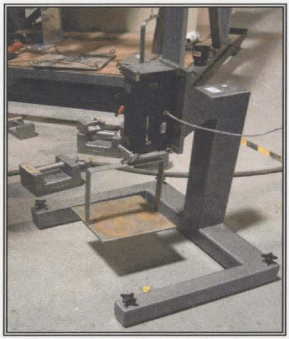

Calibration of the arm

Figure 3-1: The IOT duct load measuring arm

Performance tests with and without a nozzle were performed using the same DP thruster model and at the same thruster geometric pitch ratio. Therefore, the results of these tests do not represent a comparison between open thruster and its equivalent ducted thruster[2] but they represent two different operating conditions of the same thruster in order to figure out the effect of the duct in the operation of the DP thruster.

[2]The equivalent ducted propeller to an open propeller is a ducted propeller generating the same thrust or absorbing the same power of the open propeller at a given propeller speed. Therefore, the equivalent ducted propeller has a smaller diameter and works at higher propeller geometric pitch ratio than the open propeller.

The dynamometer used for these tests was a sealed strain gauged dynamometer mounted between the propeller and the first shaft bearing. The range of thrust measurement was (± 900 N) and the range of torque measurement was (± 45 Nm).

In this chapter, the results of the DP thruster performance tests at the IOT towing tank are given.

3-1: Performance Characteristics

Fig. (3-2) shows the results of the IOT towing tank performance tests of the DP thruster model with and without a nozzle, at different propeller speeds, and at propeller pitch ratio of 1.2. The performance curves of the ducted propeller shown in Fig. (3-2) are represented by the total thrust and efficiency of the system. The total thrust (K_{TT}) is summation of the propeller thrust and the nozzle thrust.

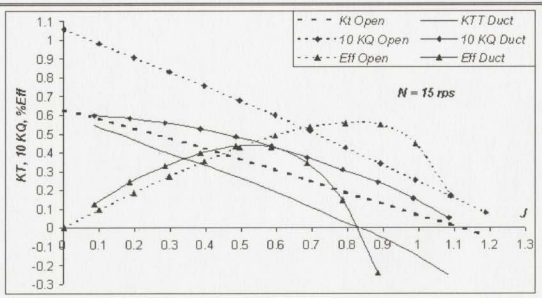

a: Performance curves with and without a nozzle at N=15 rps and P/D = 1.2

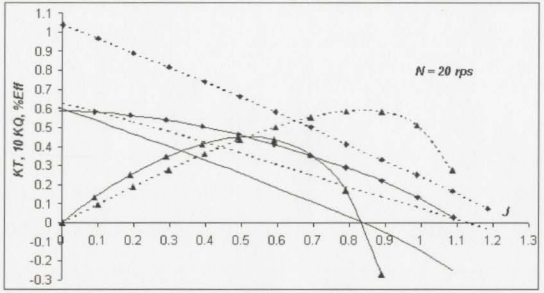

b: Performance curves with and without a nozzle at N=20 rps and P/D = 1.2

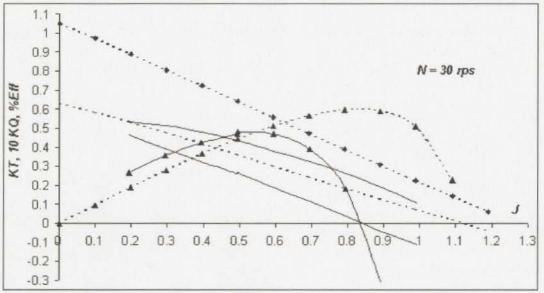

c: Performance curves with and without a nozzle at N=30 and P/D = 1.2

Figure 3-2: Towing tank DP thruster performance curves with and without a nozzle at thruster rotational speeds of 15, 20 and 30 rps and at P/D =1.2

Fig, (3-2) shows that the thrust generated from the propeller without the nozzle is higher than that generated with the nozzle working at the same advance coefficient and propeller speed. This result implies that the loading of the propeller blades in the case of the open propeller is higher than that in the ducted case.

Fig. (3-3) and Fig. (3-4) show the distribution of the thrust coefficient and torque coefficient of the DP thruster with and without a nozzle at different propeller speeds. The distribution of the ducted DP thruster thrust coefficient at different test speeds shown in Fig. (3-3) is representing the total thrust of the system (K_{TT}). The results of these tests indicate that the effect of propeller speed on the torque coefficient is much higher than on the thrust coefficient.

Performance tests at different propeller speeds show a small increase in thrust coefficient and decrease in torque coefficient as propeller speed increases. This can be explained by the difference in Reynolds number at different shaft speeds. The friction coefficient is a function of Reynolds number and as Reynolds number increases, the drag coefficient drops. This causes a reduction in the drag force and an increase in lift, and therefore an increase in thrust. This result implies that the friction forces have more influence on the torque than on the thrust.

Moreover, Fig. (3-3) shows that the influence of the Reynolds number on the torque of a ducted propeller is higher than on an open propeller. This result is also presented by Abdel Maksoud *et al.* (2002).

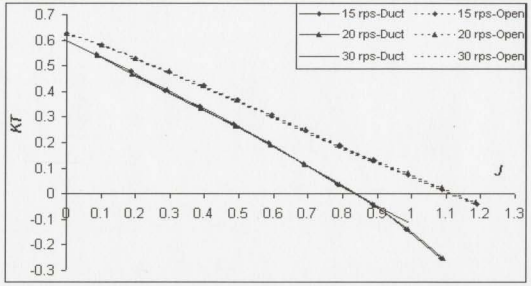

Figure 3-3: DP thruster thrust coefficient distribution with and without a nozzle, at thruster rotational speeds of 15, 20 and 30 rps and at P/D =1.2

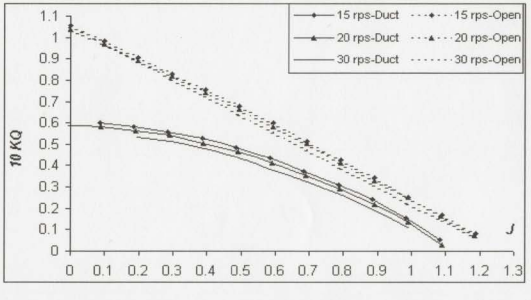

Figure 3-4: DP thruster torque coefficient distribution with and without a nozzle, at thruster rotational speeds of 15, 20 and 30 rps and at P/D =1.2

3-2: Duct Effect

The contribution of the duct to the performance of the DP thruster can be investigated from the distribution of the thrust coefficient of the propeller alone (K_{TP}), duct (K_{TN}) and of the total thrust of a ducted DP thruster ($K_{TT} = K_{TP} + K_{TN}$) as shown in Fig. (3-5). Fig. (3-6) shows the contribution of the duct thrust to the total thrust produced from the ducted DP thruster. These figures show that the duct contributes some 50% of the ducted propeller total thrust at the bollard pull condition. This relative contribution of the duct, however, reduces as advance coefficient is increased. Also, it can be shown that the duct thrust has a negative contribution to the total thrust of the ducted thruster beyond the advance coefficient value of 0.6.

DP thrusters work in very high loading conditions (bollard pull and near bollard pull). Fig. (3-2) shows that the loading on the DP thruster blades is higher in the case of the open thruster than the ducted thruster due to the effect of the duct in reducing the load acting in the thruster blades. Moreover, Fig. (3-5) and Fig. (3-6) show that the duct has a positive thrust contribution to the total thrust of the ducted thruster at bollard pull and near bollard pull operating conditions. These results imply advantages of using ducted thrusters instead of open thrusters in low speed offshore and marine applications. Also, these results show why the majority of DP thrusters are ducted thrusters.

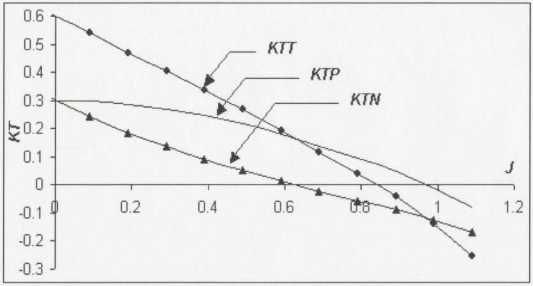

Figure 3-5: Thrust coefficient distribution for the thruster alone (K_{TP}); the duct alone (K_{TN}), and the thruster and the duct (K_{TT})of the ducted DP thruster at $N = 20$ rps

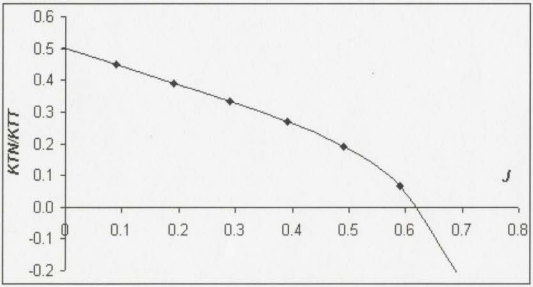

Figure 3-6: Contribution of the duct thrust to the total thrust of the ducted DP thruster at $N = 20$ rps

CHAPTER 4

DYNAMIC POSITIONING THRUSTER WAKE HYDRODYNAMIC CHARACTERISTICS

The flow field around a propeller has been of interest to many researchers who are engaged in the hydrodynamics of both marine and aeronautical propellers (Nienhuis-1992). Since non-intrusive techniques (LDV & PIV) were introduced to measure the velocity in the flow field, many surveys of propeller's flow velocities were carried out (Min 1978, Kobayashi 1982, Hoshino *et al.* 1987, Jessup 1989, Cenedese *et al.* 1985, Nienhis 1992, Chesnakas *et al.* 1998, Stella *et al.* 1998B, Felice *et al.* 2000, Judge *et al.* 2001, Jessup *et al.* 2004, and Lee *et al.* 2004).

The purpose of some of these experiments is to verify accuracy and to refine numerical models for calculating propeller hydrodynamics. Other experiments are aimed at achieving a better understanding of propeller/hull interaction. Most of the measurements were performed immediately behind or in front of the propeller. Limited studies were performed on the far wake region of propellers, and the distance to the propeller in previous experiments never exceeded approximately three diameters.

Moreover, DP thrusters are used in heavily loaded propeller conditions. Experiments should be carried out at bollard pull and low advance coefficient operating conditions. The size limitations of the experimental facilities (cavitation tunnels) do not enable measurements at a true bollard pull condition (J=0). Measurements at near bollard pull condition do not provide a true representation of the bollard pull condition.

The tests described here were done to obtain experimental information on the flow field in the wake of these thrusters. The main objective was to analyze the DP thruster at the near and far wake experimentally when operating with and without a nozzle at bollard pull and near bollard pull operating conditions. The size and characteristics of the INSEAN large cavitation tunnel enabled the investigation of bollard pull measurements.

In this chapter, the hydrodynamic characteristics and momentum propagation of the flow in the near and far wake region will be represented. Also, the effect of the nozzle on the hydrodynamic operation of the DP thrusters will be highlighted. Finally, the effect of the change in the operating conditions of the DP thruster will be presented by evaluating the wake features under varied advance coefficient values.

In order to make a comparison between the LDV and SPIV measurements, the DP thruster near wake region is considered to be up to 1.5 diameters downstream of the propeller. The region beyond 1.5 diameters up to 15 diameters downstream of the propeller is considered to be the far wake region where only SPIV measurements were performed.

All the SPIV results presented in the following were obtained by phase averaging the measurements for a blade position having the trailing edge at the 12 o'clock position.

4-1: Velocity Field Characteristics Around the DP Thruster

In this section, the general flow features of the DP thruster, when operating with and without a nozzle, will be presented for the propeller pitch ratio of 1.2 at different test advance coefficient values ($J = 0$, $J = 0.4$ and $J = 0.45$).

In order to make a comparison between the results of the LDV and SPIV measurements, each SPIV transverse plane was divided into eight radial locations (circles) with diameters equal to 0.2D, 0.4D, 0.6D, 0.8D, 0.9D, 1.0D, 1.1D and 1.2D, respectively using TECPLOT 8.0. TECPLOT software has a capability to extract velocity components at any selected point in flow. Therefore, each radial location (360^0) was divided into 16 equally spaced circumferential points. At each point, the three components of the velocity were extracted manually. In order to reduce the error due to the uncertainty in the determination of the location of the extracting points at each radial location for each transverse plane, the three components of the velocity were recorded as average values for each radial location.

4-1-1: The Distribution of the Wake Velocity Components Around the DP Thruster

Fig. (4-1) and Fig. (4-2) show the LDV and SPIV distribution of the propeller wake velocity components at 0.5 diameters downstream axial position, respectively. Results are plotted for the DP thruster with and without the nozzle at different advance coefficients.

The results of the SPIV and LDV indicate some common features between the distributions of the flow velocity components with and without the nozzle. The distribution of the axial velocity shows low values near the hub increasing radially

outwards to reach a maximum value at a radial position around r/R = 0.6-0.8 for the measurements with the nozzle, and around r/R = 0.6 for the measurements without the nozzle.

The distribution of the tangential velocity indicates high values near the hub due to the presence of the hub vortex. The hub vortex influence decreases at higher radii. At the edge of the slipstream, the tangential velocity is close to zero, as would be expected. The radial velocity generally has a small value. It has negative values, or an inward direction towards the hub, resulting from the contraction of the slipstream and hub effect.

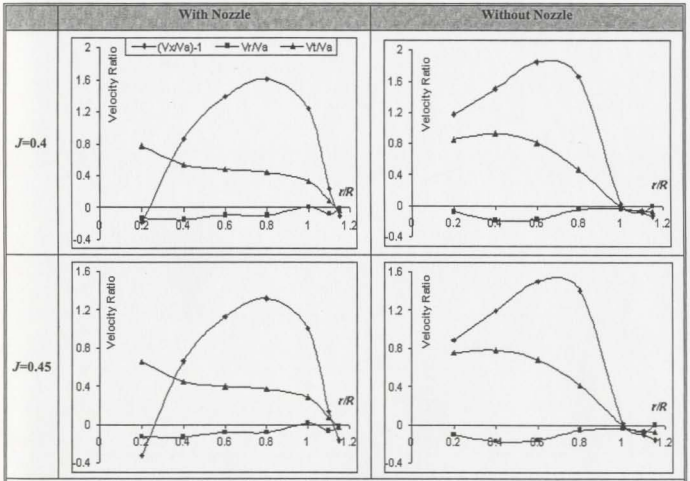

Figure 4-1: Circumferential variation of velocity components around the DP thruster; at J=0.4 and J=0.45; and at X/D = 0.5 using LDV

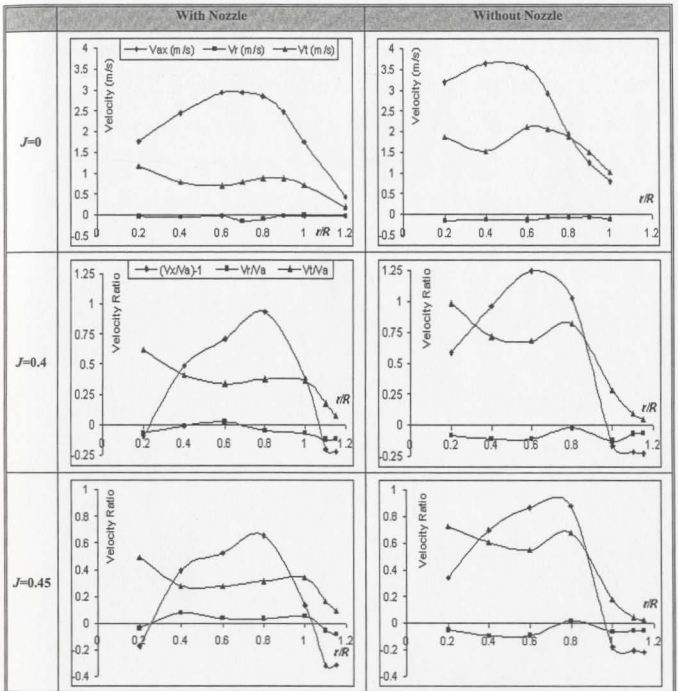

Figure 4-2: Circumferential variation of velocity components around the DP thruster at J=0, J=0.4 and J=0.45; and at X/D = 0.5 using SPIV

Fig. (4-3) shows a comparison between the LDV and SPIV axial flow velocity measurements around the open and ducted DP thruster at X/D = 0.5 and at advance

coefficients of 0.4 and 0.45. By comparing the results of the LDV and the SPIV results shown in Fig. (4-1), Fig. (4-2) and Fig. (4-3), the LDV measurements indicate higher velocity components than the SPIV measurements. Discrepancies between the LDV and SPIV results may be due to tunnel effects. Moreover, Fig. (4-3) shows that the SPIV and LDV measurements show negative axial flow velocity in the thruster blade tip region. This implies the circulatory behavior of the flow in this region, which is known as vortex ring flow. The SPIV measurements indicate higher vortex ring flow than the LDV measurements.

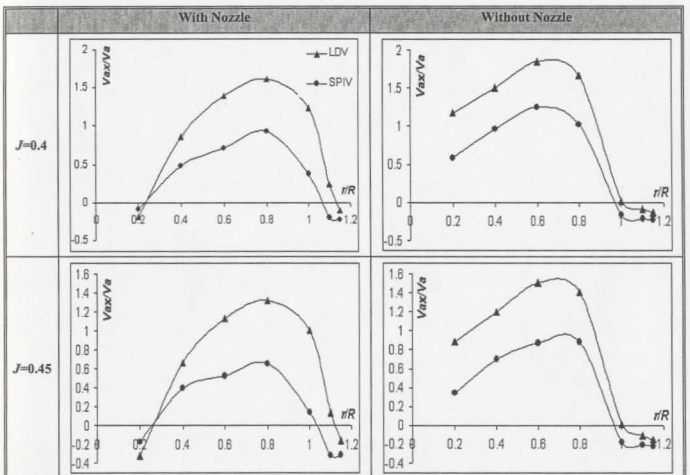

Figure 4-3: Comparison between the LDV and SPIV circumferential variation of the axial velocity component around the DP thruster; at J=0.4 and J=0.45; and at X/D = 0.5

4-1-2: Duct Effect in the DP Thruster Wake Velocity Distribution

The effect of the nozzle can be investigated by comparing the results of the DP thruster wake velocity measurements with and without the nozzle shown in Fig. (4-1) and Fig. (4-2). Measurements without the nozzle indicate higher axial and cross-flow velocity components than measurements with the nozzle.

The results of the measurements without the nozzle indicate a sharp reduction in the axial velocity after the maximum value to reach the zero value, i.e. velocity of the cavitation tunnel, at r/R =1.0. Then the axial velocity has a negative value beyond this range. The negative value of the axial velocity in this region indicates that the flow has an opposite direction to the main flow of the propeller. This is mainly a result of the shear layers produced around the propeller slipstream due to the vortex ring flow. However, measurements with the nozzle indicate gradual reduction in the axial velocity after the maximum value, and it has a negative value beyond r/R = 1.15. This result indicates that the duct increased axial flow over larger diameter and therefore the shear layers around the propeller slipstream are reduced by the presence of the nozzle. These results imply that the propeller with the nozzle is more lightly loaded than the propeller without the nozzle. The accelerating effect of the nozzle reduces the thrust loading of the propeller itself at a fixed advance coefficient; the inflow velocity to the propeller increases, causing an effective increase in advance velocity at the propeller, and consequently a decrease in the propeller blade's local angle of attack.

As propeller load reduces the rotational losses from the propeller blades also reduce. This causes a reduction in the downstream axial and tangential velocities. That is

why measurements without the nozzle indicate higher axial and cross-flow velocity components than measurements with the nozzle.

4-1-3: Advance Coefficient Effect in the DP Thruster Wake Velocity Distribution

The advance coefficient is a measure of the propeller blade loading. As mentioned before, the increase in the advance coefficient value reduces the propeller blade's angle of attack, thereby reducing the loads acting on the propeller.

The results of the LDV and SPIV measurements indicate a reduction in the velocity components' value as the propeller load is reduced, i.e. increasing advance coefficient value, due to the reduction in the angle of attack.

4-1-4: Total Flow Turbulence Distribution Around the DP Thruster

When removing the nozzle, a contraction of the slipstream is observed. This is due to the fact that only the inner part of the propeller blade is able to generate lift while the outer blade regions are stalled. This is expected because the thruster is operating far from its maximum efficiency, as shown in Fig. (3-2). This is demonstrated by the distribution of the total flow turbulence of the DP thruster with and without the nozzle at $X/D = 0.5$ as shown in Fig. (4-4). The total flow turbulence, as presented by Eq. (4-1), has been defined as the non-dimensional standard deviation of the velocity distribution at a given point by the propeller angular velocity.

$$\text{Total Flow Turbulence} = \frac{\sqrt{(\sigma_u)^2 + (\sigma_v)^2 + (\sigma_w)^2}}{W.D} \quad \text{---------- Eq. [4-1]}$$

Where, σ_u, σ_v and σ_w are the standard deviation of the axial velocity and the cross velocities v and w respectively, and W is the thruster angular velocity.

Fig. (4-4) indicates that the turbulence intensity is stronger near the propeller blade tip and hub wake region than other wake regions. The result without the nozzle indicates a higher turbulence level than the result with the nozzle. The thrusting region of the propeller wake is the region of low turbulence intensity. The results without the nozzle indicate that only the inner blades region (r/R <0.8) is thrusting and the blade tip region is not thrusting (stall condition). This is a result of the extreme blade section angle of attack due to the high thruster geometric pitch ratio.

It is clearly shown that the propeller blade working condition is improved by the introduction of the nozzle. The nozzle effect in accelerating the flow toward the propeller reduces the angle of attack. Subsequently, this reduces the total flow turbulence and improves the working condition of the propeller blades.

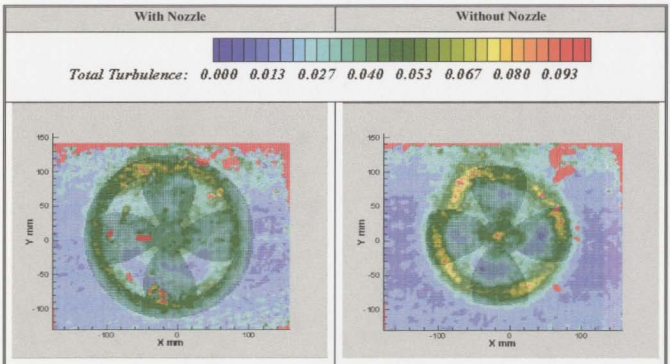

Figure 4-4: SPIV DP thruster wake total turbulence distribution at J= 0.4 and at X/D = 0.5

4-1-5: Flow Vorticity Distribution Around the DP Thruster

The propeller blade wakes could not be recognized from the mean flow velocity components shown in Figs. (4-1) and Fig. (4-2). However, the propeller blade wakes could be recognized from the vorticity distribution as shown in Fig. (4-5).

The maximum values of vorticity are found at the hub and propeller blade tip regions. The trailing vorticity, shed from the blade trailing edges, is easily identified and consists of two circular layers of opposite sign which overlap at about $r/R = 0.7$ at the blade section of maximum loading. This result was also obtained by Felli *et al.* (2002). It is difficult to identify the tip vortices in both the measurements with and without the nozzle, due to the high loading condition of the test.

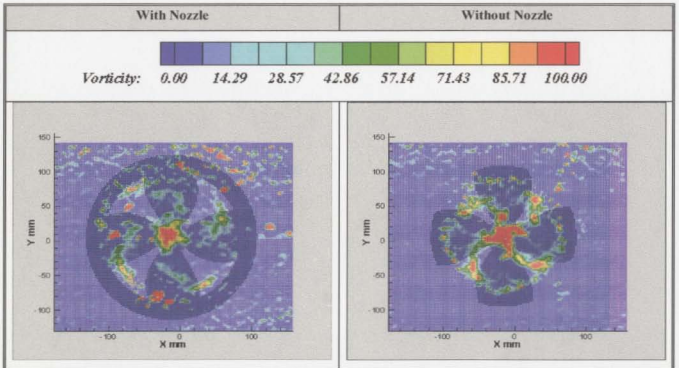

Figure 4-5: SPIV Vorticity distribution with and without the nozzle at $J = 0.4$ and at $X/D = 0.5$

4-2: Characteristics of the DP Thruster Near Wake Region

The near wake region is the region up to the contraction of the propeller wake. It is extended up to one diameter downstream of the propeller. In this study, the evaluation of the characteristics of the DP thruster near wake region is considered to be up to 1.5 diameters downstream. In this section, the hydrodynamic characteristics and the momentum and energy propagation of the DP thruster wake at different transverse downstream axial planes (X/D = 0.3, 0.5, 1.0 and 1.5), under varied operating conditions, are presented.

4-2-1: Characteristics of the DP Thruster Near Wake Velocity Distribution

Figs. (4-6) and (4-7) show the LDV and the SPIV near wake mean axial velocity distribution of the DP thruster wake at different axial downstream planes and at different advance coefficient values, respectively. The propagation of the DP thruster near wake axial flow velocity at different radial and downstream axial plans is shown in Fig. (4-8).

The evolution along the longitudinal axis of the axial velocity component for both measurements with and without the nozzle shows that the shape of the axial velocity profiles and the maximum velocity vary with axial distance.

Fig. (4-7) and Fig (4-8) show that the wake contraction of the DP thruster at the bollard pull operating condition take place at X/D =0.5. However, measurements at J=0.4 and J=0.45 show that the wake contraction between the first two LDV measurement planes, which are very close to each other and to the propeller plane, causes some axial acceleration, indicated by the higher axial velocity achieved in the second measurement plane (X/D = 1.0). Also, the near wake evaluation of the mean axial flow velocity shows

that as the advance coefficient decreases (propeller load increase), the magnitude of the axial velocity component is increased within the slipstream of the propeller. It is also noted that the contraction of the propeller slipstream behind the propeller is higher at J=0 than J=0.4 and J=0.45. These results imply that the contraction of the DP thruster slipstream occurs earlier in the case of bollard pull measurements than the measurements at J=0.4 and J=0.45. Therefore, as the advance coefficient is reduced the contraction of the slipstream occurs earlier.

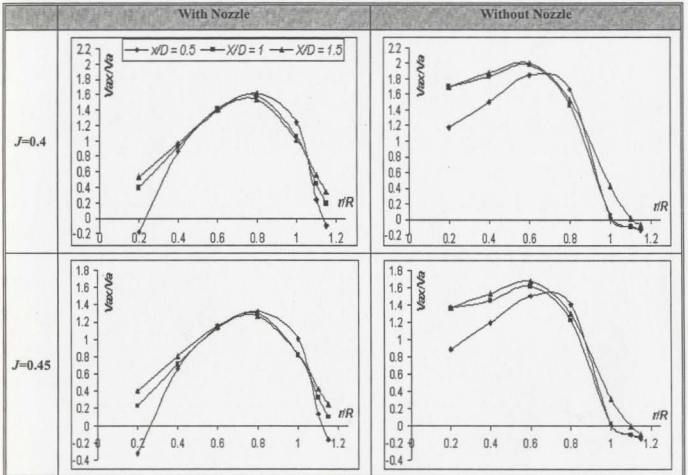

Figure 4-6: LDV near wake mean axial flow velocity evolution with and without the nozzle at J=0.4 and J=0.45

A reduction in the DP thruster wake axial velocity starts beyond the plane of contraction (X/D = 0.5 for J=0, and X/D =1 for J=0.4 and J=0.45). Also, the beginning of the slipstream broadening and expanding starts beyond the plane of contraction. Moreover, the near wake axial velocity propagation indicates a reduction in the longitudinal axial velocity as the advance coefficient increases.

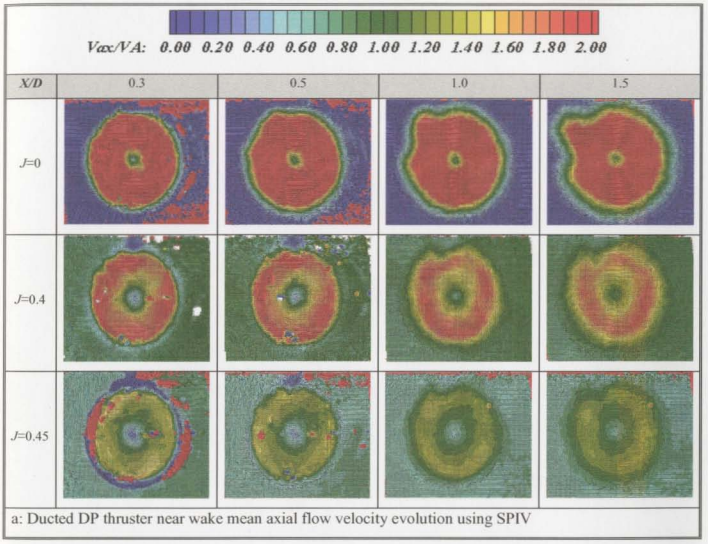

a: Ducted DP thruster near wake mean axial flow velocity evolution using SPIV

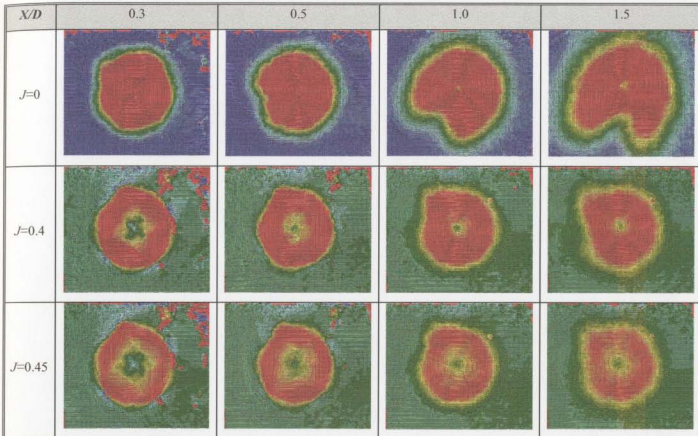

b: Open DP thruster near wake mean axial flow velocity evolution using SPIV

Figure 4-7: SPIV near wake mean axial flow velocity evolution with and without the nozzle at J=0, J=0.4 and J=0.45

Fig. (4-6) and Fig. (4-7) show that measurements with the nozzle have lower mean axial velocity values at similar radial and downstream axial positions than those without the nozzle. This is because the ducted propeller is more lightly loaded than the open propeller. It is also noted that the contraction of the propeller slipstream behind the propeller is less with the propeller in the nozzle than with the open propeller. This is due to the effect of the nozzle in reducing the displacement effect of the propeller wake, as will be shown from the analysis of the DP thruster wake momentum later in this chapter.

At the positions just downstream of the propeller, the axial velocities are almost zero at the inner propeller radii due to the influence of the propeller hub. This influence is clearly represented in Fig. (4-7), where the hub influence is reduced by a reduction in the advance coefficient value and an increase in the distance from the propeller. The open propeller results show lower influence to the hub effect than the ducted results. This is because of the higher contraction and load of the open propeller than the ducted propeller.

It can be seen from Fig. (4-7) that the velocity field close behind the axisymmetrical propeller is not axisymmetrical. This phenomenon occurs in both the ducted and the open propeller wake. The reason for this phenomenon is probably related to the influence of the propeller strut. The strut of the DP thruster model has a conical shape with a diameter larger than the propeller blade width and with a fin from the bottom side, as shown in Fig. (2-1). The large geometry of the strut affects the slipstream wake, as well as the downstream wake of the DP thruster. It can be seen from Fig. (4-7) that the strut influence region almost covers a section of 90^0 and that the angular position of this region moves with an increase in the axial distance to the propeller. The strut influence region changes its angular position and grows as the distance from the propeller is increased. It appears that the wake produced by the strut resembles a helix with a varying pitch. This phenomenon was also observed by Nienhuis (1992). The wake of the nozzle and the strut is more apparent at higher advance coefficient due to the higher advance velocity

Fig. (4-8) shows that the propagation of the open DP thruster axial flow velocity at r/R =0.2 to r/R= 0.6 indicates a higher value than the ducted DP thruster at the bollard

pull condition. A large drop in the open DP thruster axial velocity is noted at r/R =0.8. This result indicates that there is a high turbulent wake in this region, which decreases the induced axial velocity of the open DP thruster at r/R =0.8. It is clearly shown that the loss of the induced axial flow velocity at r/R =0.8 is improved by the ducted propeller and by the reduction in the advance coefficient value. This result is also shown in Fig. (4-9).

Up to r/R = 0.8 the propagation of the DP thruster near wake axial velocity shows a reduction in value as the X/D increases for the measurements at J=0. Measurements at J=0.4 and J= 0.45 show increases in the axial velocity up to X/D = 1.0, then a reduction in the axial velocity beyond this range up to r/R = 0.8.

At r/R =1.0, measurements of the open DP thruster indicate lower axial velocity than the ducted DP thruster wake at X/D=0.5. This is due to the mixing between the open DP thruster high turbulent flow and the viscous wake at the tip of the propeller blades. The effect of the viscous wake is reduced as the distance from the propeller increases. Therefore, there is an increase in the axial flow velocity at r/R =1.0 as the X/D increases.

The rate of the increase in the axial flow velocity at r/R 1.0 is higher in the case of the measurements at the bollard pull condition than the measurements at J=0.4 and J=0.45. Also, it is higher in the case of the open thruster than ducted thruster. These results indicate that the rate of the near wake energy decay increases as the advance coefficient decreases, and it is higher in the case of the open thruster than the ducted thruster.

Fig. (4-7) shows that the wake of the DP thruster becomes more organized as the advance coefficient increases. The blade wake at the inner radii and near the hub of the open DP thruster at J=0.4 and J=0.45 could be recognized. Also, the presence of the tip

vortex could be observed in the results of the open DP thruster at X/D=0.3 for J=0.4 and J=0.45. The tip vortices are appeared as four blue spots at the tip of the open DP thruster blades.

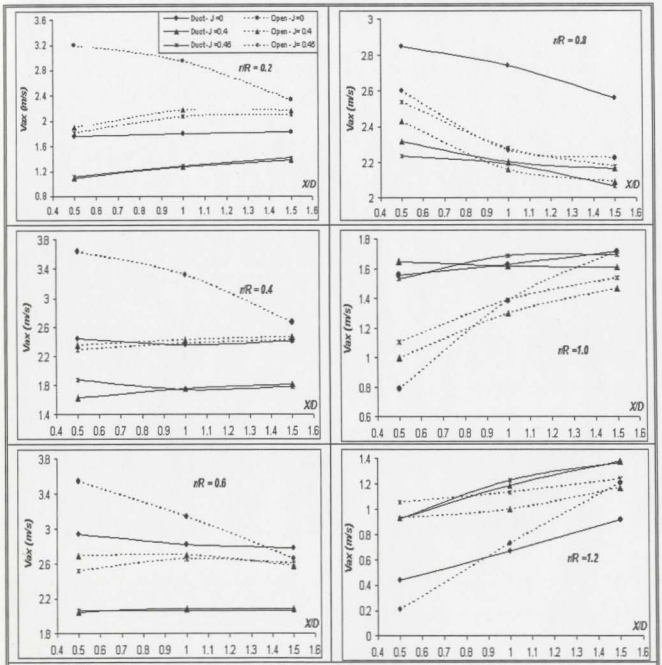

Figure 4-8: DP thruster near wake axial flow velocity propagation with and without a nozzle; and at J=0, J= 0.4 and J=0.45 (SPIV results)

4-2-2: Characteristics of the DP Thruster Near Wake Vorticity Distribution

Fig. (4-9) shows the DP thruster near wake vorticity distribution with and without a nozzle at J=0, J= 0.4 and J=0.45.

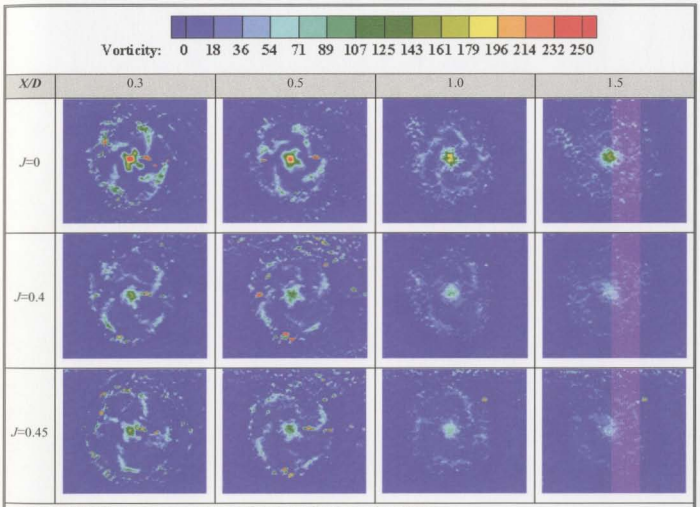

a: Ducted DP thruster near wake vorticity distribution using SPIV

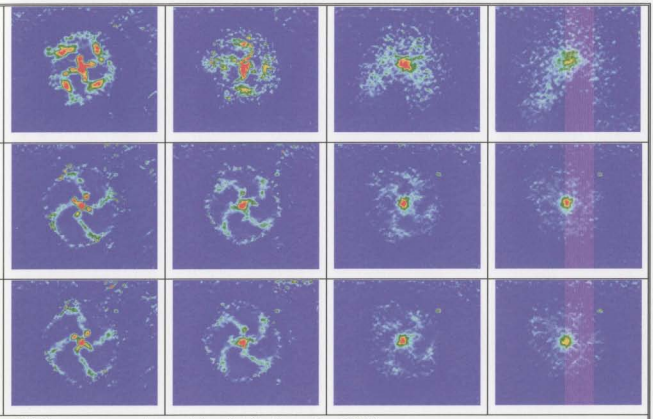

b: Open DP thruster near wake vorticity distribution using SPIV

Figure 4-9: SPIV DP thruster near wake vorticity distribution with and without the nozzle at J=0, J= 0.4 and J=0.45

The propeller blade wakes can be recognized from the flow vorticity distribution for both measurements with and without a nozzle up to X/D = 1.0 downstream of the propeller. Fig. (4-9) shows that the vorticity of the propeller wake increases as the propeller loading increases (lower advance coefficient) as expected, because it is strictly related to the circulation and to the pressure distribution along the blade span. Also, this indicates that the heavily loaded propeller loses more energy due to the formation of vorticity than that of lightly loaded propeller. Also, Fig. (4-9) shows that there is a rapid

reduction in the flow vorticity as the distance from the propeller increases. This implies a high rate of vorticity dissipation and diffusion in the near wake region.

In the all cases shown in Fig. (4-9), the hub vortex has the strongest vortex structure of the propeller wake. This is due to the strong roll up process of the hub vortex due to the strong acceleration of the radial velocity component near the propeller hub. Measurements with the nozzle show a weaker hub vortex with respect to the case without the nozzle pointing out the unloading effect of the nozzle on the propeller. The distance required for the vortex decay is proportional to the vortex intensity and occurs in the near wake region for J=0.4 and J=0.45 for the measurements with the nozzle, while the measurements without the nozzle point out the long life of the hub vortex which is still existing at the measurement plane X/D = 1.5.

4-2-3: Characteristics of the DP Thruster Near Wake Flow Turbulence Distribution

Fig. (4-10) shows the distribution of the DP thruster near wake total flow turbulence. The red and white spots in the images are due to spurious vectors, which were created due to light reflection. Measurements with and without a nozzle indicate a reduction in the total flow turbulence as the advance coefficient value and the distance from the propeller increase.

The ducted DP thruster results indicate a presence of an annular region of turbulence. This is due to the interaction of the nozzle wake with the blade tip wake. Also, there is no apparent trace of the tip vortices can be recognized from the ducted DP thruster near wake total turbulence distribution.

Fig. (4-10) indicates stronger turbulence intensity at the thruster tip and hub wake regions, specially at J=0, than the other wake regions and it is higher in the case of the open DP thruster results than the ducted thruster results. This implies that the outer blade regions are most likely stalled. However, as soon the advance coefficient increases coherent and organized flow structures are apparent showing the presence of the blade wake and the tip vortices that are rapidly dissipated in the downstream evolution.

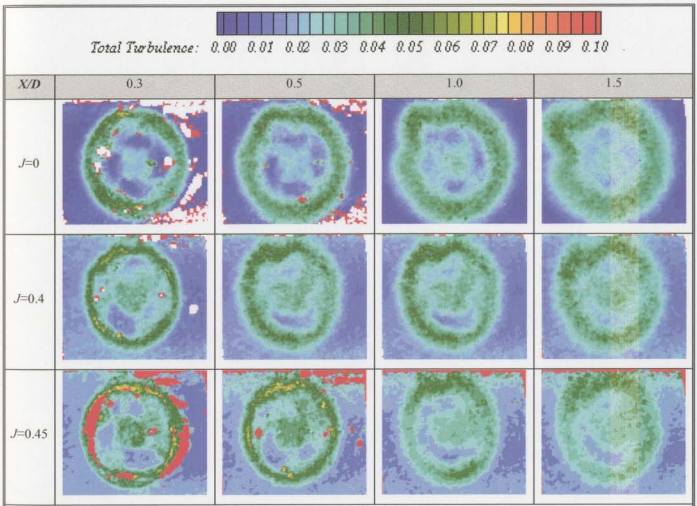

a: Ducted DP thruster near wake total turbulence distribution using SPIV

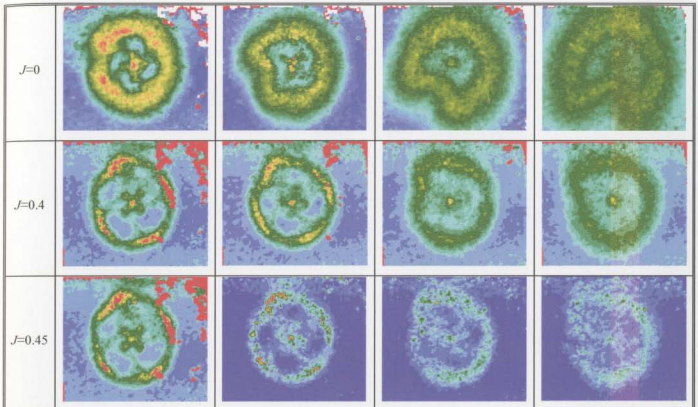

b: Open DP thruster near wake total turbulence distribution using SPIV

Figure 4-10: SPIV DP thruster near wake total turbulence distribution with and without the nozzle at J=0, J= 0.4 and J=0.45

4-2-4: Evaluation of the DP Thruster Near Wake Circulation

Circulation can be calculated from the distribution of mean tangential velocity in the wake of the propeller (Kerwin, 1982; Jessup, 1989) from:

$$\frac{\Gamma}{2\pi R V_A} = \frac{1}{K} \times \frac{r}{R} \times \frac{V_t}{V_A} \quad \text{---------- Eq. [4-2]}$$

where, Γ is the calculated circulation, which is normalized by advance velocity (V_A) and propeller radius (R). K is the number of propeller blades, r/R is the radius fraction and V_t/V_A is the normalized tangential velocity. The distribution of the DP thruster near wake

circulation with and without the nozzle is shown in Fig. (4-11) for the SPIV measurements and in Fig. (4-12) for the LDV measurements.

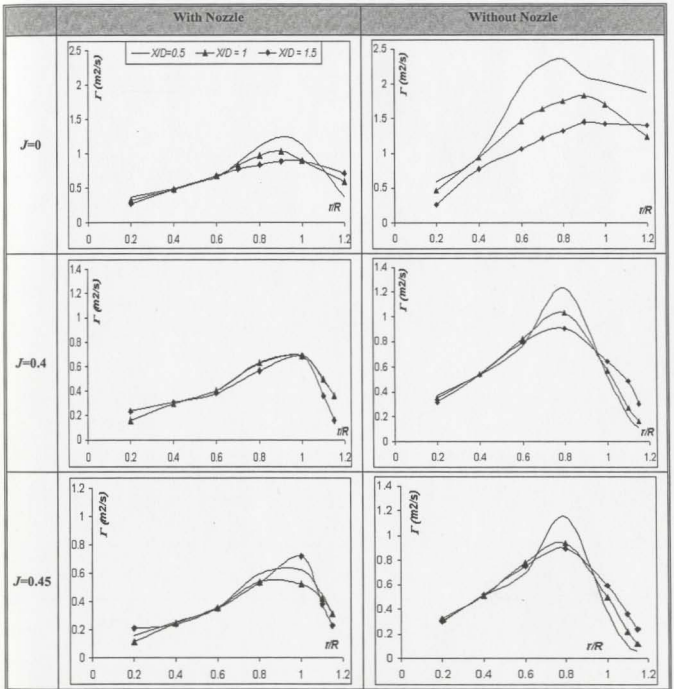

Figure 4-11: Near wake circulation distribution at different radial and downstream axial positions Using SPIV

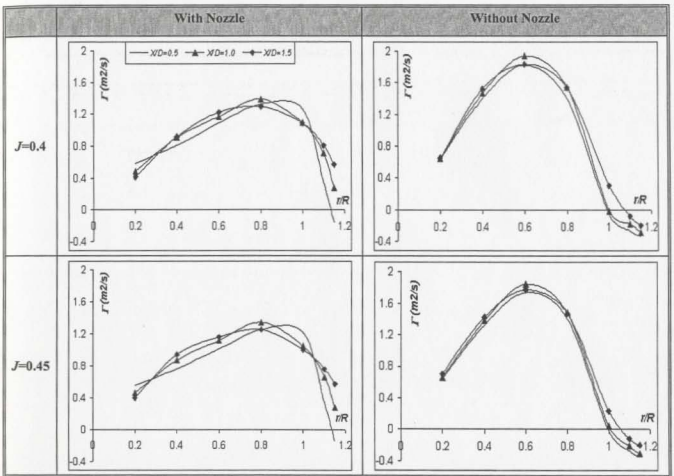

Figure 4-12: Near wake circulation distribution at different radial and downstream axial positions Using LDV

The results indicate a similarity in circulation distribution behavior from the different downstream positions. The near wake distribution of the circulation shows low values near the hub; increasing radially outward to reach a maximum value at about r/R = 0.8-1.0 for the measurements with the nozzle and at about r/R = 0.7–0.9 for the SPIV measurements without the nozzle. Fig. (4-12) shows that the maximum circulation of the measurements without the nozzle is at about r/R=0.6. The near wake distribution of flow circulation indicates a reduction in the flow circulation after the maximum value for both

the measurements with and without the nozzle. Fig. (4-11) and Fig. (4-12) show that the rate of reduction in the flow circulation is higher in the outer blade regions for the measurements without the nozzle than those with the nozzle. This implies that the outer blade regions of the open thruster are rapidly losing lift and are most likely stalled. Also, Fig. (4-11) and Fig. (4-12) show that the flow circulation of the open thruster has higher value than the ducted thruster, and the LDV measurements indicate higher flow circulation that the SPIV measurements.

Moreover, Fig. (4-11) and Fig. (4-12) show that the circulation increases as J is reduced, and reduces as X/D is increased. This latter could be due to viscous effects.

4-2-5: Evaluation of the DP Thruster Near Wake Flow Momentum

The propeller thrust and torque impart axial and swirl momentum to the propeller slipstream immediately behind the propeller disk. These momentum fluxes can be determined by integrating the measured mean velocity profile (Hyun and Patel 1991, Oh and Kang 1992). Integral parameters for the mass and momentum deficits are defined as follows:

$$m^{0'} = 2\pi\rho \int_0^{\delta} (V_A - V_X)\, r dr \qquad \text{(Kg/s)} \text{ ---------- Eq. [4-3]}$$

$$M'_{XX} = 2\pi\rho \int_0^{\delta} V_X (V_A - V_X)\, r dr \qquad \text{(kN)} \text{ ---------- Eq. [4-4]}$$

$$M'_{\theta X} = 2\pi\rho \int_0^{\delta} V_X V_t\, r dr \qquad \text{(kN)} \text{ ---------- Eq. [4-5]}$$

where, $m^{0'}$ is the mass flow deficit, M'_{XX} is the momentum flux deficit in the x direction, and M'_{OX} is the swirl (tangential) flux deficit in the x direction. The value δ is the radial

distance at which the axial velocity becomes equal to the free stream velocity. Eq. (4-6), Eq. (4-7) and Eq. (4-8) represent the normalized form of these parameters.

$$m^{0} = \frac{2\pi}{V_A D^2}\int_0^{\delta}(V_A - V_X)\,r dr \qquad \text{Eq. [4-6]}$$

$$M_{xx} = \frac{2\pi}{V_A^2 D^2}\int_0^{\delta} V_X (V_A - V_X)\,r dr \qquad \text{Eq. [4-7]}$$

$$M_{\theta x} = \frac{2\pi}{V_A^2 D^2}\int_0^{\delta} V_X V_t\, r dr \qquad \text{Eq. [4-8]}$$

where, V_x and V_t are normalized by the velocity of advance (V_A), ρ is normalized by ρ, and r is normalized by the propeller diameter (D).

The calculation process of these parameters may include errors due to the uncertainty in estimating δ, and the axial and tangential velocity profile at each operating condition. The estimated values of these parameters for the DP thruster near wake region with and without the nozzle is shown in Fig. (4-13) for J= 0, J= 0.4 and J= 0.45.

The results indicate some common features between the distributions of the flow mass deficit, the axial momentum flux deficit, and the swirl flux deficit of the measurements with and without the nozzle. The distribution of these parameters shows increasing values in the near wake region, reaching a maximum value at X/D = 1, then remaining nearly constant beyond this position. Fig. (4-13) shows that there is a reduction in these parameters as the advance coefficient increases. This can be explained due to an increase in the DP thruster ambient flow velocity and a reduction in the level of which DP thruster flow is displaced outward as the advance coefficient increases. Therefore, the flow dissipation rate increases as the advance coefficient decreases.

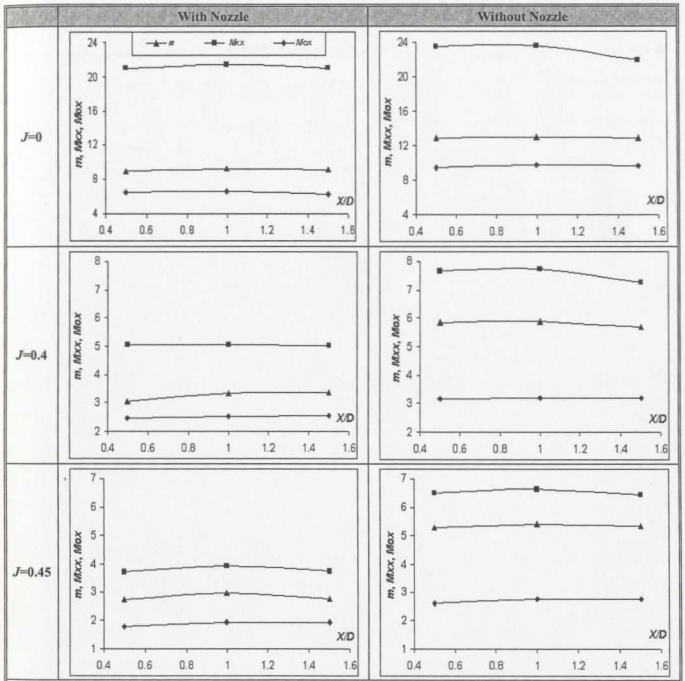

Figure 4-13: Distribution of the mass deficit, and axial and swirl momentum flux deficits with and without the nozzle (SPIV results)

The mass flow deficit is a measure of the displacement effect of the viscous flow. By comparing the distribution of the DP thruster mass flow deficit with and without the

nozzle, it is clearly shown that the displacement effect of the propeller wake is reduced by the presence of the nozzle. This indicates that the contraction of the propeller slipstream behind the propeller is less with the propeller in the nozzle, than with the open propeller.

The distribution of the axial momentum flux is related to the propeller thrust. Fig. (4-14) shows the distribution of the propeller thrust at different downstream axial positions with and without the nozzle. The flow thrust of the DP thruster is estimated using Eq. (4-6):

$$\textbf{Thrust} = 2\pi\rho \int_0^{r/R} V_X{}^2 \, r \, dr \qquad \text{----------Eq. [4-9]}$$

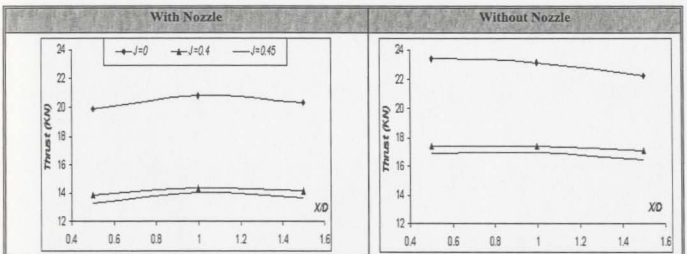

Figure 4-14: DP thruster near wake flow thrust propagation with and without a nozzle at J=0, J=0.4 and J= 0.45 (SPIV results)

Fig. (4-14) shows that the thrust produced from the propeller without the nozzle is higher than that with the nozzle and it has the same distribution features of the axial momentum flux.

4-2-6: Evaluation of the DP Thruster Near Wake Energy Propagation

The rate of energy dissipation can be investigated from the propagation of the flow shape factor (H). The shape factor is defined as the ratio of the flow displacement thickness (m^0) to the flow momentum thickness (M_{xx}). The value of the shape factor gives an indication of how prone a boundary layer is to separation. The smaller value of the shape factor implies higher transverse momentum exchange and more kinetic energy in the flow.

Fig. (4-15) shows the distribution of the calculated flow shape factor of the DP thruster near wake with and without a nozzle at the test advance coefficient values. The results of the ducted and open thruster show that there is an increase in the DP thruster near wake shape factor as the advance coefficient and distance from the propeller both increase. These results imply that there is a reduction in the DP thruster near wake total flow energy and total flow turbulence as the advance coefficient and the distance from the propeller increase.

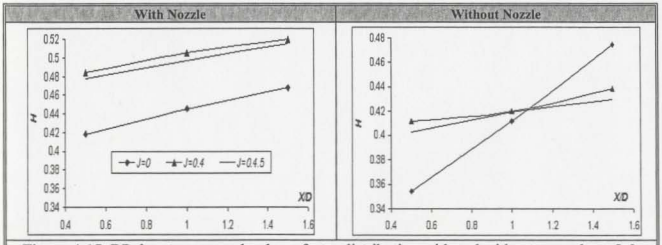

Figure 4-15: DP thruster near wake shape factor distribution with and without a nozzle at J=0, J= 0.4 and J=0.45 (SPIV results)

The near wake evaluation of the DP thruster shape factor indicates that the open DP thruster wake has higher energy than the ducted DP thruster wake with the same advance coefficient, as shown in Fig. (4-16). It is clear from Fig. (4-16) that the DP near wake energy decay rate is higher in the case of the open thruster than the ducted DP thruster.

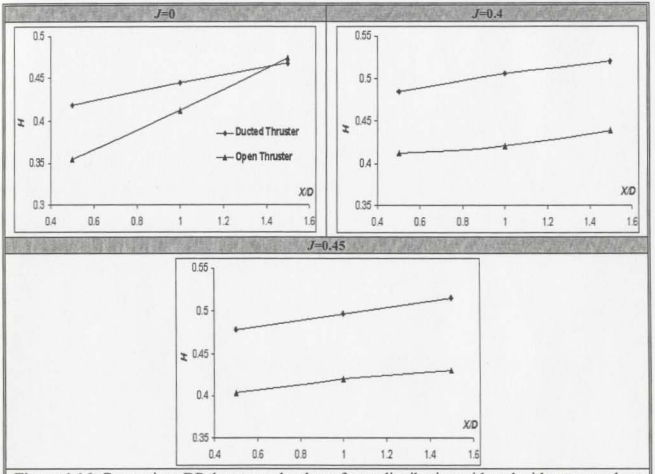

Figure 4-16: Comparison DP thruster wake shape factor distribution with and without a nozzle at J=0, J=0.4 and J=0.45 (SPIV results)

The evaluation of the DP thruster near wake characteristics shows that the rate of change in the flow velocity, vorticity, total turbulence, momentum, thrust, and energy

among the measuring planes when moving downstream the propeller, is higher in the case of the open thruster than the ducted thruster. This result implies that the DP thruster near wake region energy decay rate is higher in the case of the open thruster than the ducted thruster.

4-3: Characteristics of the DP Thruster Far Wake Region

The far wake region is the region where the variations in the wake are relatively slow. In fact, the far wake can be thought of as that region where the wake decays slowly and steadily. This can be seen in Fig. (4-17), which shows the propagation of the DP thruster far wake mean axial flow velocity at r/R= 0.6 with and without the nozzle, up to 15 diameters downstream, and at J= 0 and J= 0.4. As shown, there is a high reduction in the axial velocity value in the near wake region and this reduction is furthermore taking place when moving downstream of the propeller.

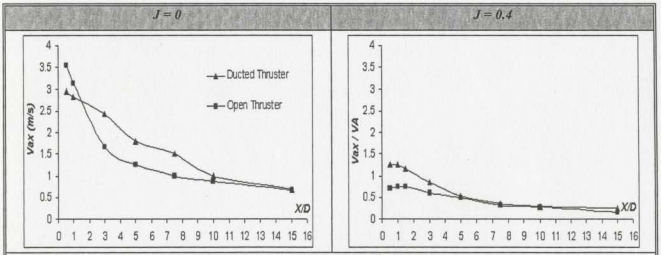

Figure 4-17: Propagation of the axial velocity for the DP thruster wake with and without a nozzle at r/R = 0.6 (SPIV results)

The DP thruster far wake velocity measurements were performed up to $X/D = 15$ using the SPIV system. In this section, the ducted and open DP thruster far wake hydrodynamic characteristics, momentum propagation, and energy evaluation at different advance coefficient values ($J= 0$ and $J= 0.4$) and transverse downstream axial planes (X/D =3.0, 5.0, 10.0 and 15.0) are presented.

4-3-1: Characteristics of the DP Thruster Far Wake Velocity Distribution

Fig. (4-18) shows the far wake distribution of the mean axial flow velocity evolution for the DP thruster with and without the nozzle at $J= 0$ and $J= 0.4$. The evolution along the longitudinal axis of the axial velocity component for both measurements with and without the nozzle shows unstable fluctuation of the slipstream in the downstream region. Measurements performed in phase with the propeller blade point out that a strong deformation of the slipstream. The deformation already seen in the near wake is amplified in the downstream evolution. This phenomena is more apparent for the case without the nozzle and at $J=0$ indicating that a possible relation of the wake deformation mechanism with the blade loading exist.

The propagation of the DP thruster far wake at different radial and downstream axial planes is shown in Fig. (4-19). The distribution of the DP thruster axial flow velocity at different radial location with and without the nozzle indicates a reduction in values as the distance from the propeller increases due to the fact that the flow rate is distributed on a large area. The rate of the axial velocity flow reduction rate is higher in the case of the bollard pull measurements than the measurements at $J=0.4$ because of the

higher diffusion process due to the higher turbulence levels observed in such cases in the near wake region.

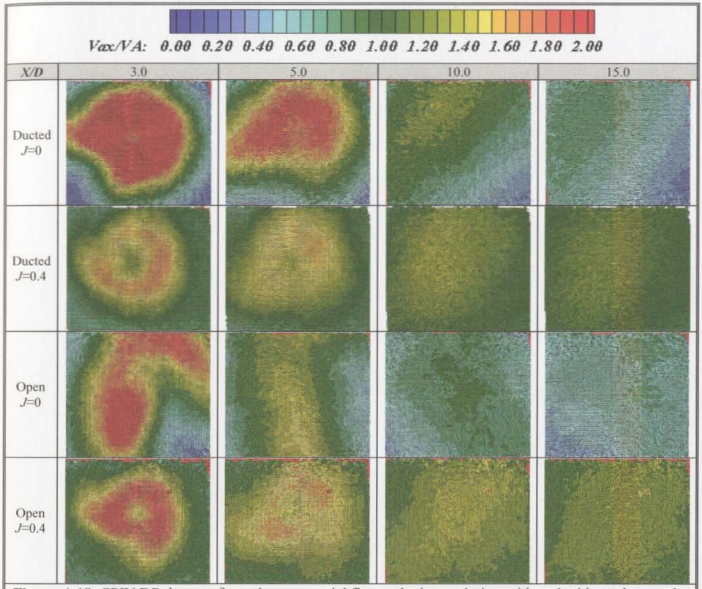

Figure 4-18: SPIV DP thruster far wake mean axial flow velocity evolution with and without the nozzle, and at J=0 and J=0.4

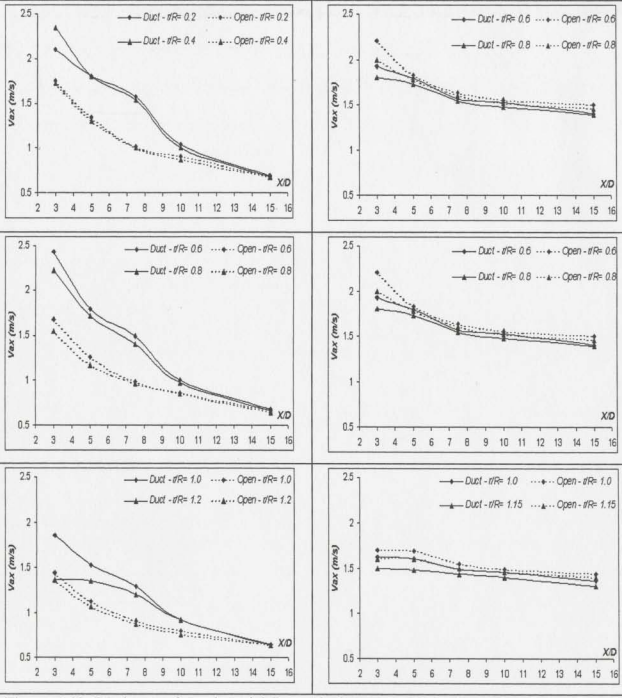

Figure 4-19: DP thruster far wake axial flow velocity propagation with and without a nozzle, and at J=0 and J=0.4 (SPIV results)

Fig. (4-18) shows that the wake of the ducted DP thruster has higher axial flow velocity than the wake of the open DP thruster at the bollard pull operating condition. However, the results at J=0.4 show the opposite. This is due to the effect of the duct thrust contribution to the total thrust of the ducted DP thruster discussed in the last chapter. At the bollard pull condition, the duct contributes about 50% of the total thrust of the ducted DP thruster, and this contribution is decreased as the advance coefficient is increased. This caused a reduction in the ducted DP thruster induced axial velocity as the advance coefficient increases.

By comparing the results of the ducted and the open DP thruster wake axial velocity value at X/D =15 shown in Fig. (4-19), the results show that the ducted DP thruster has higher axial velocity than the open DP thruster at J=0. Therefore, at the bollard pull operating condition the wake of the ducted DP thruster persists further downstream than the open DP thruster wake. Also, the far wake evaluation of the open and ducted DP thruster axial flow velocity at X/D =15 show that the results at J=0.4 have higher axial flow velocity than the results at the bollard pull operating condition. Thereby, the wake of the ducted and open DP thruster persists further downstream as the advance coefficient value increases.

Fig. (4-18) shows that the flow loses its identity when moving downstream from the propeller. As the distance behind the propeller increases, the gravitational effect on the displaced fluid becomes more dominant and results in a vertical collapse and a horizontal growth in the wake region. As expected from the DP thruster near wake momentum analysis, the width of the DP thruster wake increases as the distance from the

propeller increases and the rate of increase is higher in the case of the bollard pull condition than J=0.4.

Also, Fig. (4-18) indicates that the reduction and the fluctuation in the axial velocity among the measured axial planes when moving downstream from the propeller are reduced as the advance coefficient increases. Therefore, it is expected that the wake of the DP thruster will persist further downstream as the advance coefficient increases.

4-3-2: Characteristics of the DP Thruster Far Wake Vorticity Distribution

The distribution of the DP thruster far wake flow vorticity is shown in Fig. (4-20). The vorticity evaluation in the far wake region was performed at values lower than that in the near wake region in order to capture the profile of the flow vorticity distribution, which reduces rapidly when moving downstream of the propeller.

Fig. (4-20) shows that only the hub vortices of the DP thruster far wake vorticity distribution could be captured at the X/D =3.0 and there is no substantial flow vorticity beyond X/D =5.0. These results indicate that the flow become less rotational when moving downstream from the propeller. This gives an indication of the level of the wake energy decay.

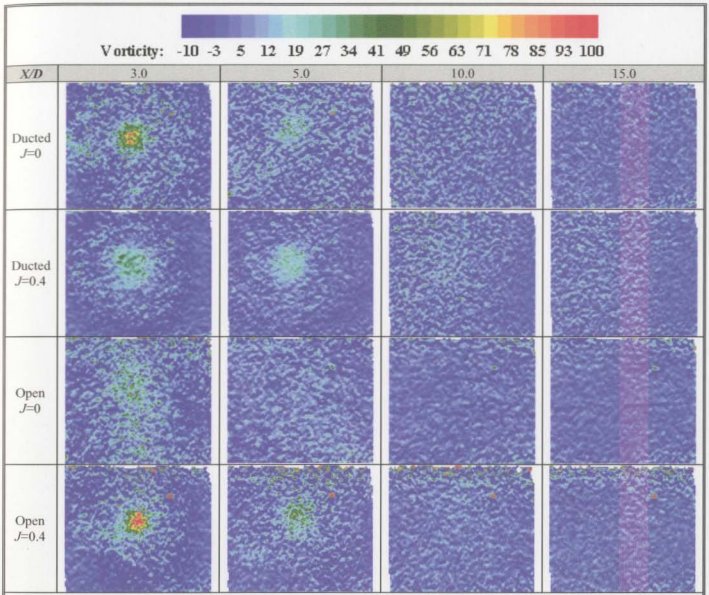

Figure 4-20: SPIV DP thruster far wake vorticity evolution with and without the nozzle, and at J=0 and J=0.4

4-3-3: Characteristics of the DP Thruster Far Wake Total Turbulence Distribution

The distribution of the DP thruster far wake total flow turbulence is shown in Fig. (4-21). Measurements without the nozzle indicate higher turbulence intensity and fluctuation than those with the nozzle.

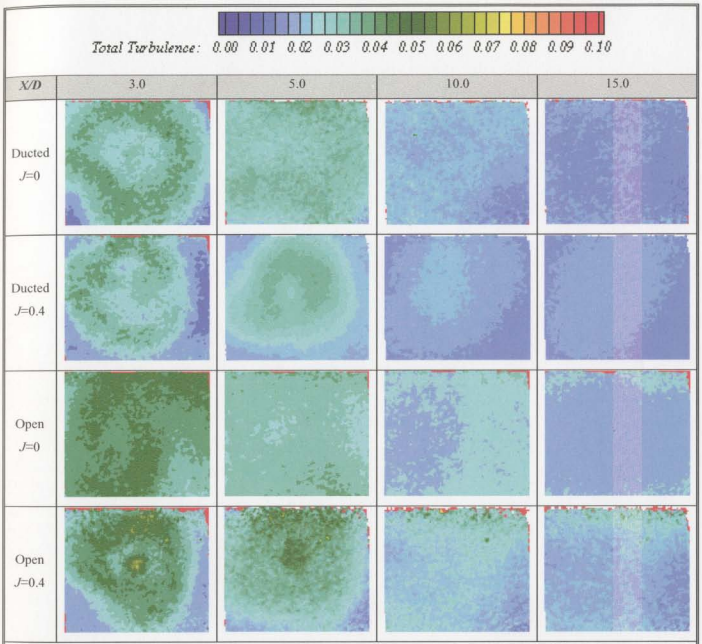

Figure 4-21: SPIV DP thruster far wake total flow turbulence evolution with and without the nozzle, and at J=0 and J=0.4

The propagation of the DP thruster far wake total turbulence indicates that measurements at J=0.4 have a higher flow total turbulence beyond X/D =3.0 than measurements at J=0. This result gives an indication that the flow of the DP thruster

persists further downstream as the advance coefficient value increases. Also, the DP thruster far wake total flow turbulence is reduced from about 7% at X/D = 3.0 to around 1.5% at X/D= 15. This gives an indication that the flow in the far wake region is almost laminar.

4-3-4: Evaluation of the DP Thruster Far Wake Flow Circulation

The distributions of the DP thruster far wake circulation at different radial and downstream axial planes were calculated using Eq. (4-2) and are shown in Fig. (4-22).

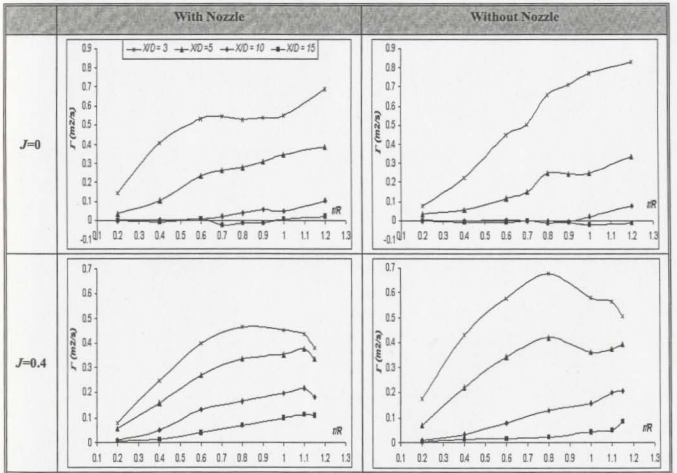

Figure 4-22: DP thruster far wake circulation distribution at different radial and downstream axial positions, and at J=0 and J=0.4 (SPIV results)

The results shown in Fig. (4-22) indicate that measurements with the nozzle have lower flow circulation at different radial and downstream axial positions than those without the nozzle. This is because the ducted propeller is more lightly loaded than the open propeller. Also, Fig. (4-22) shows that the flow circulation is decreased as the distance from the propeller is increased. The results at J=0 indicate lower (almost zero) flow circulation than those at J=0.4 beyond X/D =5.0. This result implies that the rate of decay in the DP thruster far wake tangential velocity is increased as the advance coefficient is reduced. Also, it indicates that the DP thruster far wake region is more or less irrotational flow.

4-2-5: Evaluation of the DP Thruster Far Wake Flow Momentum

Fig. (4-23) shows the estimated values of the DP thruster far wake distributions of the flow mass deficit, the axial momentum flux deficit, and the swirl momentum flux deficit of the measurements with and without the nozzle. These parameters were estimated using Eq. (4-3), Eq.(4-4) and Eq. (4-5) respectively.

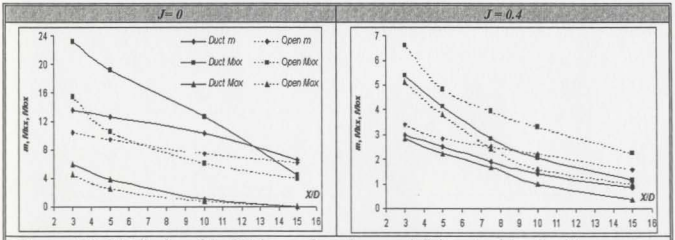

Figure 4-23: Distribution of the DP thruster far wake mass deficit, and axial and swirl momentum flux deficits with and without the nozzle, and at J=0 and J=0.4 (SPIV results)

The DP thruster far wake distribution of these parameters shows reduction in values as the distance from the propeller is increased. As the distance from the thruster increases the rate of DP thruster wake diffusion increases, therefore, the flow mass deficit reduces. Also, as the distance from the thruster increases the rate of reduction in the thrust and flow vorticity are increased. This is why the axial momentum flux deficit, and the swirl flux deficit of the measurements with and without the nozzle decrease as the distance from the thruster increases.

The distribution of the swirl momentum flux deficits at J=0 shown in Fig. (4-23) indicates zero value at X/D =15 for the measurements with and without the nozzle. This result implies that the flow has stopped rotating at and beyond X/D = 15. However, measurements at J=0.4 indicate small positive swirl momentum at X/D=15 for the measurements with and without the nozzle. This indicates that the flow is still rotational flow and the rate of flow rotational is higher in the case of open thruster than the ducted thruster.

Fig. (4-23) shows that the estimated values of these parameters at the bollard pull condition indicate higher value in the case of the ducted DP thruster than the case of the open thruster. This is because to the rate of energy dissipation of the DP thruster, which is higher in the case of the open DP thruster than the ducted DP thruster at the bollard pull operating condition. However, the distribution of these parameters at J=0.4 indicates higher value in the case of the open DP thruster than the case of the ducted DP thruster. This is due to the difference between the total thrust produced from the ducted and open DP thruster at J=0 and J=0.4, which can be figured out from the comparison between the DP thruster far wake thrust propagation with and without a nozzle at J=0 and J = 0.4 as

shown in Fig. (4-24). Fig. (4-24) shows that the thrust generated from the ducted DP thruster at J= 0 is higher than the open DP thruster. While, the results of the DP thruster thrust distribution at J=0.4 indicates the opposite.

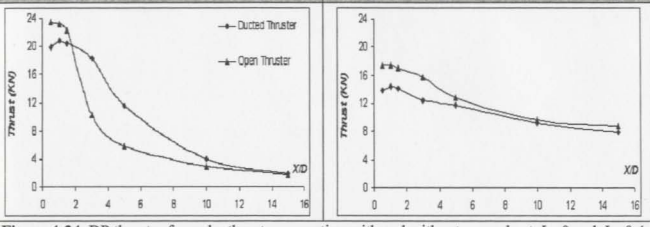

Figure 4-24: DP thruster far wake thrust propagation with and without a nozzle at J = 0 and J = 0.4 (SPIV results)

Fig. (4-25) shows a comparison between the distribution of the flow mass deficit, the axial momentum flux deficit, and the swirl momentum flux deficit of the measurements with and without the nozzle at J=0 and J=0.4. Fig. (4-25) shows that the rate of reduction of these parameters is higher in the case of J=0 than the case of J=0.4. This gives an indication that the rate of the DP thruster far wake energy decay, diffusion and dissipation increases as the advance coefficient is decreased.

Also, Fig. (4-25) shows that the rate of degradation of the mass deficit and the axial momentum flux deficits is larger in the case of the bollard pull condition than the case at J=0.4. This result can also be pointed out from the comparison between the DP thruster far wake thrust propagation at J=0 and J=0.4 shown in Fig. (4-26). Fig. (4-26) shows that the DP thruster far wake thrust at X/D =15 are higher in the case of the DP

thruster at J=0.4 than in the bollard pull condition. This result ensures that as the advance coefficient is increased the flow of propeller will persist to further distance downstream.

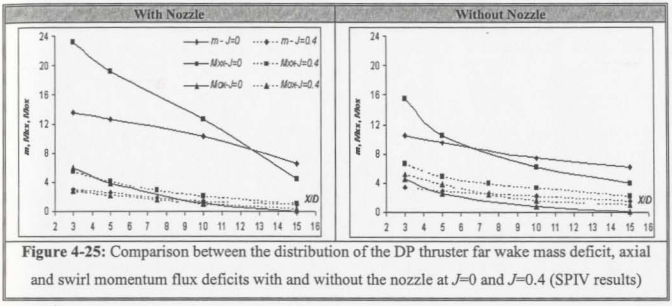

Figure 4-25: Comparison between the distribution of the DP thruster far wake mass deficit, axial and swirl momentum flux deficits with and without the nozzle at J=0 and J=0.4 (SPIV results)

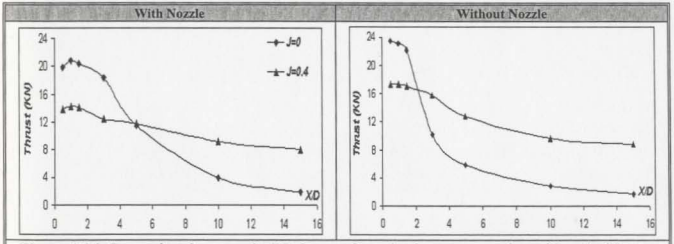

Figure 4-26: Comparison between the DP thruster far wake thrust propagation with and without a nozzle at J = 0 and J = 0.4 (SPIV results)

4-3-6: Evaluation of the DP Thruster Far Wake Energy Propagation

The estimated value of the DP thruster far wake shape factor with and without a nozzle at J=0 and J=0.4 is shown in Fig. (4-27).

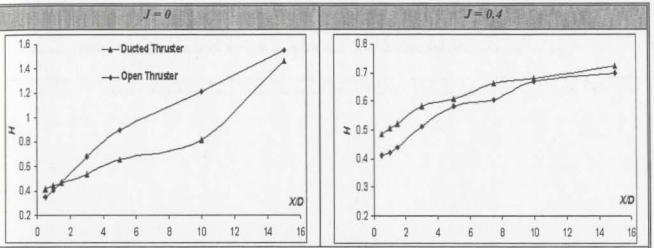

Figure 4-27: DP thruster far wake shape factor distribution with and without a nozzle, and at J=0 and J=0.4 (SPIV results)

The distribution of the DP thruster far wake shape factor at the bollard pull condition indicates that the ducted DP thruster has a lower value than the open DP thruster. This means that at the bollard pull operating condition the ducted DP thruster far wake has higher energy than the open DP thruster wake. Therefore, the wake of the ducted DP thruster will persist further downstream than the wake of the open DP thruster at the bollard pull operating condition.

On the other hand, the distribution of the DP thruster shape factor at J=0.4 indicates that the wake of the ducted DP thruster has a lower value than the wake of the open DP thruster. Therefore, the wake of the open DP thruster will persist further downstream than the wake of the ducted DP thruster at advance ratio higher than J=0. This is due to the contribution of the duct thrust to the total thrust of the ducted DP thruster, which is reduced as the advance coefficient increases.

The comparison between the ducted and open DP thruster far wake shape factor distribution at J=0 and J=0.4 shown in Fig. (4-28) indicates that an increase in the

advance coefficient value results in a reduction in the rate of the wake energy decay and dissipation rate. Also, the comparison between the shape factor value at the X/D =15 indicates that the result at J=0.4 has lower wake shape factor value than the result at J=0. This result means that at X/D=15 the energy of the DP thruster wake at J=0.4 is higher than at the bollard pull condition. Therefore, the DP thruster wake will persist further downstream as the advance coefficient increases.

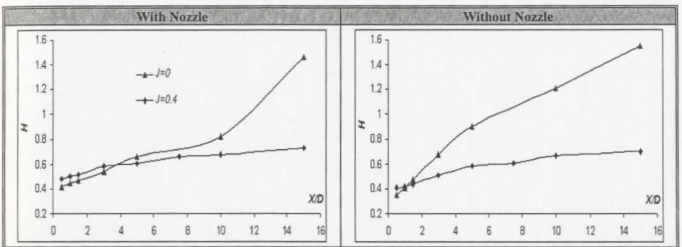

Figure 4-28: Comparison between the DP thruster far wake shape factor distribution with and without a nozzle at $J = 0$ and $J = 0.4$ (SPIV results)

These results could also be investigated from tracking the change in the axial flow velocity downstream the propeller. Fig. (4-29) shows the distribution of the open and ducted DP thruster wake axial flow velocity ratio at different downstream axial positions and advance coefficient values (J=0 and J=0.4). The axial velocity ratio is the ratio of the average axial velocity at any downstream axial plane to its value at X/D = 0.5 (V_d). Fig. (4-29) shows that the rate of reduction in the ducted DP thruster far wake axial flow velocity is lower than the open DP thruster, and the rate of the DP thruster far wake axial flow velocity reduces as the advance coefficient is increased.

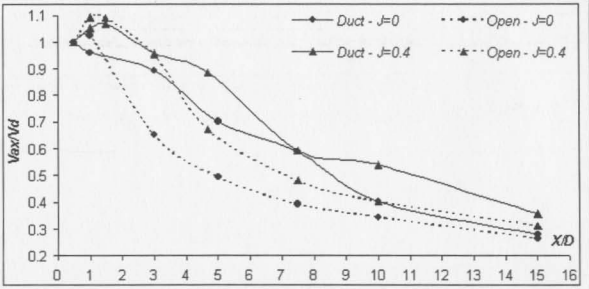

Figure 4-29: Propagation of the DP thruster wake axial velocity ratio at different downstream axial plans, with and without a nozzle, and at J=0 and J=0.4 (SPIV results)

4-4: Evaluation of the DP Thruster Wake Load on Structures in the Slipstream

The location of the DP thrusters, below the hull or placed in tunnels crossing the hull from one side to the other, affects any structures behind and downstream of their operation. When DP thrusters are in operation, they create a water jet current behind and downstream of the thruster. Any structures downstream (production pipelines, moorings,..etc) are subjected to this current wash or momentum impacts. These impacts create fluid loading on these structures. This fluid loading can be computed as a fluid drag force as indicated in Eq. (4-7).

$$\textbf{Drag Force} = 0.5 \cdot C_D \cdot \rho \cdot A \cdot V^2 \quad \text{(N)} \quad \text{..... Eq. [4-7]}$$

where C_D is the drag coefficient, ρ is the water density, A is the structure cross-sectional area, and V is the flow velocity.

This drag force increases the load acting on structures in the slipstream, and hence, any damage that may occur to these structures will affect the environment, the productivity, and the reliability of the offshore projects.

The propagation of the DP thruster wake loading force ratio at different downstream axial planes, with and without a nozzle and at J=0 and J= 0.4 is shown in Fig. (4-30). Fig. (4-30) shows the ratio between the drag force at any downstream axial plane to the drag force at X/D=0.5 assuming constant drag coefficient, water density and structure cross-sectional area. Therefore, the percentage of the drag force ratio at any downstream location is equivalent to the percentage of the square of the DP thruster wake velocity at this location to the square of the DP thruster wake velocity at X/D=0.5.

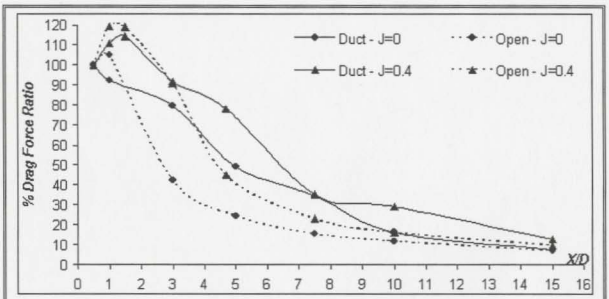

Figure 4-30: Propagation of the DP thruster wake loading force ratio at different downstream axial plans, with and without a nozzle, and at J=0 and J=0.4 (SPIV results)

Table (4-1) shows the rate of reduction in the DP thruster wake loading force at different downstream axial planes as a percentage of the wake loading force at X/D=0.5.

X/D	Ducted Thruster		Open Thruster	
	J= 0	J= 0.4	J= 0	J= 0.4
0.5	0.00	0.00	0.00	0.00
1.0	7.70	-10.64	-4.92	-19.20
3.0	20.18	8.13	57.67	9.10
5.0	50.93	21.70	75.56	54.94
7.5	65.49	64.79	84.58	76.88
10	83.77	70.90	88.16	83.84
15	92.60	87.19	92.97	90.22

Table 4-1: Percentage rate of reduction in the DP thruster wake loading force as the distance from the propeller increases

Fig. (4-30) shows that both the open and the ducted DP thruster results indicate increasing in the wake loading force in the near wake region, then a reduction in the wake loading force is indicated as moving downstream of the thruster. Table (4-1) shows that the rate of degradation in the DP thruster wake loading force is higher in the case of the open thruster than the ducted thruster, and this rate in increased as the advance coefficient reduces. Therefore, if the thruster is used as a dynamic positioning device, any structure placed in the near wake region will be subjected to a high level of dynamic forces.

In order to have a reliable, safe, productive and environmental friendly operation of DP offshore projects, the DP thruster wake loading effect should be taken into consideration in the early stage of design of structures in the slipstream of the DP thrusters wake. For the existing DP offshore projects, more attention and monitoring of the structures in the near wake region of DP thrusters should be taken to avoid any unexpected damage to these structures.

CHAPTER 5

COMPUTATIONAL FLUID DYNAMIC SIMULATIONS

Simulation of the flow field around a DP thruster requires software that can solve the discretized Navier-Stokes equations including the effect of turbulence.

Numerical simulation of the DP thruster far wake was performed using FLUENT-6.0. FLUENT is a finite volume general-purpose code for modeling fluid flow, heat transfer, and chemical reactions. It can perform calculations of the discretized Reynolds Averaged Navier-Stokes (RANS) equations including viscous effects, turbulence modeling, and free surface constraints on unstructured adaptive grids.

In this chapter, an introduction to the concept and the structure of CFD and the structure of the FLUENT 6.0 solver are given. Examples simulation of the DP thruster far wake with and without a nozzle at advance coefficient values of 0 and 0.4 using FLUENT 6.0 are also given.

5-1: The Concept of Computational Fluid Dynamics

CFD is a computational technology that enables the study of the hydrodynamics of a flow. It is a sophisticated analysis technique which not only predicts fluid flow behavior, but can also predict the transfer of heat, mass, phase change, chemical reaction, and mechanical movement depending on the program code.

CFD is used to predict the fluid velocity distribution by solving the fundamental equations of motion using numerical methods. Usually the fluid body is divided into cells or elements forming a grid. Then equations for the unknown variables are solved for each cell, which requires a substantial amount of computing resources. An advantage of this approach is that it has the potential to remove the difficulties associated with experimental methods. The fundamental equations for fluid flow, which describe the conservation of mass and momentum, are the equation of continuity and the Navier-Stokes equations. In practice, it is impossible to solve these equations directly since the fastest supercomputer with the largest memory available falls short of the required performance by many orders of magnitude (Bull, 1996).

5-2: Numerical Considerations

CFD is a comprehensive field covering a broad range of related topics. This section is intended to introduce the primary aspects of CFD.

5-2-1: Grids

A basic concept of CFD is to divide the fluid geometry into elements or cells, and then solve an equation for each cell. Meshing is an important step in any computational method in which the accuracy of solution can be directly related to the size and shapes of the mesh elements.

Grids can be classified according to several characteristics:

1- ***Shape***: the shape of the cells is usually triangular or quadrilateral as shown in Fig.(5-1).

2- ***Orthogonality***: the orthogonality of the grid is determined by the angle between the crossing grid lines. If the angle is 90^0, the grid is orthogonal. If it is different from 90^0, the grid is non- orthogonal.

Figure 5-1: Triangular and Quadrilateral Cell Shapes

3- ***Structure***: grids can be structured or non-structured.

The structure of the grid is the most important feature of the grid. Structured grids are currently the most common in CFD applications. This type of mesh requires a systematic scheme of node and element numbering related to the generation of the grid. The structured meshes do not require high computer memory because a map of the grid structure does not need to be stored. Also, the structured meshes allow the use of more efficient solution methods, which can reduce computer-processing time.

In spite of these advantages, it can be difficult to create complex geometries using structured meshes. Therefore, unstructured meshes are used for complex geometries instead of structured meshes. Unstructured grids are flexible, useful for complex geometries, and can be constructed with any type of element or with combinations of different element types. The combination of orthogonal and non-orthogonal elements is called a hybrid mesh. The application of unstructured hybrid meshes can greatly accelerate the meshing process of a CFD simulation. The disadvantages of this method are the increased computational resources required, and the fact that solvers have to be designed specially to handle unstructured meshes (Thornhill, 2002).

5-2-2: Solution Techniques

The concept of any CFD program is to solve the fundamental equations of motion using numerical methods. The equations of motion here are the Navier-Stokes equations, and CFD uses different numerical techniques or approaches to solve these equations. The Navier-Stokes equations governing the conservation of mass and momentum of fluid are a set of coupled, non-linear, mixed elliptic-parabolic partial differential equations (Versteeg *et al.*, 1995).

Exact solution cannot be determined for practical flows. Therefore it is necessary to employ numerical methods to develop approximate solutions to these equations. The solution process of the Navier-Stokes equations can be done in various ways. Well-known methods are: Finite Difference Methods (FDM), Finite Element Methods (FEM), Finite Volume Methods (FVM), and Spectral Element Methods (SEM). The basic steps for each of these methods can be summarized as:

- Use of a simple function to approximate unknown flow variables.
- Discretizing the governing flow equations with substitutions of the approximate functions followed by mathematical manipulations
- Solving the resulting algebraic equations.

5-2-3: Turbulence Modeling

Turbulent flows are characterized by fluctuating velocity fields, and these fluctuations mix transported quantities and cause the transported quantities to fluctuate as well. Since these fluctuations can be of high frequency and small scale, they are too computationally expensive to be modeled directly in practical engineering calculations. The equations are practically impossible to be solved analytically, and require numerical methods to be formulated to solve for particular states within the flow. The concept of these methods assumes that the components of the flow velocity, and the pressure, consist of a mean value with superimposed fluctuations. These fluctuations are bounded to remain within a spectrum of values in terms of frequency and amplitude. This spectrum of the turbulent kinetic energy can be analyzed and operated on using statistical tools, from which a variety of formulations for the mass and momentum conservation can then be derived. The most well known method is known as Reynolds averaging and forms the basis of the Reynolds-Averaged Navier Stokes Equations (RANS). RANS equations are developed from the time-dependent three-dimensional Navier-Stokes equations which are averaged in such a manner that unsteady structures of small size in space and time are eliminated and become expressed by their mean effects on the flow through the so-called Reynolds or turbulent stresses.

The Navier Stokes Equation for linear momentum is given as:

$$\frac{\partial u_i}{\partial t} + u_j \frac{\partial u_i}{\partial x_j} = -\frac{\partial P}{\partial x_i} + \nu \nabla^2 u_i \quad \text{..... [Eq. 5-1]}$$

Velocity is decomposed into mean, ūi, and fluctuating, Ui\`, components as follows:

$$Ui = \bar{u}i + Ui` \quad \text{.....[Eq. 5-2]}$$

Similarly for pressure,

$$P = \overline{P} + P` \quad \text{.....[Eq. 5-3]}$$

Substituting the decomposed velocity and pressure into the momentum equation [D-1] and taking an ensemble mean leads to the RANS equation:

$$\frac{\partial \bar{u}_i}{\partial t} + \bar{u}_j \frac{\partial \bar{u}_i}{\partial x_j} = -\frac{\partial \bar{P}}{\partial x_i} + \nu \nabla^2 \bar{u}_i - \frac{\partial \tau_{ij}}{\partial x_j} \quad \text{.....[Eq. 5-4]}$$

Where, $\{\tau_{ij} = \overline{\bar{u}i\,\bar{u}j}\}$ is the Reynolds – stress tensor.

The problem then arises of how to calculate these stresses. These stresses must be interpreted in terms of calculated time-averaged variables in order to close the system of equations thereby rendering them solvable. This requires the construction of a mathematical model known as a turbulence model, involving additional correlations for the unknown quantities. There are many ways in which this can be achieved, all relying to greater or lesser extents on further assumptions and simplifications. Due to the nature of approximations made in turbulent models, a universal accurate turbulence model is probably unattainable. This is still an area, which needs significant improvement (Stern *et al.* 1999).

5-3: CFD Solver FLUENT 6.0

The FLUENT v 6.0 CFD package consists basically of two components:

1. GAMBIT, the pre-processor and
2. FLUENT, the solver.

The pre-processor GAMBIT is used to create the model of the actual fluid-laden geometry in two (2D) or three dimensions (3D). After that, the created geometry is subdivided in a grid (or mesh) consisting of so-called cells, which form the calculation domain for the subsequent flow analysis. The cells may have a quadrilateral or triangular shape for 2D-meshes. 3D-meshes consist of hexahedral, tetrahedral, wedge-shape elements or pyramids or combinations of these. The grids can either be structured – in this case each cell is part of a rectangular block structure and has a unique Cartesian coordinate – or unstructured. Furthermore, GAMBIT allows examination of the quality of the completed mesh by assessing the cell quality (e.g. the aspect ratio of a quadrilateral cell). In general, to obtain a mesh-independent solution, the mesh resolution must be chosen to be fine enough. For the 2D-calculations, the mesh is simply refined until the solution becomes mesh-independent. On completion of the pre-processing, the grid is exported to the solver FLUENT 6.0. The solver is applied to select the appropriate physical models specifying the current problem such as:

- The flow regime: laminar or turbulent
- The problem type: steady state or transient
- The fluid properties: incompressible or compressible
- The detailed problem specification: boundary conditions and materials.

In addition to this, a solver formulation and solution parameters have to be chosen. Finally, an initial solution for all cell values must be provided. The underlying governing equations are solved in an iterative process for each individual cell of the calculation domain. The post-processing (i.e. the graphical illustration) of the results is also done using FLUENT 6.0.

5-4: Simulation of a DP Thruster Far Wake

A study was performed in order to simulate the DP thruster far wake profile using FLUENT 6.0. In this study, the simulation of the DP thruster far wake was simplified and was considered to be similar to a jet flow, in which the flow of the propeller was simulated without using the detailed propeller geometry. FLUENT 6.0 was used to simulate the DP thruster far wake flow pattern based on the experimental data from the DP thruster SPIV near wake measurements.

The two-equation models are the simplest approximate models of turbulence, allowing the turbulent velocity and length scales to be independently determined. The standard k-$\in$ is one of these models and has become the workhorse in practical engineering flow calculations since the time it was proposed by Jones and Launder (1972). Economy, robustness, and reasonable accuracy for a wide range of turbulent flows have made this model popular in industrial flow and heat transfer simulations. It is a semi-empirical model, and the derivation of the model equations is based on phenomenological considerations and empiricism. In this study, the standard k-ϵ model was employed to simulate the DP thruster far wake profile with and without a nozzle at

J= 0 and at J= 0.4 in the INSEAN large cavitation tunnel. Comparisons of the simulation results with experimental results were also carried out.

5-4-1: Simulation Set-up and Description

The 2D numerical model consisted of a meshed fluid volume of water with boundaries defining the outer limits of the domain. The domain of the problem was defined to simulate the experimental condition of the DP thruster in the INSEAN large cavitation tunnel. The scale size of the DP thruster diameter to the test condition at the INSEAN cavitation tunnel was 1:18 to the width and 1:15 to the length of the tunnel. Therefore, a box of 18 diameters wide and 15 diameters long defined the model domain. The flow field was symmetrical about the *x-y* plane, and the propeller jet was centered at the x- axis. A symmetric boundary condition was applied. The domain of the DP thruster jet simulation is shown in Fig. (5-2).

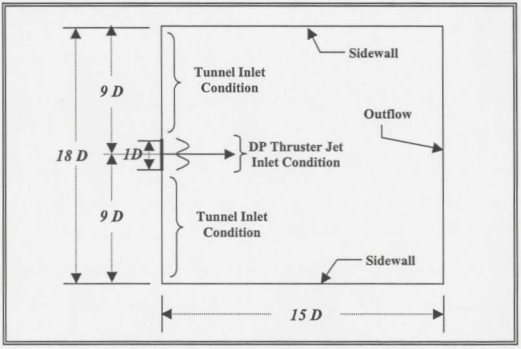

Figure 5-2: 2D domain of the simulated flow

Once the mesh was defined, it was discretized into a mesh of Structured Quad/Map type elements using the meshing software Gambit. Boundary conditions were also defined in Gambit by naming element faces located on the domain plane, inlet area, outlet area and sidewall areas. The inlet area was divided into three parts as shown in Fig. (5-2) to enable simulation of the DP thruster jet at different working conditions of advance coefficient values. A FLUENT– ready file was then generated for the given cases.

The next step in developing a CFD simulation is to choose the appropriate solver settings including which governing equations are to be solved, and how they should be discretized. FLUENT was used to set the model parameters. The FLUENT server has several options for adjusting the numerical technique used, in order to reduce error and improve performance. The selection of the solver parameters for the DP thruster jet simulation was made partly from recommendations in the FLUENT literature, and partly from trial and error evaluations of various solver-setting combinations.

The experimental results of the DP thruster at J=0 and at J=0.4 in the INSEAN large cavitation tunnel with and without a nozzle were selected for examples. Many simulation trials were performed in order to reach the best combinations of the solver parameters that to a converged and an acceptable simulation of the DP thruster jet flow for each simulation case. The final setting of the FLUENT solver parameters for each simulation example is shown in Table (5-1).

Parameter	Setting			
	Ducted Thruster		Open Thruster	
	J= 0	J=0.4	J= 0	J=0.4
Time step size	0.1			
Number of time steps	2000			
Simulation time (min)	3.33			
Max. Iterations Per Time Step	20			
Solver	2D, Segregated- Implicit, Unsteady			
Unsteady Formulation	1st Order	2nd Order	1st Order	2nd Order
Operating Pressure	101,325 Pa			
Viscous	Standard k-epsilon turbulence model			
Wall Treatment	Standard Wall Functions			
Heat Transfer	Yes			
Type of Fluid	Liquid, Water			
Water Density	998.2 kg/m^3			
Water Viscosity	0.00116 kg/m.s			
Discretization Scheme				
Momentum	QUICK			
Pressure	PRESTO			
Pressure-velocity coupling	PISO			
Turbulence Kinetic Energy	QUICK			
Turbulence Dissipation Rate	QUICK			
Energy	QUICK			

Table 5-1: Solver parameters of the jet flow simulation examples

CFD simulation needs initial values for all of the flow variables to be assigned before the solution can be computed. This is called initialization. A CFD solver creates a large set of equations based on the discretization scheme and the fundamental flow equations to be satisfied for a solution. This system of equations is most efficiently solved using an iterative approach wherein a trial solution is continuously improved until successive changes are within a predefined tolerance. In many cases, this approach will not be successful if a poor initial trial solution was used to begin the process. The system may diverge (successive iterations cause the trial solutions to get worse), or the system may converge to a solution that is clearly incorrect in term of the physical phenomena being investigated. Therefore, a proper initialization of the flow variables is an important step for a successful CFD analysis.

In the simulation process of the DP thruster far wake profile, the flow of the DP thruster was considered to be similar to a turbulent jet issuing from an orifice of the same diameter of the thruster. The initial velocity of the jet for each simulation case was considered to be the velocity of the DP thruster at X/D=0.3. The jet inlet profile was defined by assigning the value of the total flow velocity for each face-centroids of the inlet boundary mesh. This process was performed for all simulation cases by writing and defining a FLUENT profile file for each case. The results of the jet flow simulation using the second method show an acceptable simulation of the DP thruster far wake region.

5-4-2: Results of DP Thruster Far Wake Simulation

5-4-2-1: Ducted DP Thruster Far Wake Simulation Results

Fig. (5-3) shows the longitudinal profile of the FLUENT jet flow simulation of the ducted DP thruster at J=0 and J=0.4. Fig. (5-4) and Fig. (5-5) show comparison between the CFD simulation and the experimental results of the distribution of the total flow velocity at different downstream axial positions for the ducted DP thruster at J=0 and J=0.4 respectively.

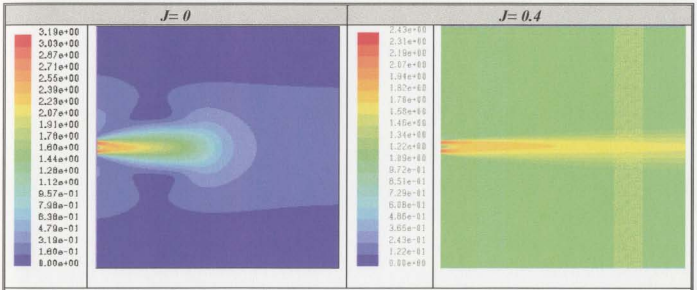

Figure 5-3: Jet flow simulation of the ducted DP thruster far wake total velocity at J=0 and J=0.4

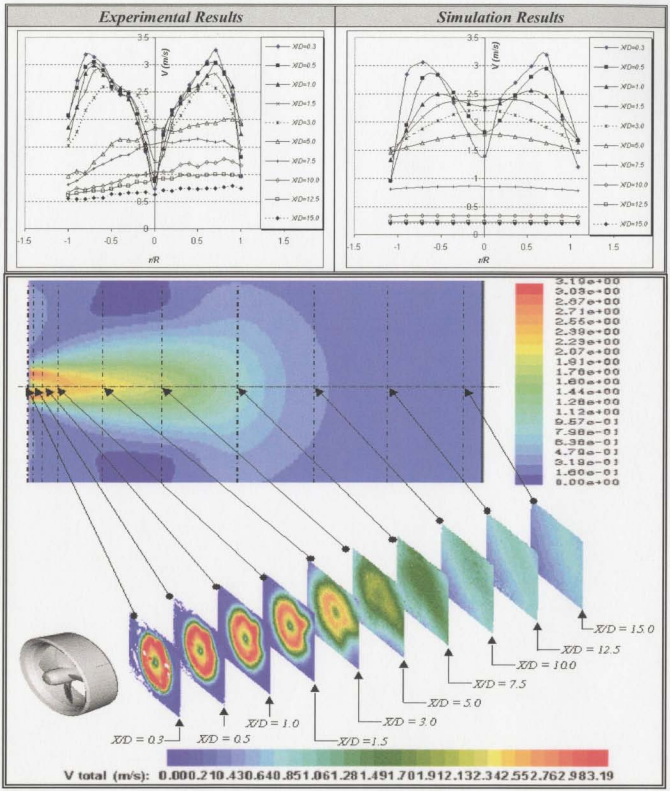

Figure 5-4: Comparison between the jet simulation results and the experimental results of the ducted DP thruster far wake total flow velocity distribution at J=0

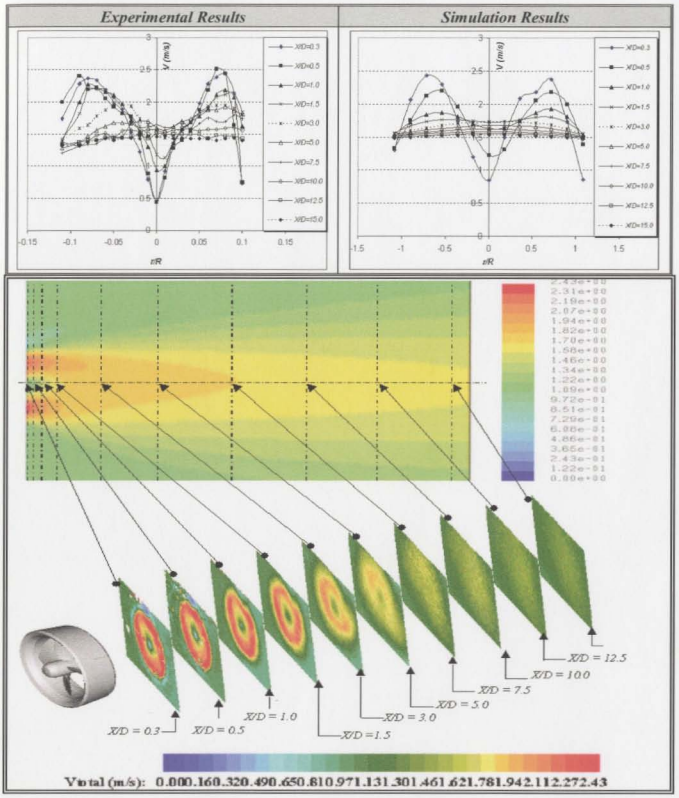

Figure 5-5: Comparison between the jet simulation results and the experimental results of the ducted DP thruster far wake total flow velocity distribution at J=0.4

The comparison between the CFD jet flow simulation and the experimental result of the ducted DP thruster far wake total flow velocity at each downstream axial plane at J=0 and J=0.4 respectively is shown in Fig. (5-6) and Fig. (5-7).

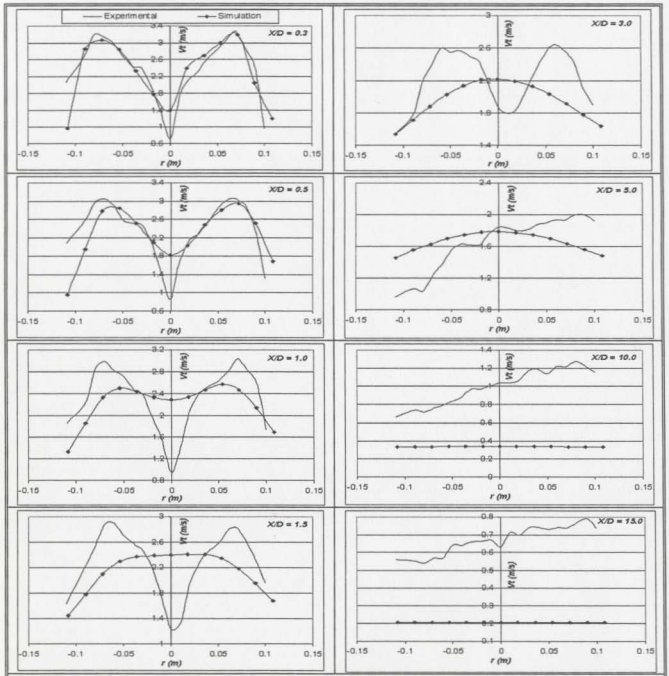

Figure 5-6: Comparison between the CFD simulation and the experimental results of the propagation of the ducted DP thruster wake total velocity at each downstream axial plane (J=0)

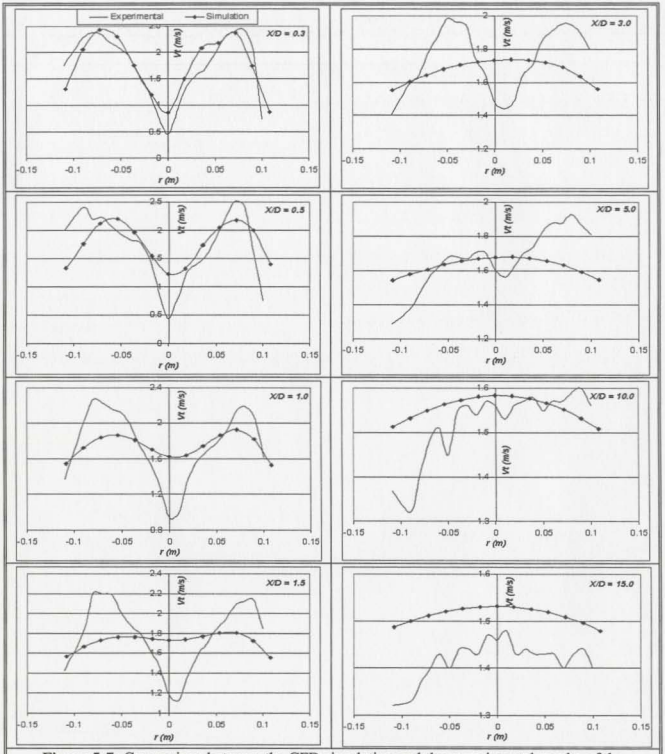

Figure 5-7: Comparison between the CFD simulation and the experimental results of the propagation of the ducted DP thruster wake total velocity at each downstream axial plane (J=0.4)

5-4-2-2: Open DP Thruster Far Wake Simulation Results

Fig. (5-8) shows the longitudinal profile of the FLUENT jet flow simulation of the open DP thruster at J=0 and J=0.4. Fig. (5-9) and Fig. (5-10) show comparison between the CFD simulation and the experimental results of the distribution of the total flow velocity at different downstream axial positions for the open DP thruster at J=0 and J=0.4 respectively.

The comparison between the CFD jet flow simulation and the experimental result of the open DP thruster far wake total flow velocity at each downstream axial plane at J=0 and J=0.4 respectively is shown in Fig. (5-11) and Fig. (5-12).

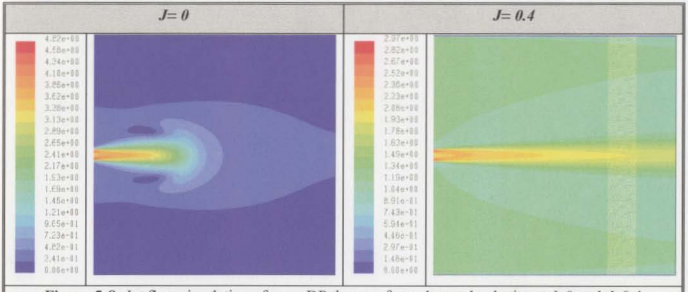

Figure 5-8: Jet flow simulation of open DP thruster far wake total velocity at J=0 and J=0.4

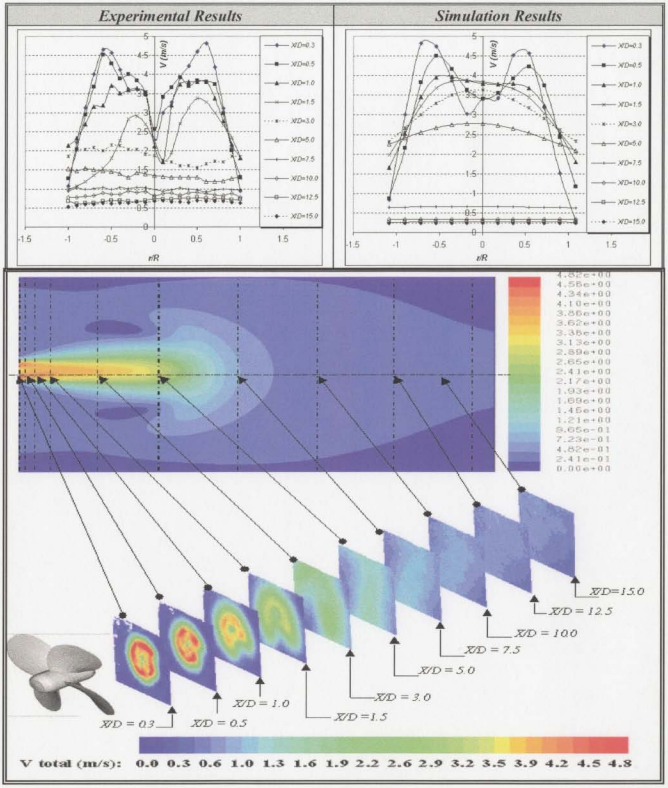

Figure 5-9: Comparison between the jet simulation results and the experimental results of the open DP thruster far wake total flow velocity distribution at J=0

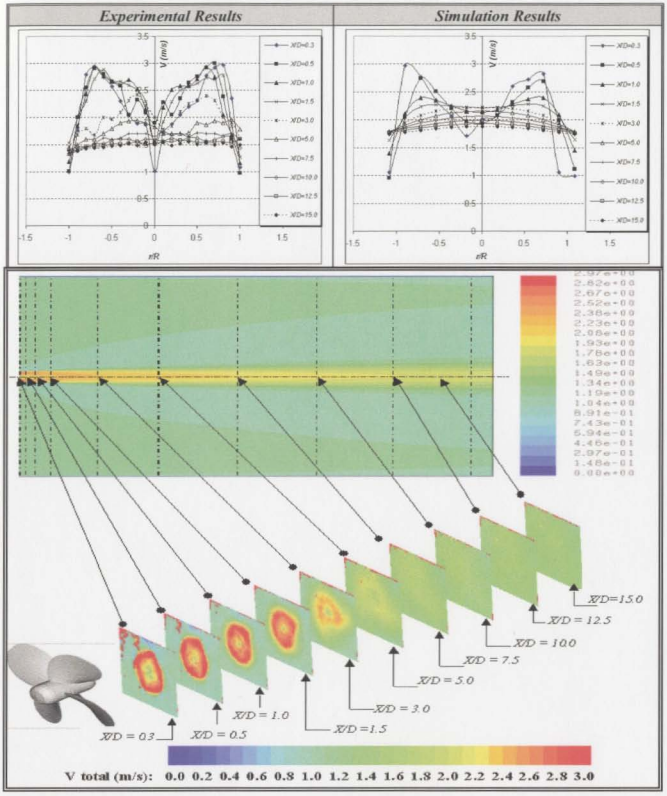

Figure 5-10: Comparison between the jet simulation results and the experimental results of the open DP thruster far wake total flow velocity distribution at J=0.4

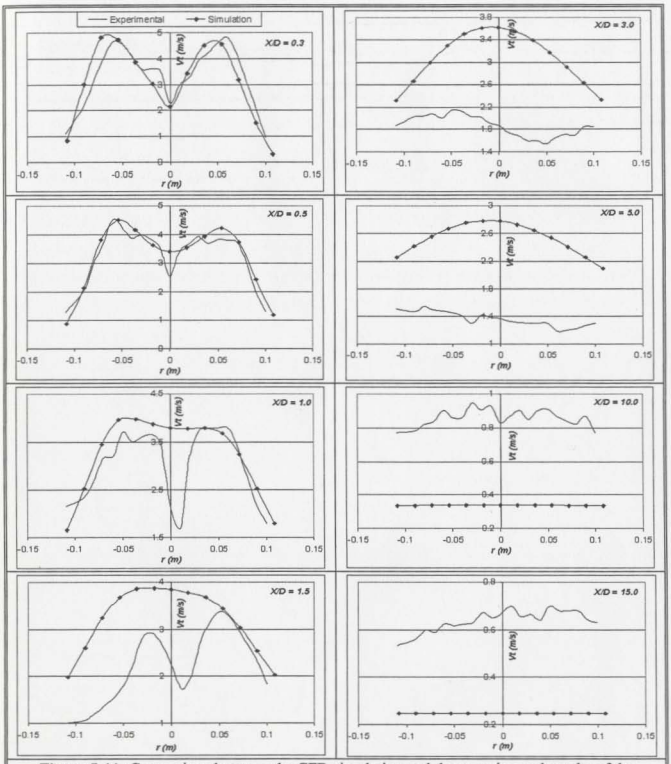

Figure 5-11: Comparison between the CFD simulation and the experimental results of the propagation of the open DP thruster wake total velocity at each downstream axial plane (J=0)

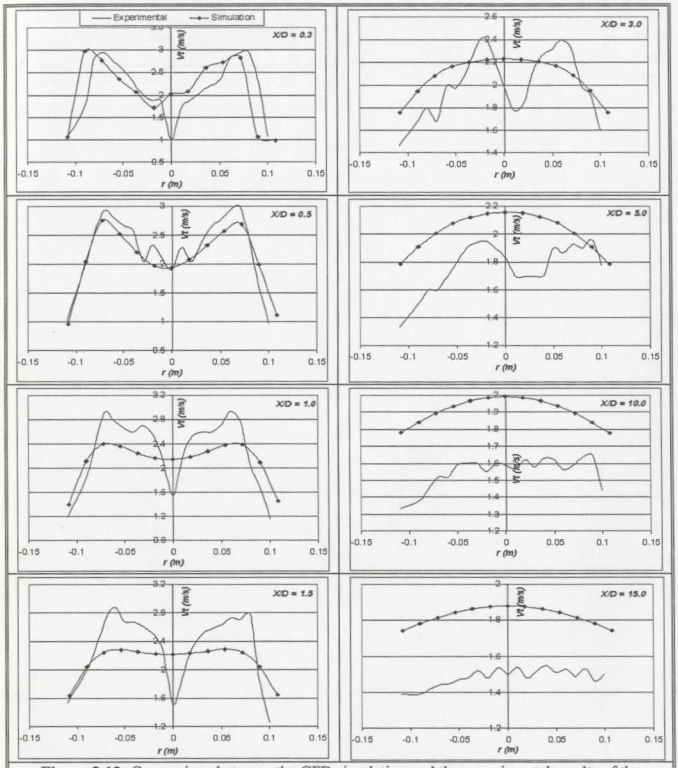

Figure 5-12: Comparison between the CFD simulation and the experimental results of the propagation of the open DP thruster wake total velocity at each downstream axial plane (J=0.4)

5-4-3: Discussion

The results of the jet simulation indicate a reduction in the total flow velocity as the distance from the orifice increases. Also, the results of jet simulation of the open and ducted DP thruster at J=0.4 show a lower velocity value at the entrance of the orifice than the results at J=0, however, the results of the total velocity propagation at X/D =15 show the opposite. This gives indication that the rate of energy decay of the jet flow at J=0 is higher than at J=0.4, and the flow of the jet at J=0.4 persists further downstream than the wake of the jet at J=0.

The comparison between the CFD simulation and the experimental results of the propagation of the DP thruster wake total velocity at each downstream axial plane indicates that the results of the CFD simulation have a good agreement with the experimental results up to X/D=0.5. Beyond X/D=0.5, the CFD results indicate more uniform and steady flow pattern than the experimental results. This may be improved by increasing the setting time of the CFD simulation.

Full Navier Stokes flow modeling of the blade, hub, duct and wake flow will be necessary to accurate represent of the detailed of the flow. This is a different long-term study, which requires accurate turbulence measurements to confirm the validity of the predictions.

CHAPTER 6

CONCLUSIONS

6-1: Summary and Significance of the Study

This is the first known attempt to evaluate Dynamic Positioning (DP) thruster performance and wake hydrodynamic characteristics when operating with and without a nozzle under varied operating conditions, including the bollard pull condition. The DP thruster performance tests were performed at a propeller geometric pitch ratio of 1.2 and different propeller speeds (10, 15, 20, and 30 rps) in the IOT towing tank. The DP thruster wake velocity measurements were carried out at different downstream axial transverse measuring planes up to 1.5 diameters downstream in the IOT cavitation tunnel and up to 15 diameters downstream in the INSEAN large cavitation tunnel. The experimental analysis of the DP thruster wake yields detailed flow information with and without a nozzle, at different advance coefficient values (J=0, J=0.4 and J=0.45), and at different propeller geometric pitch ratios (P/D=1.096, 1.2 and 1.835 using Laser Doppler Velocimetry (LDV), and at P/D=1.2 using Stereoscopic Particle Image Velocimetry

(SPIV). The application of a SPIV system in this study is the first known application of this type of system for DP thrusters wake velocity measurements.

The present work has focused on providing detailed, accurate and reliable experimental and analytical data on the performance and the hydrodynamic characteristics of a DP thruster near and far wake under a variety of working conditions. The hydrodynamic evaluation of the DP thruster near and far wake focused on evaluating and analyzing the near and far wake velocity, vorticity, total flow turbulence, momentum, thrust, flow energy, and force loading distribution and propagation.

There are few research studies that tackle the wake of DP thrusters. The detailed analysis of a DP thruster wake expands our knowledge about the hydrodynamic phenomena associated with a DP thruster wake, and provides accurate data to simulate the characteristics of the DP wake and to predict its effects on any structures in the slipstream.

The experiments and the analysis of this study were performed to increase the understanding of a DP thruster near and far wake characteristics under varied operating conditions of propeller geometric pitch ratios and advance coefficient values. The results illustrated in this work provide quantitative data, which can be used in the operational analysis of a DP thruster under a variety of operating conditions. Also, these data can be used to investigate the interaction effect between the DP thruster near and far wake and any structures that may exist in the slipstream (production lines, moorings and any submerged structure members). There is increasing demand for such information from the offshore oil and gas, and marine industries, which came to realize the importance of such information in increasing the reliability and safety of applying DP systems. Also,

the results of this study provide sufficient and reliable data useful in the validation of computational approaches to the simulation of the DP thruster near and far wake under a variety of working conditions.

6-2: Conclusions

The conclusions of the present work are split into five main parts:

- Conclusions related to the performance characteristic results of the DP thruster
- Conclusions related to the wake survey results
- Conclusions related to the measuring techniques used in this study
- Conclusions related to the numerical simulation of the DP thruster wake
- Conclusions related to practical considerations for DP thruster design

6-2-1: Conclusions Related to the Performance Characteristic Results of the DP Thruster

The results of the DP thruster performance tests provide insight about the performance behavior of the DP thruster under varied operating conditions. The following can be concluded from the results of the DP thruster performance tests. These results are originally well known from the relative performance of ducted and open propellers.

- The propeller of the Ducted DP thruster is more lightly loaded than the open DP thruster.

- The duct adds positive thrust to the propeller at the bollard pull condition. This thrust is reduced as the advance coefficient increases due to the increase in the duct drag force.

Also, the DP thruster performance tests at different propeller speeds show that the influence of change in flow Reynolds number is higher on the torque coefficient than the thrust coefficient. This is due to the effect of friction forces, which have more influence on the torque than on the thrust.

6-2-2: Conclusions Related to the DP Thruster Wake Survey Results

6-2-2-1: General Flow Features

The analysis of the DP thruster wake shows common features between the ducted and the open DP thruster wake velocity components distribution around the DP thruster under varied operating conditions of propeller geometric pitch ratios and advance coefficient values. The analysis also shows that the propeller with the nozzle is more lightly loaded than the propeller without the nozzle working at the same operating condition.

The evaluation of the open and ducted DP thruster wake at different advance coefficient values indicates increases in the magnitude of the flow velocity, vorticity, turbulence, and thrust within the slipstream of the DP thruster as the propeller loading is increased (advance coefficient is reduced). Also, the evaluation of the DP thruster wake at different advance coefficient values indicates that the wake of the DP thruster persists less distance downstream as the advance coefficient value is reduced. In the case of J=0 and J=0.4, this distance is about one to two diameters.

The analysis of the DP thruster wake vorticity at different operating conditions indicates increases in the flow vorticity as the propeller loading increases. Therefore, the heavily loaded propeller loses more energy due to the generation of vorticity than that of a lightly loaded propeller.

The comparison between the results of the ducted and the open DP thruster at the same operating condition indicates that the decay and breakdown of the open DP thruster wake takes place at a shorter distance downstream of the propeller. Also, the comparison between the ducted and open DP thruster wake characteristics at different operating conditions indicates the beneficial influence of the duct in reducing the load and improving the working condition of the propeller blades.

6-2-2-2: Near Wake Region

The near wake region is the region with high fluctuation in turbulence and in flow velocity components, contraction of the slipstream, and flow deformation due to roll up of the blade wake sheets. In this study, the DP thruster near wake region is considered to be up to 1.5 diameters downstream of the propeller.

The DP thruster near wake velocity evaluation shows that the contraction of the propeller slipstream is a function of the propeller loading condition. As the propeller loading increases the propeller slipstream contraction occurs earlier and closer to the propeller disk. Measurements at the bollard pull operating condition indicates that the contraction of the propeller slipstream takes place up to a downstream distance of 0.5 diameters from the propeller and it is about 0.8 – 0.85 of the propeller diameter, while the contraction of the propeller slipstream takes place up to a downstream distance of 1.0

diameter for the measurements at J=0.4 and J=0.45 and it is about 0.9 – 0.95 of the propeller diameter. Moreover, the contraction of the open DP thruster slipstream is higher than the ducted DP thruster.

The comparison between the ducted and the open DP thruster near wake characteristics indicates that the rate of reduction in the open DP thruster flow axial velocity, vorticity, total turbulence, momentum, thrust, and energy is higher in the near wake region than that of the ducted DP thruster when moving downstream of the propeller. Therefore, the rate of the near wake energy dissipation and decay is more rapid with distance in the case of the open propeller than the ducted propeller.

The evaluation of the DP thruster near wake characteristics at different advance coefficient values indicates that the rate of reduction in the DP thruster wake flow velocity, vorticity and total turbulence increases as the advance coefficient value is decreased. Therefore, the rate of the near wake energy decay increases as the advance coefficient decreases.

6-2-2-3: Far Wake Region

The far wake region is the region where the variations in the wake are relatively slow and where the wake decays slowly and steadily. In this study, the DP thruster far wake region was analyzed up to 15 diameters downstream.

The analysis of the DP thruster far wake characteristics indicates that the DP thruster wake becomes less rotational and more laminar as the distance downstream from the propeller increases. Also, the evaluation of the DP thruster far wake velocity, total turbulence and momentum indicates that the width of the DP thruster wake increases as

the distance from the propeller increases. Therefore, the DP thruster wake diffusion increases as the distance downstream from the propeller increases. Moreover, the evaluation of the DP thruster far wake characteristics indicate small changes in the flow characteristics (velocity, momentum, and energy) beyond a distance equal to 10 diameters downstream from the propeller.

The evaluation of the DP thruster far wake characteristics at different advance coefficient values indicates that the rate of the DP thruster far wake energy decay, diffusion and dissipation increases as the advance coefficient is decreased. Also, the evaluation of the DP thruster wake velocity, momentum and energy at a distance of 15 diameters downstream the propeller indicates that the DP thruster wake will persist further downstream as the advance coefficient increases.

6-2-3: Conclusions Related to the Study Measuring Techniques.

Two different measuring techniques were used in this study. A 2D LDV system was used in the IOT cavitation tunnel tests, and a SPIV system was used in the INSEAN large cavitation tunnel tests. The results of the LDV measurements indicate higher velocity components than the SPIV measurements, which may be due to the tunnel effects.

From the experimental point of view, stereo-PIV shows a number of advantages compared with the well-assessed LDV technique. Considering the limited time usually available for these tests combined with the management and technical difficulties typical of operating a large testing facility, the PIV technique can provide results within a short period. The LDV technique requires up to three to four times more testing time to obtain

the same information, which consequently translates into additional costs of facility occupancy. The measurement time is drastically reduced with the stereo-PIV method, where the plane of measurement is mapped instantaneously and provides all three-velocity components in one single step. The LDV technique requires multiple measurements to scan the interrogation domain. In this sense, the PIV approach offers the freedom of extending wake survey to a larger number of areas of interest, with very limited setup changes. The major drawbacks of the PIV technique are a reduced accuracy with respect to the LDV technique and the huge quantity of information gathered. One must address the critical problem of storing, managing and processing this information without compromising the testing costs by extended data processing time.

6-2-4: Conclusions Related to the Numerical Simulation of the DP Thruster Wake

The CFD simulations of the DP thruster wake for this research were performed using FLUENT 6.0 and Gambit. The simulation of the DP thruster far wake was simplified and was considered to be similar to a jet flow, in which the flow of the propeller was simulated without using the detailed propeller geometry. Therefore, the flow of the DP thruster was considered to be similar to a turbulent jet issuing from an orifice of the same diameter of the thruster. The initial velocity of the jet simulation examples was considered to be the velocity of the DP thruster experimental results at X/D= 0.3. The FLUENT solver parameters for the DP thruster jet simulation were made partly from recommendations in the FLUENT literature, and partly from trial and error

evaluations of various solver-setting combinations. The standard turbulence model (k-$\in$) was used to simulate the DP thruster far wake pattern.

The results of the FLUNET simulations show good agreements with the experimental results in presenting the breakdown, diffusion and decay of the DP thruster wake under a variety of working conditions. Moreover, the results of the FLUENT simulations show the capability of CFD solvers in simulating the flow dissipation, which could not be obtained using potential flow solvers.

6-2-5: Conclusions Related to Practical Considerations for the DP Thruster Design

From the near and far wake evaluation of the DP thruster wake hydrodynamic and momentum characteristics, it is shown that the value and the change in the DP thruster wake velocity, vorticity, total turbulence, momentum, thrust and energy is higher in the near wake region than the far wake. Moreover, the analysis of the DP thruster wake loading force shows increases in the wake loading force in the near wake region of the thruster. Therefore, for the design application of using a DP system as a station positioning keeping system, the recommended location of a thruster is to be away by approximately three to five diameters from any surrounding structures.

Moreover, DP thrusters are used in highly loaded propeller conditions (bollard pull and near bollard pull). At the bollard pull operating condition, the duct adds positive thrust to the thruster and contributes about 50% of the total thrust of the ducted DP thruster. Moreover, the duct contributes in reducing the load acting on the thruster blades and improving the working conditions of the blades. Therefore, ducted DP thrusters are

preferable for the bollard pull and near bollard pull applications than open DP thrusters. However, the propagation of the DP thruster wake force loading as the distance from the thruster increases indicates a higher rate of reduction in the case of the open thruster than the ducted thruster. In order to reduce the load acting on any structures placed in the working region of DP thrusters (thruster-structure interaction effect), a minimum distance of about three diameters (in the case of open thrusters) or five diameters (in the case of ducted thrusters) is recommended to be maintained between the thrusters and any structures placed in their working region.

In this study, a DP thruster model of 200 mm in diameter was used to investigate the hydrodynamic characteristics and load effects of DP thrusters near and far wake. The real DP thruster's diameter is about 10 to 18 times the diameter of the study DP thruster model. There are differences in wake characteristics between the small diameter and large diameter DP thrusters. These differences are mainly due to the change in flow viscosity effects as the diameter of the propeller changes. As the diameter of the propeller increases, the flow Reynolds number increases and the flow viscosity drag force reduces. Therefore, it is expected there will be higher wake thrust, momentum, and energy as DP thruster diameter increases. Moreover, DP thruster wake will persist further downstream and the rate of decay in the wake thrust, energy and force loading will reduce as DP thruster diameter increases.

This study provides detailed data about the DP thruster performance and wake hydrodynamic characteristics under variety of working conditions: with and without a nozzle, different propeller geometric pitch ratios and different advance coefficient values. These data are useful and fundamental in analyzing the induced load and vibration of the

DP thruster far wake on the slipstream-submerged structures and equipment associated with offshore systems and harbor quays. Moreover, these data are essential for the accurate assessment of the design loads on these structures, which helps in producing sound and reliable designs and achieving reliable operation of these structures.

REFERENCES

1. Abdel-Maksoud, M.; Heinke, H. J. (2002), "Scale Effects on Ducted Propellers", 24th Symposium on Naval Hydrodynamics, Fukuoka, Japan.

2. Brothers, B. (1999), "Dynamic Positioning – New Feature Documentation", The Institute for Marine Dynamics, National Research Council Canada, Report No. LM-1999-07.

3. Bull, P. W. (1996), "The Validation of CFD predictions of Nominal Wake for SUBOFF Fully Appended Geometry", 21st Symposium on Naval Hydrodynamics. Trondheim, Norway

4. Carlton, J. S. (1994), "Marine Propellers and Propulsion", Oxford; Butterworth-Heinemann, Toronto, Canada.

5. Cenedes, A. (1985), "Phase Sampling in the Analysis of a Propeller Wake", International Conference on Laser Anemometry- Advanced and Application, Manchester, U.K.

6. Chesnack, C.; Jessup, S. (1998), "Experimental Characterization of Propeller Tip Flow", 22nd Symposium on Naval Hydrodynamics, Washington D.C.

7. DANTEC (2000), " Fiber Flow Insulation and User's Guide", Denmark.

8. DANTEC (2000), "Laser Doppler Velocimetry Instruction Manual".

9. Doucet, J. M. (1996), "Cavitation Erosion Experiments in Blocked Flow with Two Ice Class Propeller Models", Master Thesis, Faculty of Engineering and Applied Science, Memorial University of Newfoundland, Canada.

10. Durrani, T. S.; Greated, C. A. (1977), "Laser Systems in Flow Measurement", Plenum Press, London.

11. Dyne, G. (1973), "Systematic Studies of Accelerating Ducted Propellers in Axial and Inclined Flow", Symposium on Ducted Propellers, The Royal Institution of Naval Architects.

12. English, J. W. (1975), "Propeller / Hull Interaction", 14th international Towing Tank Conference. Ottawa, Canada.

13. English, J. W.; Wise, D. A. (1975), "Hydrodynamic Aspects of Dynamic Positioning", Transactions of the North East Coast Institution of Engineering and Shipbuilders, UK.

14. Fay, H. (1990), "Dynamic Positioning Systems: Principles, Design and Applications", Imprimerie Nouvelle, France.

15. Felli, M.; Pereira, F.; Calcagno, G.; Di Felice, F. (2002), "Application of Stereo-PIV: Propeller Wake Analysis in a Large Circulation Water Channel", International Symposium of Application of Laser Anemometry to Fluid Mechanic, Lisbon, Portugal.

16. Felli, M. (2003), "A Versatile Fully Submersible Stereo-PIV Probe for Tow Tank Applications". Fluid Measurements and Instrumentation Symposium, Honolulu, Hawaii, USA.

17. Felice, F. Di; Roman, G.; Elefante, M. (2000), "Propeller Wake Analysis by Means of PIV", 23rd Symposium on Naval Hydrodynamics, France.

18. FLUENT User's Manual (1998). Releases 5.3.18. Copyright FLUENT Incorporated.

19. Geissler, R. (1918), "The Screw Propeller", Berlin.

20. Harvald, S. A. (1967), "Wake and Thrust Deduction at Extreme Propeller Loading", Publication 61, Statens Skeppsprovningsanstalt.

21. Hoshino, T., Oshima, A. (1987), "Measurement of Around Propeller by Using 3-Component Laser Doppler Velocimeter", Mitsubishi Technical Review.

22. Hoshino, T. (1993), "Hydrodynamic Analysis of Propellers in Unsteady Flow using a Surface Panel Method", Journal of the Society of Naval Architects of Japan, Vol. (174).

23. HSE: Healthy and Safety Executive (2000), "Review of Model Testing Requirements for FPSO's", Offshore Technology Report 2000/123, UK.

24. Hyun, B. C.; Patel, V. C. (1991), "Measurements in the Flow Around a Marine Propeller at the Stern of an Axisymmetric Body: Part 1: Circumferentially Averaged Flow", Experiments in Fluids, Vol. (11).

25. Inoue, S.; Hirano, M.; Kijma, k.; Takashina, J. (1981), "A Practical Calculation Method of Ship Maneuvering Motion", International Shipbuilding Progress, Vol. (28).

26. ITTC (1999), "22nd International Towing Tank Conference", Proceedings Vol. (II), Seoul, China.

27. Jessup, S. D. (1989), "An Experimental Investigation of Viscous Aspects of Propeller Blade Flow". Ph.D. Thesis, The Catholic University of America, Washington D.C.

28. Jessup, S.; Chesnakas, C.; Fry, D.; Donnelly, M.; Black, S.; Park, J. (2004), "Propeller Performance at Extreme Off Design Conditions", 25th Symposium on Naval Hydrodynamics, St. John's, NL, Canada.

29. Jones, W. P.; Launder, B. E. (1972), "The prediction of Laminarization with a Two-Equation Model of Turbulence", International Journal of Heat and Mass Transfer, Vol. (15).

30. Judge, C. Q.; Oweis, G.; Ceccio, S.; Jessup, S.; Chesnack, C.; Fry, D. (2001), "Tip-Leakage Vortex Inception on a Ducted Rotor", Proceeding of the 4th International Symposium on Cavitation (CAV 2001), California Institute of Technology, Pasedena, CA.

31. Kerwin, J. E. (1976), "A Deformed Wake Model for Marine Propellers", Massachusetts Institute of Technology, Ocean Engineering Report 76-6.

32. Kobayashi, S. (1982), "Propeller Wake Survey by LDV", International Symposium on Application of Laser- Doppler Anemometry to Fluid Mechanics, Lisbon, Portugal.

33. Kose, K. (1982), "On A New Mathematical Model of Maneuvering Motions of a Ship and its Applications", International Shipbuilding Progress, Vol. (29).

34. Lee, S. J.; Pailk, B. G.; Yoon, J. H.; Lee, C. M. (2004), "Three-Components Velocity Field Measurements of Propeller Wake Using A Stereoscopic PIV technique", Journal of Experiments in Fluids, Vol. (36).

35. Lehn, E. (1980), "Thruster Interaction Effects", The Ship Research Institute of Norway, Report No. R-102.80.

36. Lehn, E. (1990), "Thrusters in extreme condition PART 2, Propeller/hull interaction effects", The Ship Research Institute of Norway, Report No. FPS-2000 1.6B.

37. Liu, P.; Bose, N.; Colbourne, B. (2001), "Automated Marine Propeller Geometry Generation of Arbitrary Configurations and A Wake Model for Far Field Momentum Prediction", International Ship Building Progress (ISP), Vol. (48).

38. Min, K. S. (1978), "Numerical and Experimental Methods for Prediction of Field Point Velocities Around Propeller Blades", Massachusetts Institute of Technology, Department of Ocean Engineering, Report No. 78-12

39. Moberg, S.; Hellstrom, S. A. (1983), "Dynamic Positioning of a Four Column Semi-submersible", 2nd International Symposium on Ocean Engineering and Ship Handling, Gothenburg.

40. Morgan, M. J. (1978), "Dynamic Positioning of Offshore Vessels", PPC Books Division, Petroleum Pub. Co.

41. Narita, H.; Yagi, H.; Johnson, H. D.; Breves, L. R. (1981), "Development and Full Scale Experiences of a Novel Integrated Duct Propeller", SNAME Transactions, Vol. (89).

42. Nienhuis, U. (1986), "Simulation of Low Frequency Motions of Dynamically Positioned Offshore Structures", RINA Spring Meeting, London.

43. Nienhuis, U. (1992), "Analysis of Thruster Effectivity for Dynamic Positioning and Low Speed maneuvering", PhD Thesis, Delft University of Technology, Netherlands.

44. Oh, K. J.; Kang, S. H. (1992), "Numerical Calculation of the Viscous Flow Around a Marine Propeller", 19th ONR Symposium on Naval Hydrodynamics, South Korea.

45. Oosterveld, M. W. C. (1970), "Wake Addapted Ducted Propellers", PhD Thesis, Delft University of Technology, Netherlands.

46. Prasad, A. K. (2000), "Stereoscopic Particle Image Velocimetry", Experiments in Fluids, Vol. (29).

47. PROPELLA User Manual (1997-2003), Copyright and publication: Pengfei Liu.

48. Raffel, M.; Willert, C.; Kompenhans, J. (1998), "Particle Image Velocimetry", Springer.

49. Ridley, D. E. (1971), "Observations of the Effect of Vessel Speed on Bow Thruster Performance", Journal of Marine Technology.

50. Sacks, A. H.; Burnell, J. A. (1962), "Ducted Propellers – A Critical Review of State of the Art", Progress in Aeronautical Science, Vol. (2).

51. Shields, C. E. (1965), "Open Water Performance in Inclined Flow", Hydrodynamic Laboratory of David Taylor Model Basin, Test Report No. 110-H-01.

52. Stella, A.; Guj, G.; Felice, F Di; Elefante, M.; Matera, F. (1998A), "Propeller Flow Field Analysis by Means of LDV phase Sampling Techniques", 3rd International Symposium on Cavitation, France.

53. Stella, A.; Guj, G.; Felice, F Di; Elefante, M. (1998B), "Propeller Wake Evaluation Analysis by LDV", 22nd Symposium on Naval Hydrodynamics, Washington.

54. Stella, A.; Guj, G.; Felice, F Di; Elefante, M. (2000), "Experimental Investigation of Propeller Wake Evaluation by Means of LDV and Flow Visualizations", Journal of Ship Research, Vol. (44).

55. Stern, F.; Raven, H. C.; Bulgarelli, U.; Gustafsson, L. T.; Maksoud, M. A.; Perez-Rojas, L.; Suzuki, T.; Zhou, L. (1999), "The Resistance Committee Final Report and Recommendations to the 22nd ITTC", Seoul, Korea.

56. Stierman, E. J. (1984), "Extrapolation Methods for Ships with Ducted Propellers", International Shipbuilding Progress, Vol. (31).

57. Solof, S. M.; Adrian, R. J.; Liu, Z. C. (1997), "Distortion Compensation for Generalized Stereoscopic Particle Image Velocimetry", Journal of Measurement Science Technology, Vol. (8).

58. Thronhill, E. (2002), "Application of a General CFD Code to Planing Craft Performance", Ph.D. Thesis, Faculty of Engineering and Applied Science, Memorial University of Newfoundland, Canada.

59. TSI (2000), "Stereoscopic Particle Image Velocimetry Software Instruction Manual".

60. van den Boom, H. J. J.; Nienhuis, U. (1983), "Hydrodynamic Analysis of Dynamically Positioned Vessels", International Workshop on Ship and Platform Motions, Berkeley.

61. van den Made, A.; Bussemaker, O. (1976), "Thrusters for Dynamic Positioning", Offshore Craft Conference, London.

62. van Lammeran, W. P A.; Troost, L.; Koning, J. G. (1984), "Resistance, Propulsion and Steering of Ships", The Technical Publishing Company, Staam, Haarlem, Netherlands.

63. van Leest, H.; Bussemaker, O. (1976), "The performance and Characteristics of Thrusters", Offshore South East Asia Conference, Singapore.

64. Versteeg, H. K.; Mallalasekera, W. (1995), "An Introduction to Computational Fluid Dynamics – The Finite Volume Method", Longman Group Ltd., Harlow.

65. Webster, J.; Borges, de Sousa (1999), "Optimum allocation for multiple thruster". Proceedings of the 1999 ISOPE Conference, Brest, France, Vol. (83).

66. Wise, D. A.; English, J. W. (1975), "Tank and Wind Tunnel Tests for a Drift-Ship with Dynamic Position Control", Offshore Technology Conference (OTC), Houston, Texas, USA.

67. Yumuro, A. (1975), "A Model Experiment on Incoming Flow Direction to the Rudder a Ship Sailing Obliquely", 14th International Towing Tank Conference (ITTC), Ottawa, Canada.

APPENDIX A

Experimental Facilities

A-1: DP Thruster Model

The propeller used was a 200 mm diameter controllable pitch propeller model. This model was tested because of its availability and its similarity to DP thruster designs. The model was constructed from brass using CNC machining and was milled to an accuracy of ± 0.05 mm in thickness.

A strut system and fin were designed and fabricated at Memorial University of Newfoundland in order to support the DP thruster model in the INSEAN large cavitation tunnel. Fig. (A-1) shows a schematic diagram of this system. Also, a support bracket was designed and fabricated at the IOT workshop in order to support the arm, which was used to measure the duct thrust during the DP thruster towing tank performance tests at the IOT towing tank. A schematic diagram to the duct load measurement arm at the support bracket of this arm is shown in Fig. (A-2). Fig. (A-3) and Fig. (A-4) show the shows the location of the DP thruster model in the IOT cavitation tunnel and INSEAN large cavitation tunnel test section, respectively.

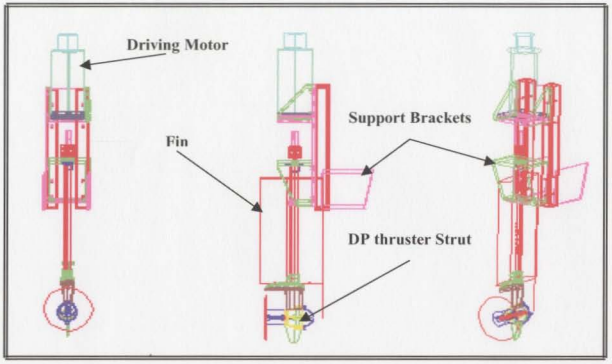

Figure A-1: Schematic diagram of the DP thruster support, driving and strut systems.

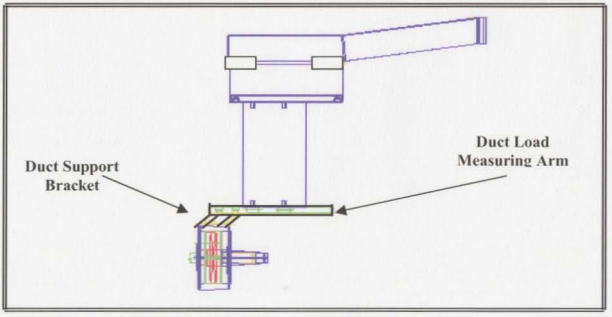

Figure A-2: Schematic diagram of the DP thruster duct support and load measuring arm

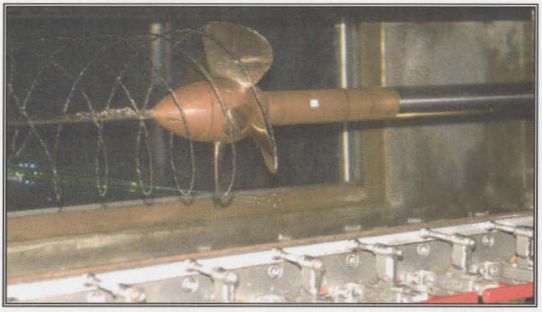

Figure A-3: DP Thruster model in the IOT cavitation tunnel

Figure A-4: DP thruster model in the INSEAN cavitation tunnel.

A-2: IOT Cavitation Tunnel

The IOT cavitation tunnel test sections are shown in Fig. (A-5) and the control panels of the cavitation tunnel LDV system are shown in Fig. (A-6). Fig. (A-7) shows the IOT cavitation tunnel dynamometer.

Figure A-5: The IOT cavitation test windows

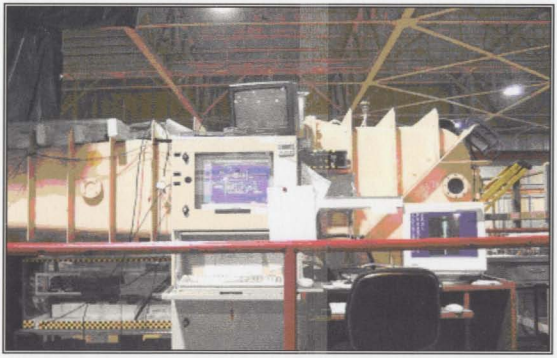

Figure A-6: The IOT cavitation tunnel and LDV control panels

Figure A-7: The IOT cavitation tunnel dynamometer

A-3: INSEAN Cavitation Tunnel

The schematic diagram of the INSEAN cavitaion tunnel elevation and side view are shown in Fig.(A-8).

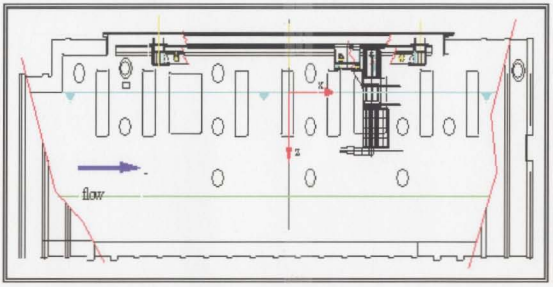

a: Elevation View

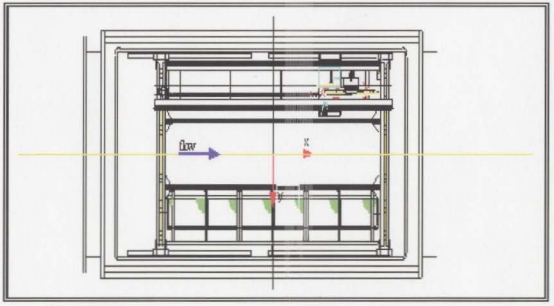

c: Plan View

Figure A-8: INSEAN cavitation tunnel cross-sectional view

APPENDIX B

Experimental Results and Analysis of the DP Thruster LDV Measurements

An LDV system was used to measure the flow velocity of the DP thruster model near wake region. Measurements were performed at propeller geometric pitch ratio of 1.096, 1.2 and 1.835; and at advance coefficient value of 0.4 and 0.45. These tests were performed with and without a nozzle for the DP thruster at a geometric pitch ratio of 1.096 and 1.2. Only the ducted DP thruster near wake velocity measurements were performed at pitch ratio of 1.835. This was due to the high level of cavitation and air bubbles generated during the near wake velocity measurements of the open DP thruster.

The following figures, (B-1) to (B-4), show the near wake velocity distribution of the DP thruster at propeller geometric pitch ratio of 1.096, with and without a nozzle; at three different downstream axial transverse measuring plans (X/D = 0.5, 1.0, and 1.5); and at advance coefficients of 0.4 and 0.45. Figures (B-5) to (B-9) show the same distribution of the DP thruster near wake velocity components at propeller geometric pitch ratio of 1.835 with the nozzle only.

B-1: Results of the LDV Measurements at *P/D*=1.096

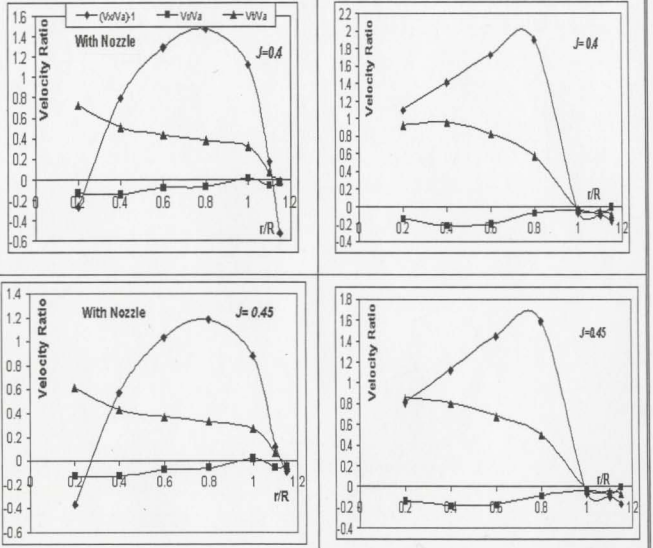

Figure B-1: Circumferential variation of velocity components around the DP thruster at J=0.4 and J=0.45; with and without a nozzle; at X/D = 0.5; and at P/D =1.096

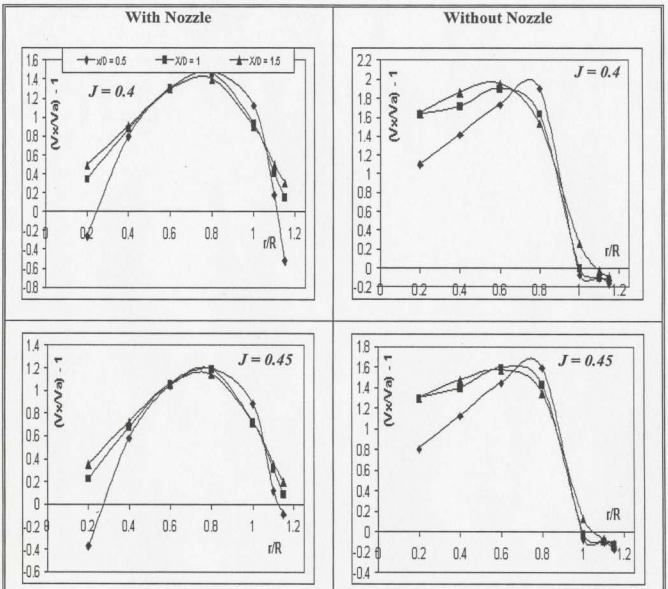

Figure B-2: DP thruster near wake mean axial flow velocity evolution with and without the nozzle at J=0.4 and J=0.45; and at P/D =1.096

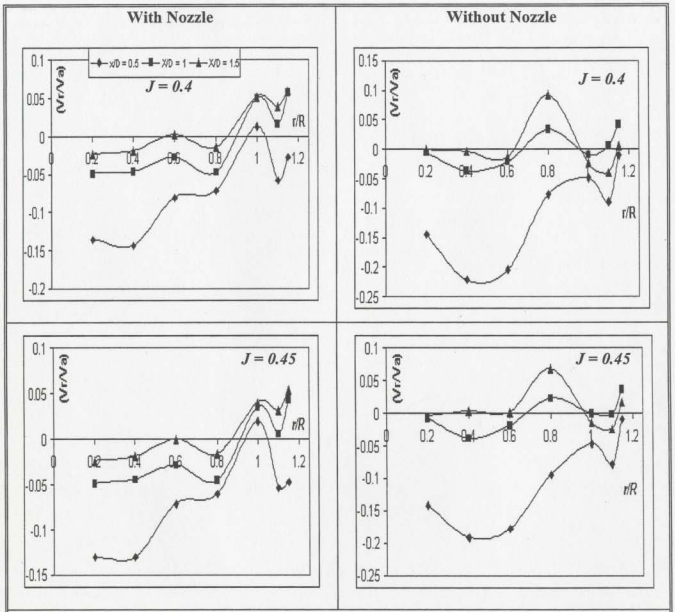

Figure B-3: DP thruster near wake radial flow velocity evolution with and without the nozzle at J=0.4 and J=0.45; and at P/D =1.096

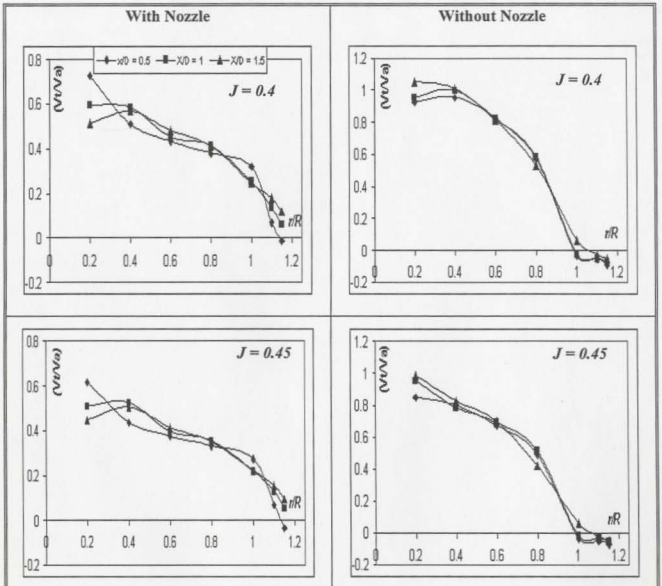

Figure B-4: DP thruster near wake tangential flow velocity evolution with and without the nozzle at J=0.4 and J=0.45; and at P/D =1.096

B-2: Results of the LDV Measurements at *P/D*=1.835

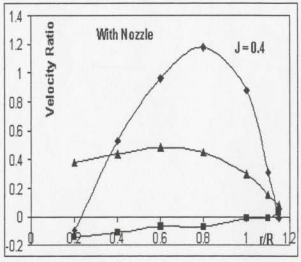

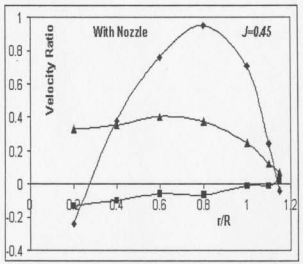

Figure B-5: Circumferential variation of velocity components around the ducted DP thruster at *J*=0.4 and *J*=0.45; at *X/D* = 0.5; and at *P/D* =1.835

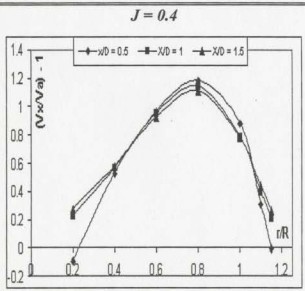

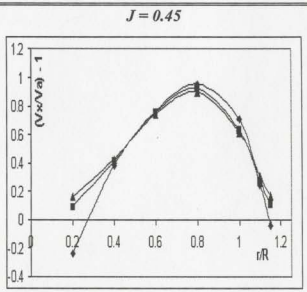

Figure B-6: Ducted DP thruster near wake mean axial flow velocity evolution at *J*=0.4 and *J*=0.45; and at *P/D* =1.835

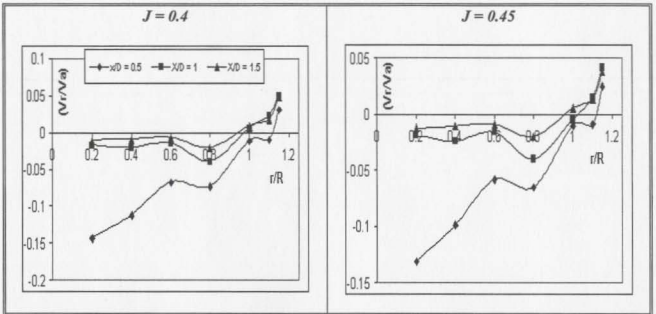

Figure B-7: Ducted DP thruster near wake radial flow velocity evolution at J=0.4 and J=0.45; and at P/D =1.835

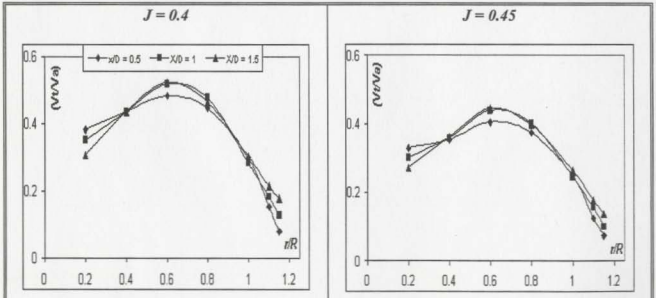

Figure B-8: Ducted DP thruster near wake tangential flow velocity evolution at J=0.4 and J=0.45; and at P/D =1.835

APPENDIX C

Experimental Results and Analysis of the DP Thruster

SPIV Measurements

The SPIV system was used to measure the flow velocity of the DP thruster model with and without a nozzle near and far wake regions. Measurements were performed at a propeller geometric pitch ratio of 1.2; and at an advance coefficient value of 0.0, 0.4 and 0.45. Measurements were performed at downstream axial transverse measuring plans (*X/D*) of 0.1, 0.2, 0.3, 0.5, 0.75, 1.0, 1.5, 3.0, 5.0, 7.5, 10.0, 12.5, and 15.0. Measurements with the nozzle could not be performed at *X/D* =0.1 and 0.2 due to the presence of the nozzle.

Figures (C-1) and (C-2) show the axial evolution of the near and far wake axial flow velocity of the ducted and open DP thruster model, respectively. The near and far wake flow vorticity distribution of the ducted and open DP thruster are shown in Figures (C-3) and (C-4). Figures (C-5) and (C-6) show the propagation of the axial flow velocity at different radial and downstream axial positions in the near and far wake regions, respectively. Finally, the propagation of the ducted and open DP thruster axial velocity ratio in the near and far wake regions at different radial and downstream axial positions are shown in Figures (C-7) and (C-8).

C-1: Results of the DP Thruster wake Axial Flow Velocity Evolution

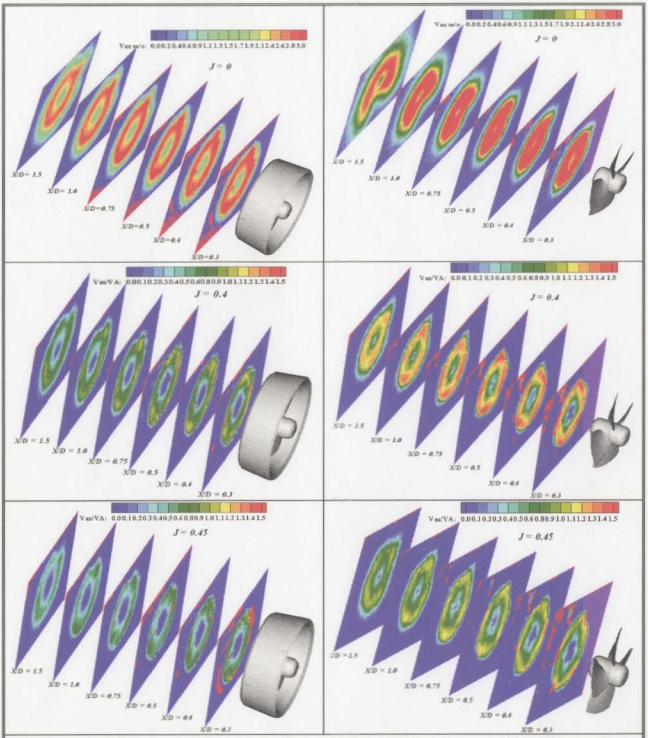

Figure C-1: SPIV near wake mean axial flow velocity evolution with and without the nozzle at J=0, J=0.4 and J=0.45

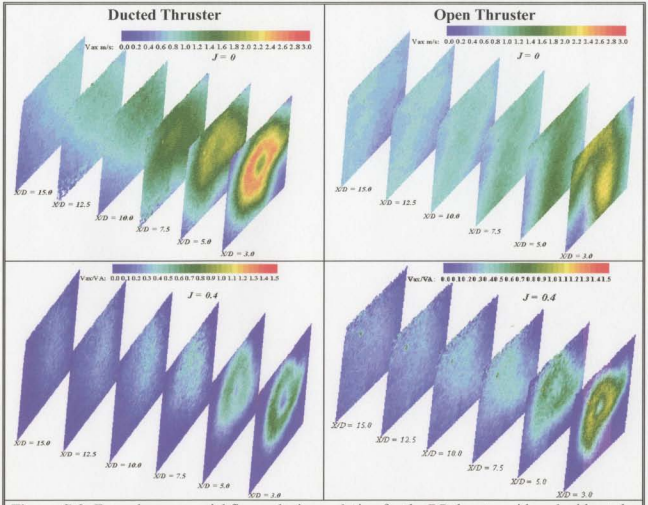

Figure C-2: Far wake mean axial flow velocity evolution for the DP thruster with and without the nozzle, and at J=0 and J=0.4

C-2: Results of the DP Thruster wake Vorticity Evolution

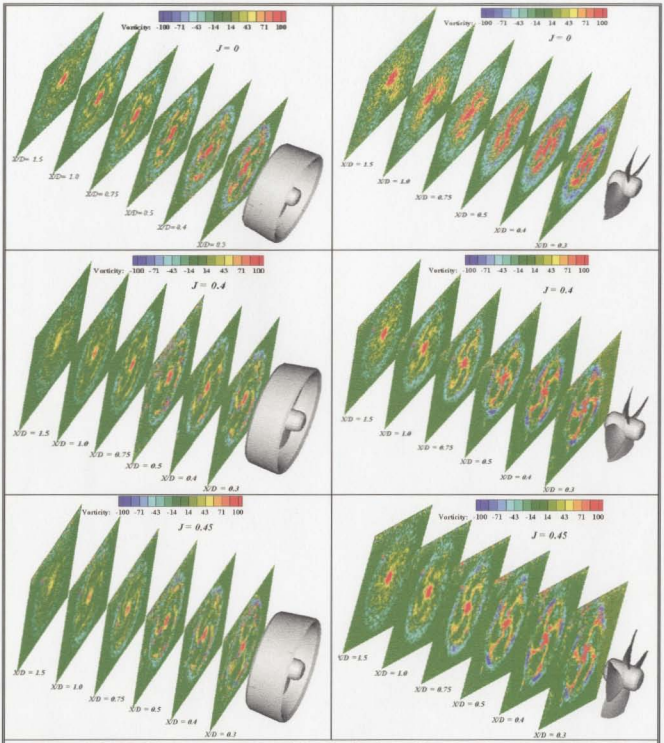

Figure C-3: DP thruster near wake vorticity distribution with and without the nozzle at J=0, J=0.4 and J=0.45

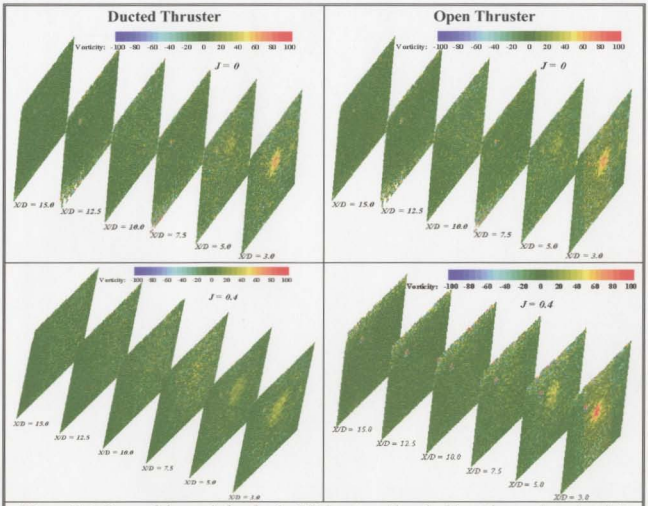

Figure C-4: Far vorticity evolution for the DP thruster with and without the nozzle, and at J=0 and J=0.4

C-3: Results of the Axial Flow Velocity Evolution at Different Radial and Downstream Axial Positions

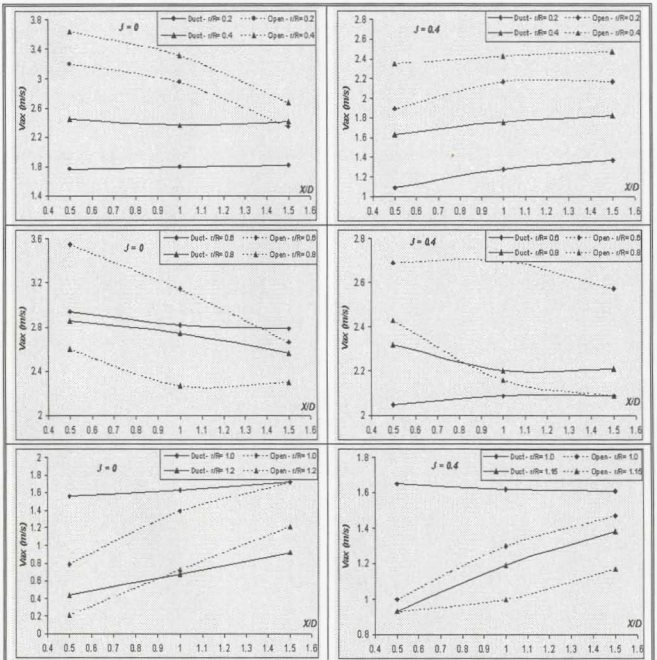

Figure C-5: DP thruster near wake axial flow velocity propagation with and without a nozzle, at different radial and downstream axial plans; and at J=0 and J=0.4

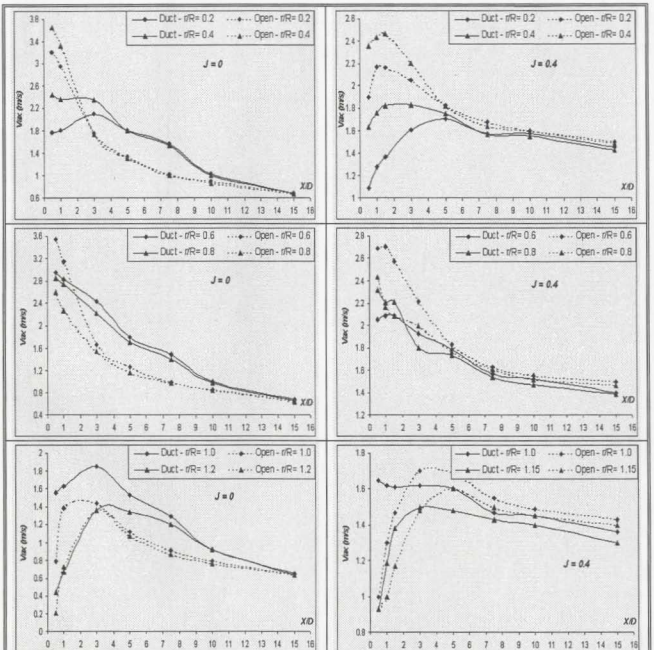

Figure C-6: DP thruster axial flow velocity propagation with and without a nozzle, at different radial and downstream axial plans; and at J=0 and J=0.4

C-3: Results of the Axial Flow Velocity Decay Evaluation at Different Radial and Axial Downstream Positions

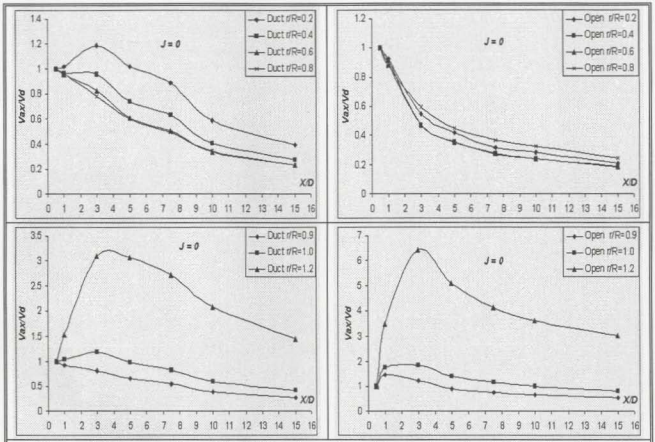

Figure C-7: Propagation of the DP thruster wake axial velocity ratio at different radial and downstream axial plan, with and without a nozzle, and at J=0

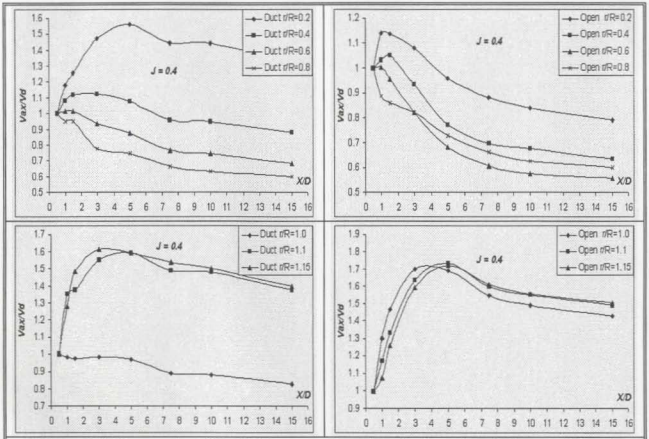

Figure C-8: Propagation of the DP thruster wake axial velocity ratio at different radial and downstream axial plan, with and without a nozzle, and at J=0.4